PEOPELS'S DEMOCRATIC REPUBLIC OF ALGERIA

MINISTRY OF HIGHER EDUCATION AND SCIENTIFIC RESEARCH

Blida 01 University

Institute of Aeronautics and Space Studies

In partial fulfilment of the requirements for The Degree of Master in Aeronautics.

Specialty: Aircraft propulsion

Analysis and numerical simulation of flows in a centrifugal compressor with Large-Eddy Simulation (L.E.S).

A Thesis Submitted by

KAZOUAI Abderrahmane

KELBITE Hamza

Under the Supervision of

Mr. LAAZEB Sebaa

Blida 2023-2024

Acknowledgement

الحمد لله ربِّ العالمين والصلاة والسلام على من أرسله الله رحمة العالمين وعلى آله وصحبه وإخوانه إلى يوم الدين وبعد،

فنحمد الله سبحانه وتعالى حمداً كثيراً طيباً مباركاً فيه كما يحب ويرضى على نعمه التي تعد ولاتحصى ومما أنعم علينا أن وفقنا لإتمام بحثنا هذا فله الحمد وله الشكر، وكما قال صلى الله عليه وسلم "من لا يشكر الناس لا يشكر الله". فمن هذا المقام نتوجه بجزيل الشكر لآبائنا الذين لا يمكن أن نرد مالهم من الفضل علينا فجزاهم الله خيراً ،وكذلك لا ننسانا شيخنا و معلمنا الشيخ فركوس الذي هو بمكانة الأب لنا فجزاه الله خيراً عنا و عن المسلمين و بارك الله لنا فيه و في علمه، و لا ننسا التوجه بالشكر إلى أستاذنا الفاضل "لعزب سبع" الذي لولا أن وفقنا الله للعمل معه لما تمكنا من إتمام مشروعنا فله جزيل الشكر على كل مجهوداته فقد كان العون الأكبر و السند الأعظم لنا و لا نقدر أن نرد له فضله علينا فجزاه الله خيراً و نشكر أستاذنا الكريم الآخر "رزوق طاهر" مسؤول مخابر المعهد الذي كان له عون كبير في الوصول إلى هذه النقطة بالسماح لنا بالإستعانة بمخبر المعهد لإنجاز مشروعنا فبارك الله فيه.

ملخص

الهدف الأساسي من هذا المشروع هو التقاط هياكل تدفق الموائع داخل ضاغط الطرد المركزي باستخدام نموذج محاكاة (LES) ومقارنتها بنماذج رانس (RANS) و رانس غير المستقر (URANS). ومن خلال إجراء عمليات المحاكاة عبر معالم مختلفة، نهدف إلى معرفة الاختلافات من حيث التدفقات المضطربة. تراقب هذه الدراسة المقارنة النماذج عبر مؤشرات متعددة مثل الضغط الساكن والضغط الكلي ورقم الماخ وغيرها و توضح قدرة LES على تقديم الدقة و التفاصيل. تتماشى دراستنا مع دراسات ديناميكيات الموائع الحاسوبية المتقدمة المماثلة (CFD)، و تؤكد الدور المهم لنموذج LES في تعزيز فهم تدفقات المضطربة للآلات التوربينية وتحسينها.

كلمات مفتاحية: هياكل التدفق, التدفقات المضطربة, الضغط الساكن والكلي.

Résumé:

L'objectif principal de ce projet est de capturer les structures d'écoulement à l'intérieur d'un compresseur centrifuge en utilisant le modèle de simulation des grandes échelles (LES) et de le comparer aux modèles RANS (Reynolds-Averaged Navier-Stokes) et URANS (Unsteady RANS). En effectuant des simulations sur différents plans, nous voulons voir les différences en termes d'écoulements turbulents. Cette étude comparative observe les modèles dans de multiples paramètres tels que la pression statique et totale, le nombre de Mach, et d'autres démontrant le potentiel de LES pour offrir précision et détails. Notre étude est alignée sur des études avancées similaires de dynamique des fluides numérique (CFD), et soulignant le rôle important de la LES dans l'amélioration de la compréhension et de l'optimisation des écoulements turbulents des turbomachines.

Mots clef : structure d'écoulement, l'écoulement turbulent, la pression statique et totale.

Abstract:

The primary objective of this project is to capture the flow structures within a centrifugal compressor using the Large Eddy Simulation (LES) model and to compare it against the Reynolds-Averaged Navier-Stokes (RANS) and Unsteady RANS (URANS) models. By conducting simulations across different planes, we aim to see the differences in term of turbulent flows. This comparative study observe the models in multiple parameters such as the static and total pressure, the Mach number, and others demonstrating the potential of LES to offer accuracy and details. Our investigation is aligned with similar advanced

computational fluid dynamics (CFD) studies, and underscoring the important role of LES in enhancing the understanding and optimization of turbulent turbomachinery flows.

Key word: flow structures, turbulent flows, static and total pressure.

Table of Contents

LIST OF FIGURES

List of Tables

INTRODUCTION:

In the aviation sector, turbocompressors are extensively utilized to enhance power output. Radial compressors are the most commonly employed type due to their capability to handle higher power levels and achieve a high-pressure ratio at low airflow rates, compared to axial turbocompressors of equivalent size.

A stage of a centrifugal compressor comprises a rotating component (rotor or impeller) and a stationary component (stator or diffuser), both crucial for the compressor's proper operation.

- Rotor Component (Centrifugal Impeller): The primary function of the impeller is to increase the fluid's energy, manifested as both heat and stagnation pressure. This increase in stagnation pressure translates into higher static pressure and elevated kinetic energy.
- Stator Component (Diffuser): The diffuser's main role is to reduce the stagnation pressure due to inherent losses, while simultaneously converting the form of energy, resulting in increased static pressure and decreased kinetic energy.

The flow analysis within this compressor stage is generally viscous, compressible, three-dimensional, and turbulent. Addressing this analytically is challenging, but it can be tackled numerically using ANSYS CFX software. This software suite includes three models: CFX-BladeGen for 3D generation, CFX-Turbogrid for structural mesh generation, and a results processing module.

This study is organized into four chapters:

Literature Review: This section provides an understanding of the studied phenomenon by citing previous research findings.

Chapter 1: This chapter covers the basics of turbomachinery, with general definitions related to compressors, particularly centrifugal compressors, their classifications, and descriptions of their various characteristics.

Chapter 2: This chapter presents the analytical equations governing a stage of a centrifugal compressor and the governing equations for the CFD model, focusing on existing turbulence models.

Chapter 3: This chapter details numerical modeling and the use of ANSYS CFX software. It describes the modeling of the geometries of the centrifugal compressor impeller and diffuser in detail, along with meshing under specific conditions. The turbulence models employed in this study (RANS, URANS and LES) and the finite volume method with numerical discretization are also presented.

Chapter 4: This chapter presents the results for the centrifugal compressor stage and validates these results by comparing the numerical findings with Ziegler's experimental results.

Finally, the conclusion offers suggestions for future research directions.

Literature review

Centrifugal compressors are a crucial component in various industrial applications, including power generation, oil and gas, and refrigeration systems. These turbomachines play a vital role in increasing the pressure of a gas by converting its kinetic energy into potential energy. The design and operation of centrifugal compressors involve complex physics and engineering principles, making them a subject of ongoing research and development.

Numerical studies have been instrumental in understanding the behavior of centrifugal compressors, particularly in optimizing their performance and efficiency. These studies utilize computational fluid dynamics (CFD) and other numerical methods to simulate the flow behavior within the compressor, allowing for the analysis of various design parameters and operating conditions.

Practical studies, on the other hand, involve experimental testing and validation of centrifugal compressor designs. These studies provide valuable insights into the compressor's behavior under real-world operating conditions, allowing for the refinement of design parameters and the development of more efficient and reliable compressors.

The design and operation of centrifugal compressors involve a range of considerations, including the impeller's geometry, the diffuser's design, and the compressor's overall aerodynamic and mechanical performance. Numerical and practical studies have contributed significantly to our understanding of these factors and have led to the development of more efficient and reliable centrifugal compressors.

Many researchers have already studied and analysed the flow in a centrifugal compressor, for an overview:

Rui Zhu [1] 2021

Real centrifugal compressor performance often deviates from the design due to manufacturing and operational uncertainties, causing instability. Studies addressing both types of uncertainties are rare, and the underlying flow mechanisms remain unclear. This study analyses a centrifugal compressor stage using CFD simulation and stochastic collocation methods. They assess the effects of various uncertainties on performance, highlighting the significant impact of tip clearance uncertainty. This study sheds light on complex flow dynamics downstream, providing insights for designing more robust compressors.

Wang Yi [2] 2020

The study explores how increasing the total pressure ratio in centrifugal compressors can lead to high subsonic or even supersonic flow at the diffuser inlet, causing additional shock loss and decreasing stage performance. Pre-compression, achieved through wedge diffusers with varying angles and blade numbers, is investigated for its efficacy in reducing shock loss and enhancing performance. Results indicate that optimal performance is achieved with pre-compression angles of 2.5° to 5.5° and divergence angles of 7° to 9°. Additionally, increasing the number of blades slightly improves the total pressure ratio and adiabatic efficiency while decreasing the surge margin.

Seongbin Hong [3] 2022

This study investigates the intricate 3-dimensional flow structures affecting the performance and efficiency of centrifugal compressors, particularly those in hydrogen-powered fuel cell electric vehicles (FCEVs). Using critical-point theory and probabilistic definitions, the analysis focuses on vortex structures in an air supply device for commercial FCEVs. Findings reveal the presence of tip leakage, hub separation, and horseshoe vortices, impacting compressor aerodynamics. Notably, optimization of compressor design leads to a 1.47% improvement in average pressure difference across all flow rates.

Ali Zamiri [4] 2020

This study delves into the dynamics of unsteady flow in a transonic centrifugal compressor with a vaned diffuser, employing computational simulations based on three-dimensional, compressible, unsteady Navier-Stokes equations. Using a high-compression ratio compressor model, the analysis focuses on the interaction of pressure waves with diffuser blade surfaces, revealing pulsating behavior within the diffuser. Moreover, the spectral analysis identifies blade passing frequency tonal noise as a primary noise source. Comparison with the URANS-SST approach highlights the superior resolution of transient fluctuations by the hybrid scale-adaptive simulation (SAS) model. The study suggests SAS as a promising approach for predicting transient phenomena with significantly reduced turnaround time compared to LES.

Simon J [5] 2009

This study compares large eddy-resolving simulations for jets using different numerical schemes and subgrid-scale (SGS) models. Results show little variation among SGS models, indicating that for schemes with dissipative elements, the SGS model can be omitted, termed numerical large eddy simulation (NLES). More complex geometries like coaxial and chevron nozzle jets are explored. Near-wall Reynolds-averaged Navier-Stokes (RANS) models are employed to cover streak-like structures. Compressor and turbine flows are successfully computed using the NLES-RANS strategy, with the RANS layer aiding in preventing premature separation upstream of the compressor's leading edge. While capturing correct flow over the turbine is challenging, the RANS layer proves helpful. The study suggests that issues like inflow conditions, problem definition, and transition are more influential than the SGS model for the considered flows.

S. Vagnoli [6] 2015

This paper employs unsteady RANS computations to investigate the onset of rotating stalls in a transonic centrifugal compressor, considering realistic installation effects due to space limitations. It compares the impact of ideal uniform inlet conditions with inlet distortions caused by a bent pipe placed in front of the impeller. Detailed numerical techniques are described, including modeling the entire annulus of the radial machine and utilizing high-performance computing to capture non-periodic phenomena leading to stall inception. Stable boundary conditions are used to prevent large unphysical surge cycles. Results show that with a uniform inlet flow, 8 blockage cells rotate in the same direction as the compressor form, while the installation of an elbow in front of the impeller suppresses the formation of a rotating stall pattern**.**

Ibrahim Shahin [7] 2016

This study investigates active surge control and performance enhancement for a NASA CC3 aero engine centrifugal compressor using self-recirculating bleed slots positioned differently. Unsteady three-dimensional numerical simulations based on large eddy simulation

are conducted. Three bleeding slot positions are compared with a compressor without surge control. The aim is to remove reversed flow during surge inception from the impeller inducer, affecting stable operation and compressor pressure ratio. Detailed analysis of the impeller flow field highlights the effects of bleeding slot positions on internal flow and compressor performance. Surge event stages are well detected inside the impeller and diffuser. Results indicate that an effective bleeding system can increase surge limit by 8% compared to a classical compressor without such a system. Closer placement of bleeding slots to the main blade's leading edge yields a higher surge limit increase compared to slots near the split blade's leading edge.

Ali Zamiri, Byung Ju Lee, Jin Taek Chung [8] 2017

The study employs three-dimensional, compressible, unsteady Navier–Stokes equations to examine the flow field of a transonic centrifugal compressor with a high compression ratio. The computational domain includes an inlet bell mouth, an impeller with splitter blades, and a two-dimensional wedge-vaned diffuser. Validation against experimental data is conducted for aerodynamic compressor performance and flow field. The analysis focuses on pressure fluctuations and entropy production within the impeller and diffuser passages at the design point. Interaction between impeller and diffuser blades induces unsteadiness and pulsating behavior in the diffuser passages. Pressure waves and unsteady separation bubbles are observed along the diffuser blade surfaces. Pressure fluctuation spectra are evaluated to analyze noise characteristics, mainly blade passing frequency noise. The study suggests the URANS approach as a tool for predicting unsteady flow and compressor noise with appropriate turbulence modeling and well-resolved grids.

Kai U.Ziegler [9]

This paper explores the impact of impeller-diffuser interaction on centrifugal compressor flow. Part I investigates flow configuration and performance, focusing on radial gap adjustment between the impeller and diffuser. Results indicate smaller gaps lead to more uniform flow at diffuser exit and higher pressure recovery, enhancing compressor efficiency. Part II employs laser velocimetry to illuminate underlying mechanisms. Experimental findings are shared as an open CFD test case called "Radiver.".

Chapter 1 Generality's

1. 1 Turbomachine

We classify as turbomachines all those devices in which energy is transferred either to, or from, a continuously flowing fluid by the dynamic action of one or more moving blade rows. The word turbo or turbines is of Latin origin and implies that which spins or whirls around. Essentially, a rotating blade row, a rotor or an impeller changes the stagnation enthalpy of the fluid moving through it by doing either positive or negative work, depending upon the effect required of the machine. These enthalpy changes are intimately linked with the pressure changes occurring simultaneously in the fluid.

Two main categories of turbomachine are identified: firstly, those that absorb power to increase the fluid pressure or head (ducted and unducted fans, compressors, and pumps); secondly, those that produce power by expanding fluid to a lower pressure or head (wind, hydraulic, steam, and gas turbines). Figure 1.1 shows, in a simple diagrammatic form, a selection of the many varieties of turbomachines encountered in practice. The reason that so many different types of either pump (compressor) or turbine are in use is because of the almost infinite range of service requirements. Generally speaking, for a given set of operating requirements one type of pump or turbine is best suited to provide optimum conditions of operation.

Turbomachines are further categorised according to the nature of the flow path through the passages of the rotor. When the path of the through-flow is wholly or mainly parallel to the axis of rotation, the device is termed an axial flow turbomachine [e.g., Figures 1.1(a) and (e)]. When the path of the throughflow is wholly or mainly in a plane perpendicular to the rotation axis, the device is termed a radial flow turbomachine [e.g., Figure 1.1(c)]. Mixed flow turbomachines are widely used. The term mixed flow in this context refers to the direction of the through-flow at the rotor outlet when both radial and axial velocity components are present in significant amounts. Figure 1.1(b) shows a mixed flow pump and Figure 1.1(d) a mixed flow hydraulic turbine.

One further category should be mentioned. All turbomachines can be classified as either impulse or reaction machines according to whether pressure changes are absent or present, respectively, in the flow through the rotor. In an impulse machine all the pressure change takes place in one or more nozzles, the fluid being directed onto the rotor. The Pelton wheel, Figure 1.1(f), is an example of an impulse turbine. [10]

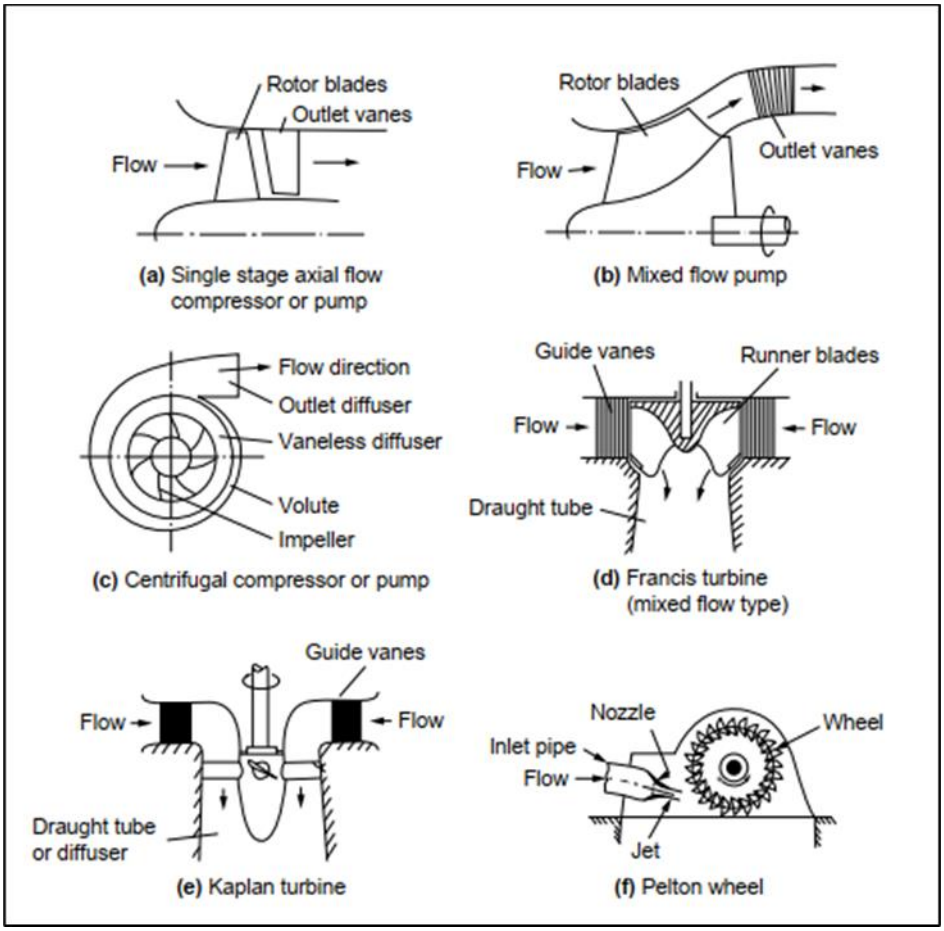

Figure 1-1 Examples of Turbomachines. [10]

1. 2 Classification of turbomachines

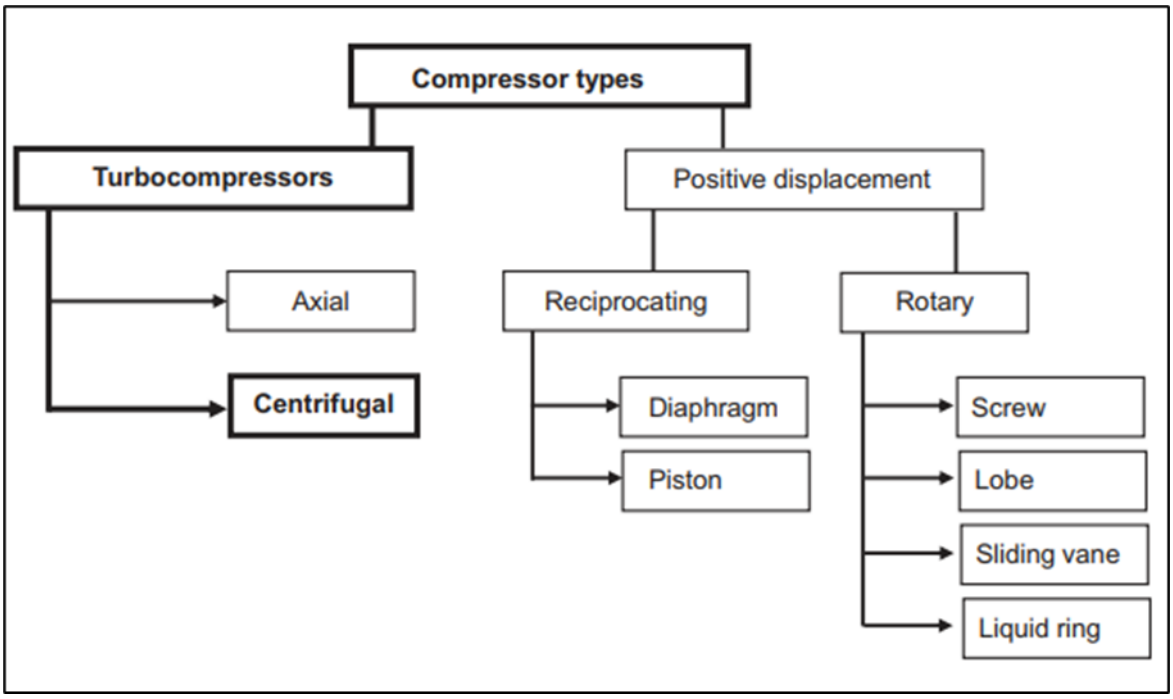

Figure 1-2 Categories of different compressor types.[12]

There are many ways to categorize turbomachinery. The most important are as follows:

1.2.1 Depending on the direction of the energy exchange

a) **Generating machines** that increase the energy of the fluid by supplying mechanical energy to the shaft of the machine (e.g., compressors, pumps, etc.).
b) **Driving machine:** means a device that continuously converts the energy of a fluid into mechanical power.

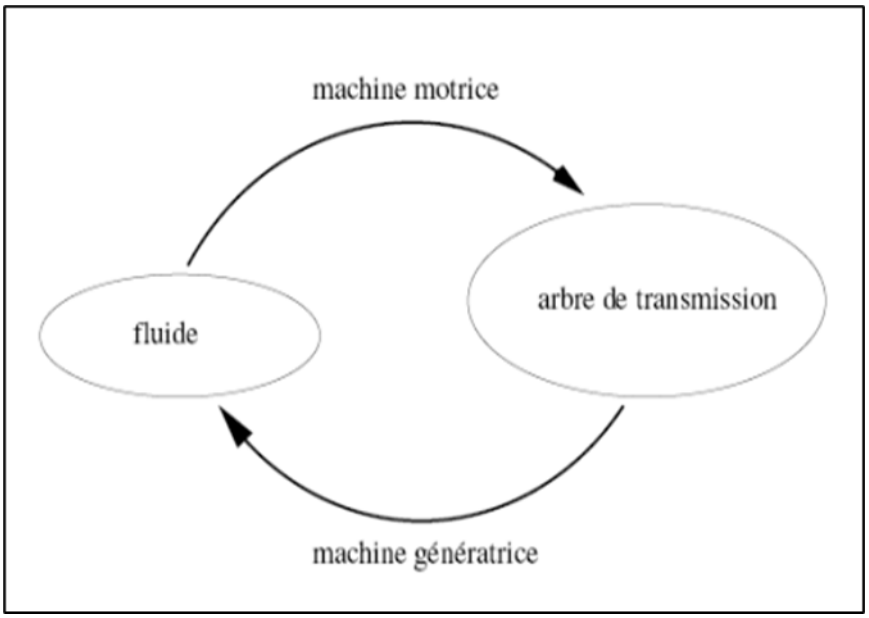

Figure 1-3 Energy transfer in a turbomachine.

1.2.2 Depending on the nature of the fluid

a) **Compressible fluid machines:** The density of the fluid is variable (generally gases), e.g., compressor, turbine, etc.
b) **Machines with incompressible fluids:** The density of the fluid is constant (generally liquids), e.g., water vane pumps, etc.

1.2.3 Depending on the flow trajectory

a) **Axial machines:** Axial machines belong to a class of turbomachinery where the fluid being processed, whether liquid or gas, primarily moves along the axis of rotation, parallel to the rotor's axis. These machines consist mainly of two components: the rotor and the stator. Their function involves interacting with the fluid to either extract energy from it, as turbines do, or to add energy to it, as compressors and pumps do.
b) **Centrifugal machines:** Centrifugal machines are vital devices that harness centrifugal force to move and manipulate fluids, increasing their pressure and velocity. These machines feature a rotating impeller that imparts kinetic energy to the

fluid, which is then directed by a casing or diffuser to convert this kinetic energy into pressure energy efficiently. There are various types of centrifugal machines tailored to different applications (Centrifugal Pumps, Centrifugal Compressors, Centrifugal Fans). Operating on fluid mechanics principles, these machines handle high flow rates and generate significant pressure increases, making them indispensable in sectors such as water treatment, chemical processing, aerospace, automotive, and HVAC. Their efficiency and capability in energy transformation ensure their critical role in modern engineering and industrial processes.

c) **Mixed machines:** Mixed flow turbomachines represent a class of turbomachinery characterized by fluid flow possessing both axial and radial velocity components. Within these machines, fluid enters the rotor either axially and exits radially, or vice versa. The synergy of axial and radial flow enables mixed flow turbomachines to attain greater pressure rises compared to machines exclusively axial or radial in nature. Nonetheless, the design and analysis of mixed flow machines prove more intricate owing to the three-dimensional dynamics of the flow.

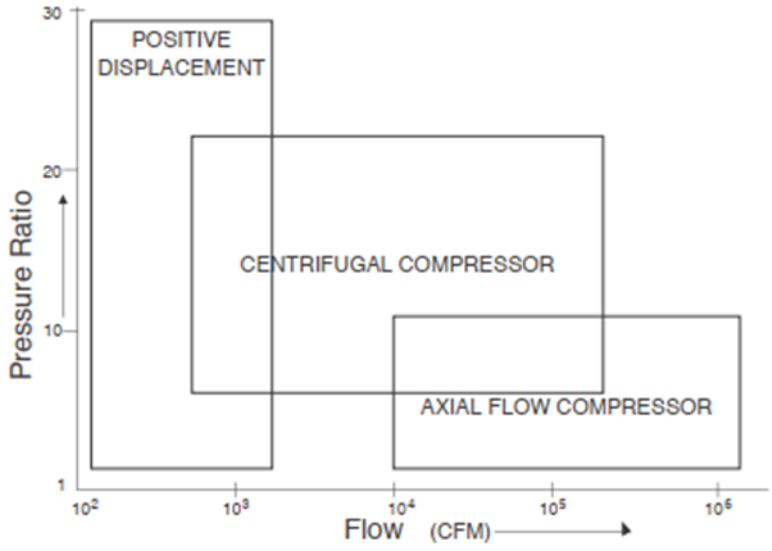

Figure 1-4 Performance characteristics of different types of compressors[11].

1. 3 Centrifugal compressor

Centrifugal compressors are widely used in the petrochemical industry due to their smooth operation, reliability, and ability to handle process fluctuations. They are also employed in small gas turbines. Their pressure ratios range from 1.3:1 per stage in process industries to 3-7:1 in gas turbines, and up to 13:1 in experimental models. Compressors with pressure ratios above 5:1 require special diffuser designs due to supersonic flow (M>1.0).

These compressors operate at higher speeds than others, ranging from 50,000-100,000 rpm in aerospace applications, while commercial units run below 20,000 rpm. As rpm increases, issues with bearing lubrication, vibration, and balancing become more prominent. They are well-suited for gas or steam turbine drives with variable-speed control and require smaller foundations due to the absence of inertia forces. Centrifugal compressors have high availability, often running 2-3 years without shutdown, and require less maintenance than reciprocating compressors.

The working principle involves fluid being forced through a rotating impeller, where velocity is converted to pressure in both the impeller and diffuser. Typically, half the pressure rise occurs in each component. The air enters axially and exits radially into a diffuser, with the inducer turning the flow 90º. In high-pressure compressors, vaneless spaces are used to reduce the Mach number before entering the diffuser. While centrifugal compressors are slightly less efficient than axial-flow compressors, they offer greater stability and a wider operating range.

1.3.1 The different characteristics of a compressor

- Isentropic compression efficiency :

Its expression is obtained from the law of the first principle of thermodynamics.

$$dH_t = dQ + dW_t \qquad 1\text{-}1$$

Expression of the enthalpy

$$dH_t = dh + d\left(v^2/_2\right) \quad 1\text{-}2$$

Case of isentropic transformation:

- Adiabatic. $dQ = 0$ 1-3
- reversible between two positions in the rotor.

$$dHt = dW_t \quad 1\text{-}4$$

$$dH_t = c_p.dT_t = \frac{1}{\rho_t}.dP_t + T_t.dS \quad 1\text{-}5$$

$$dW_{t1-2} = c_p.(T_{t2} - T_{t1}) = c_p.T_{t1}.(\frac{p_{t2}}{p_{t1}}^{\frac{\gamma-1}{\gamma}} - 1) \quad 1\text{-}6$$

$$dW_{t1-2} = c_p.T_{t1}.(\pi_c^{\frac{\gamma-1}{\gamma}} - 1) \quad 1\text{-}7$$

Isentropic efficiency can be defined as the ratio of the total entropy change in an isentropic transformation to the actual total entropy change:

$$\eta_{isc} = \frac{h_{t2isc} - h_{t1}}{h_{t2} - h_{t1}} = \frac{T_{t2isc} - T_{t1}}{T_{t2} - T_{t1}} = \frac{\pi_c^{\frac{\gamma-1}{\gamma}} - 1}{\tau_t - 1} \quad 1\text{-}8$$

And

$$\tau_t = \frac{T_{t2}}{T_{t1}} = \pi_c^{\frac{\gamma-1}{\gamma}} = \frac{p_{t2}}{p_{t1}}^{\frac{\gamma-1}{\gamma}} \quad 1\text{-}9$$

a) The compressor field curve:

In order to determine the behaviour of a radial compressor, different designs are usually compared on a non-dimensionalized basis. Following the procedure outlined by Dixon (1998), non-dimensionalized groups can be found based on various thermodynamic properties. These are the stagnation pressure ratio,$P_{oII}/P_{OI} = P_{Rstage,tot-tot}$ the change in stagnation temper- ature over inlet stagnation temperature, $\Delta T_o/T_{or}$ and the efficiency, η, of a turbomachine. Throughout this analysis subscript 0 denotes thermodynamic stagnation conditions, while subscript I and II denotes compressor stage inlet and outlet, respectively. The dimensionless parameters can be written as

$$\frac{P_{oII}}{P_{OI}}, \frac{\Delta T_o}{T_{OI}}, \eta = f\left\{\frac{\dot{m}\sqrt{RT_{OI}}}{D^2 P_{OI}}, \frac{ND}{\sqrt{RT_{OI}}}, R_e, \gamma\right\} \quad \textit{1-20}$$

where $\dot{m}$ denotes the mass flow, R the specific gas constant, D a characteristic diameter, N the rotating speed, R_e the Reynolds number and γ the ratio of specific heats. For a specific turbomachine handling a single fluid, the parameters D, R and γ can be regarded as constant. Further, if the turbomachine is operated at high speed (fully developed flow) the Reynolds number R_e can also be dropped.[19]

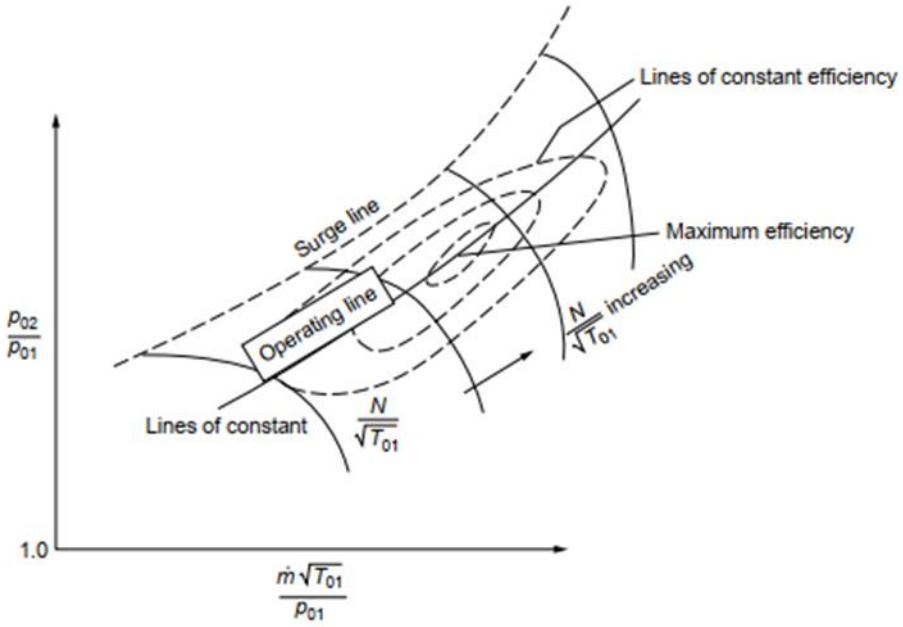

1-3 Characteristic curve of a compressor.[19]

b) Compressor stall:

The phenomenon of compressor stall is a highly intricate non-stationary occurrence that arises under specific operating conditions. It occurs when the airflow rate falls below a certain threshold for a given rotational speed, leading to significant periodic variations in pressure and flow rate at a varying frequency.

This phenomenon results in a cyclic reversal of airflow against the direction of flow, giving rise to two types of surging:

- Classical surging: characterized by oscillations in pressure and flow rate.

- Deep surging: where the flow rate oscillations are so pronounced that flow reversal occurs within the pressure system.

c) The operating range:

The operating range of a compressor is important and can be defined by the following relationship:

$$range = \frac{\dot{m}_{blocking} - \dot{m}_{stall}}{\dot{m}_{normal}} \qquad 1\text{-}41$$

d) Rotating stall :

Rotating stall can be defined as the formation of variable flow zones within the channels between blades. When the flow impacts a blade at an angle, the flow separates from the blade's suction side, leading to a reduction in flow rate. Consequently, the flow diverts towards the pressure side of the neighboring blade, which then experiences an excessive incidence and stalls as well. This process repeats itself and is linked to the rotational speed.

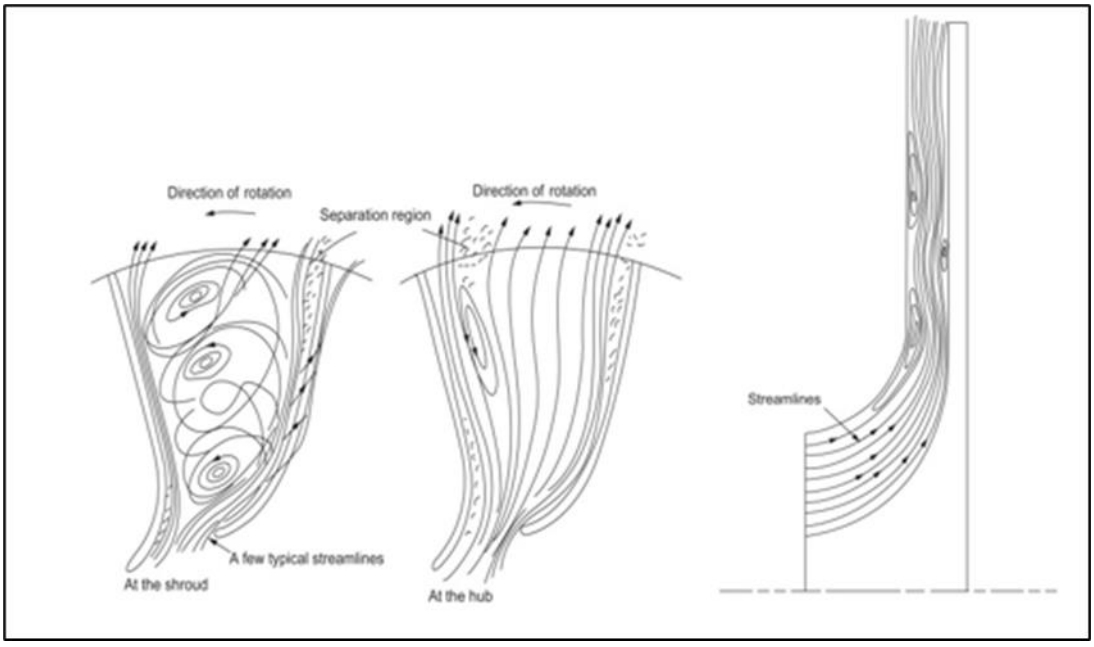

Figure 1-5 Presentation of the flow structure in the impeller of a centrifugal compressor.

1. 4 Reference planes in a centrifugal compressor

The flows in a centrifugal compressor are three-dimensional, viscous, turbulent and generally compressible fluid. here is an overview of the main reference planes used to describe the flow in a centrifugal compressor, based on the provided research results:

- **Meridional Projection**: The meridional projection is an axisymmetric cross-section of the compressor, perpendicular to the blades. It allows visualization of the geometry of both the stationary parts (casing, diffuser) and the moving parts (impeller), as well as the radial development of the flow.
- **Blade-to-Blade Plane**: The blade-to-blade plane is a cross-section perpendicular to the blades of the impeller, parallel to the axis of rotation. It allows visualization of the flow passage between the blades and the development of the flow in the tangential direction.
- **Orthogonal Cut:** The orthogonal cut is a cross-section perpendicular to both the axis of rotation and the blades of the impeller. It allows visualization of the flow in both the radial and tangential directions simultaneously.

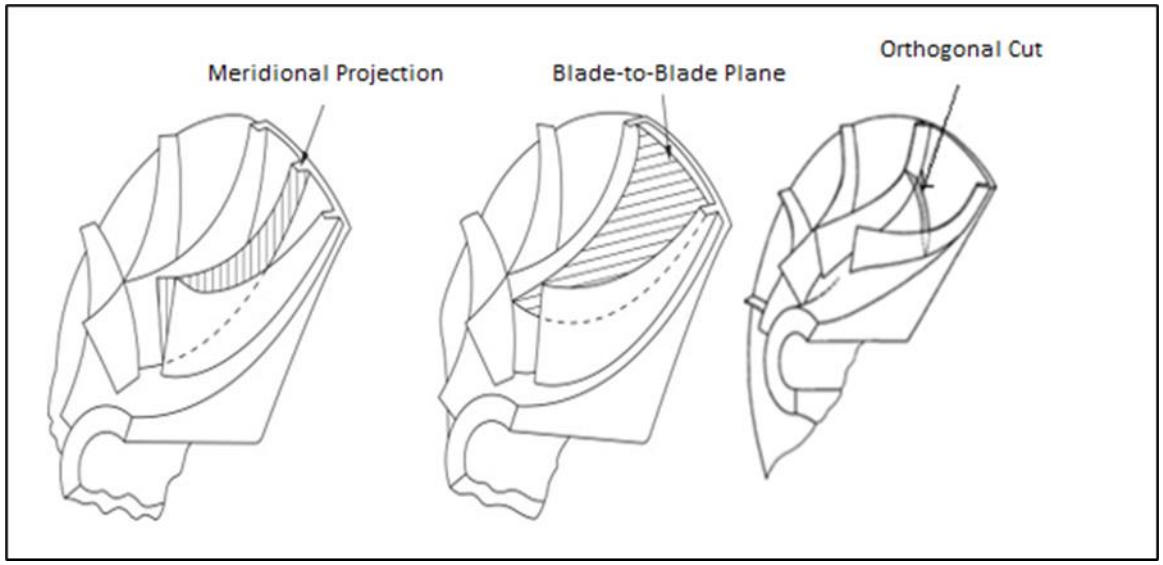

Figure 1-6 surfaces in the centrifugal compressor impeller.

Chapter 2 Mathematical Model

2. 1 Instantaneous Navier-Stokes equations

In the realm of turbulent flows, the enduring principles of classical continuum mechanics maintain their relevance. Thus, the foundational step in any numerical simulation of fluid dynamics is the invocation of the Navier-Stokes equations in their instantaneous manifestation, supplemented by the fluid's equation of state to ensure completeness. While strictly delineating variations in momentum, the Navier-Stokes equations are complemented by equations governing the conservation of mass and energy.

In the scenario of fluid flow characterized by viscosity, compressibility, and heat conduction, and where external volumetric forces such as gravity are disregarded, these equations assume the following form in their instantaneous expression:

$$\frac{\partial \rho}{\partial t} + \frac{\partial \rho u_j}{\partial x_j} = 0 \qquad 2\text{-}1$$

$$\frac{\partial \rho u_j}{\partial t} + \frac{\partial}{\partial x_j}\left(\rho u_i u_j + p\delta_{ij}\right) = \frac{\partial \tau_{ij}}{\partial x_j} + S_i \qquad 2\text{-}2$$

$$\frac{\partial \rho E}{\partial t} + \frac{\partial}{\partial x_j}\left[u_j(\rho E + p)\right] = \frac{\partial}{\partial x_j}\tau_{ij}u_i - \frac{\partial q_j}{\partial x_j} + S_E \qquad 2\text{-}3$$

Where ρ is the density, p the static pressure, u_i the i^{th} component of the velocity vector, τ_{ij} the viscous stress tensor, S_i source term of force, E the total energy per mass unit, S_E source term of energy, q_j the heat flux, and δ_{ij} the Kronecker tensor (i free index, $i \in \{3,2,1\}$ and j summation index $j \in \{3,2,1\}$, with $\delta_{ij} = 0$ for $i \neq j$ and $\delta_{ij} = 1$ for $i = j$).

S_i : source term which includes all volume force (gravite, centrifugal force, Coriolis force).

$$S_i = S_{i,Cor} + S_{i,cent} \qquad 2\text{-}4$$

In this system of equations, the total energy per mass unit is expressed from the internal energy e and the kinetic energy according to the relation:

$$E = e + \frac{1}{2}u_k u_k \qquad 2\text{-}5$$

$$\tau_{ij} = \mu(\frac{\partial u_i}{\partial x_j} + \frac{\partial u_j}{\partial x_i}) + \lambda(\frac{\partial u_i}{\partial x_j})\delta_{ij} \qquad 2\text{-}6$$

where μ and λ are related by:

$$3\lambda + 2\mu = 0 \quad (Hypothèse de Stokes) \qquad 2\text{-}7$$

q_j represents the components of the heat flux and is expressed as a function of the temperature gradient by Fourier's law of thermal conduction

$$q_j = -k\frac{\partial T}{\partial x_j} \qquad 2\text{-}8$$

where k is the coefficient of thermal conductivity. This coefficient is expressed as a function of dynamic viscosity using the Prandtl number:

$$Pr = \frac{\mu c_p}{k} = \gamma\frac{\mu c_v}{k} \qquad 2\text{-}9$$

where c_p and c_v represent the specific heats at constant pressure and volume respectively

And

$$\gamma = c_p \,/\, c_v \qquad 2\text{-}10$$

For air, under standard conditions, the Prandtl number Pr is 0.71, Changes in dynamic viscosity as a function of temperature are governed by Sutherland's law:

$$\mu(T) = \mu_0\left(\frac{T}{T_0}\right)^{3/2}\frac{T_0 + 110.4}{T + 110.4} = \frac{1.458 \times 10^{-6}T^{3/2}}{T + 110.4} \qquad 2\text{-}21$$

With $T0 = 273.15\ K$ and $\mu_0 = 1.711 \times 10 - 5\ kg.m^{-1}\ s^{-1}$

To take into account the variations in density and pressure associated with temperature variations, the system still requires knowledge of the state law. Considering air as a perfect gas, the equation of state is expressed as:

$$p = \rho rT = \rho(\gamma - 1)e \qquad 2\text{-}32$$

where r is related to the specific heats by Meyer's relation

$$r = c_p - c_v \qquad 2\text{-}43$$

2. 2 mathematical models

CFD (Computational Fluid Dynamics) mathematical models include several approaches to simulate turbulent flows. These models are categorized based on their ability to resolve different scales of turbulence.

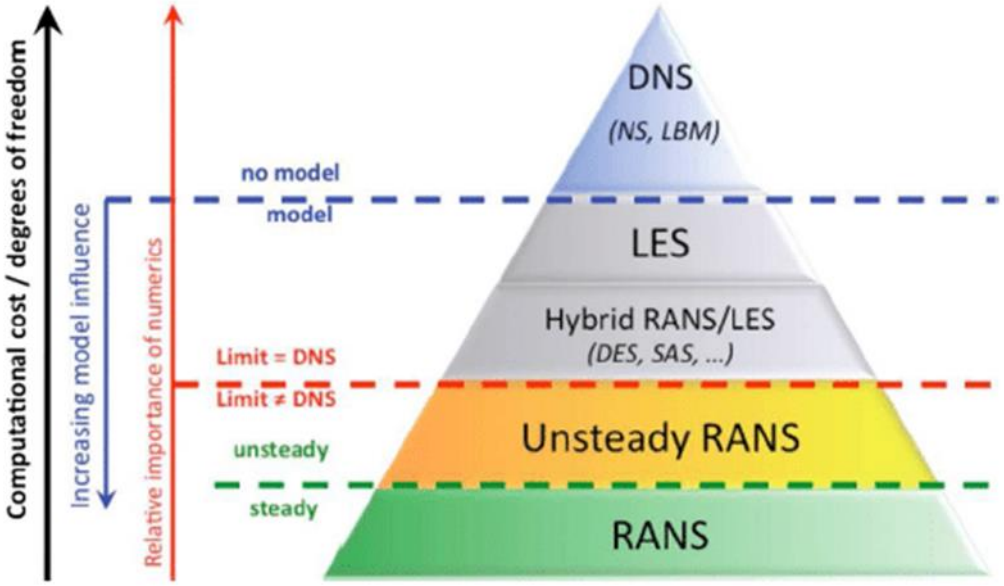

Figure 2-1 Classical CFD approaches for turbulent flow simulation

2.2.1 Direct Numerical Simulation (DNS)

Direct Numerical Simulation (DNS) is a computational approach in fluid dynamics that directly simulates fluid flows without employing any turbulence modeling. It relies on the numerical solution of the Navier-Stokes equations, which govern the motion of fluids. DNS is particularly effective for simulating flows with low Reynolds numbers, where the flow is laminar, or for highly turbulent flows where the turbulence can be resolved directly by the computational grid.

The DNS approach typically utilizes numerical methods such as the finite difference method or the finite element method. These methods discretize the Navier-Stokes equations, allowing for their numerical solution. Often, DNS is combined with other numerical techniques, such as Large Eddy Simulation (LES), to address flows where turbulence is not sufficiently resolved by the grid alone.

DNS has found extensive application across various fields, including aerospace engineering, chemical engineering, and environmental engineering. It is used to simulate complex fluid flows and to study the impacts of turbulence on flow behavior.

2.2.2 Reynolds-Averaged Navier-Stokes (RANS)

The Reynolds-Averaged Navier-Stokes (RANS) model represents a prevalent turbulence modeling paradigm within the realm of fluid dynamics, providing a streamlined framework to comprehend the intricate and unpredictable nature of turbulent motion. Grounded in the Reynolds-averaged Navier-Stokes equations, derived through temporal averaging of the governing Navier-Stokes equations, this model simplifies the complexity of turbulence, rendering the flow more amenable to analysis.

By segregating flow variables into mean (time-averaged) and fluctuating components. This averaging process effectively simplifies the complex behavior of turbulence, allowing for a more manageable representation of the flow. The RANS equations provide a practical means to predict the mean flow characteristics of turbulent flows, striking a balance between accuracy and computational efficiency.

The instantaneous field is decomposed into an average field $\bar{X}$ plus a fluctuating field X′. This is the Reynolds decomposition. Thus, for a quantity X:

$$X = \bar{X} + X' \qquad 2\text{-}54$$

Examples of Reynolds decomposition:

$$U = \bar{U} + U' \qquad 2\text{-}65$$

With

$$\bar{U} = \lim_{\Delta t \to \infty} \frac{1}{\Delta t} \int_{to}^{to+\Delta t} U(t)\, dt \qquad 2\text{-}76$$

Since the flow is compressible, we prefer to use the Favre average for the velocity u and the total energy E. The Favre mean is calculated from the Reynolds average. For a quantity A:

$$A = \tilde{A} + A'' \qquad 2\text{-}87$$

The application of Reynolds decomposition to the compressible Navier-Stokes equations does not therefore lead to a system of equations for the mean field which is formally identical to the original equations. To avoid this problem, we adopt the Favre decomposition, which is based on density-weighted averages.

The Favre average:

$$\bar{U} = \frac{\overline{\rho U}}{\bar{U}} \qquad 2\text{-}98$$

The decomposition is as follows:

$$U = \bar{U} + U' \qquad 2\text{-}109$$

$$\overline{\rho U} = \bar{\rho}\,.\,\bar{U} \qquad 2\text{-}20$$

$$\overline{\rho U'} = 0 \qquad 2\text{-}21$$

$$\overline{U'} \neq 0 \qquad 2\text{-}22$$

We can clearly see that the Favre average makes it possible to hide correlations involving fluctuations in density. This feature also allows the Favre formalism to retain the conservative form of the instantaneous equations. We obtain the following forms:

$$\frac{\partial \bar{\rho}}{\partial t} + \frac{\partial \bar{\rho} \tilde{u_j}}{\partial x_j} = 0 \qquad 2\text{-}23$$

$$\frac{\partial \bar{\rho} \tilde{u_j}}{\partial t} + \frac{\partial}{\partial x_j}\left(\bar{\rho} \tilde{u_i} \tilde{u_j}\right) = -\frac{\partial \bar{p}}{\partial x_i} + \frac{\partial}{\partial x_j}\left(\overline{\tau_{ij}} - \overline{\rho u_i'' u_j''}\right) \qquad 2\text{-}24$$

$$\frac{\partial \bar{\rho}\tilde{E}}{\partial t} + \frac{\partial}{\partial x_j}(\bar{\rho}\tilde{E}\tilde{u_j}) = -\frac{\partial \bar{p}\tilde{u_j}}{\partial x_j} + \frac{\partial}{\partial x_j}(\overline{\tau_{ij}}\tilde{u_j}) - \frac{\partial}{\partial x_j}(\overline{q_j} - \overline{\rho E'' u''_j}) \quad 2\text{-}25$$

$$\overline{\tau_{ij}} = \bar{\mu}\left(\frac{\partial \tilde{u_i}}{\partial x_j} + \frac{\partial \tilde{u_j}}{\partial x_i} - \frac{2}{3}\left(\frac{\partial \tilde{u_k}}{\partial x_k}\right)\delta_{ij}\right) \quad 2\text{-}26$$

$$\overline{q_j} = -\bar{k}\frac{\partial \tilde{T}}{\partial x_j} = -c_p\overline{\rho T'' u''_j} \quad 2\text{-}27$$

$$p = \bar{\rho} r \tilde{T} = \bar{\rho}(\gamma - 1)\tilde{e} \quad 2\text{-}28$$

$$\tilde{E} = \tilde{e} + \frac{1}{2}\tilde{u_k}\tilde{u_k} + k \quad 2\text{-}29$$

$$k = \frac{1}{2}u''_k u''_k \quad 2\text{-}30$$

2.2.2.1 Turbulence models

Turbulence models are mathematical constructs employed in Computational Fluid Dynamics (CFD) to account for the effects of turbulence in the simulation of fluid flows. These models are crucial for computing Reynolds stresses in turbulent flows, which are nonlinear components necessitating additional modeling to close the Reynolds-Averaged Navier-Stokes (RANS) equations for solution.

We are using ANSYS CFX which is a high-performance computational fluid dynamics (CFD) software widely used for simulating fluid flow and related phenomena. It offers a variety of turbulence models to accurately capture the complexities of turbulent flow. Some of the available turbulence models in ANSYS CFX:

k-ε model

The K-ε model is a two transport equation model to evaluate the vortex viscosity. It solves two partial differential equations to obtain the turbulent kinetic energy K and its dissipation ε, these equations are as follows:

$$\frac{\partial}{\partial t}(\bar{\rho}k) + \frac{\partial}{\partial x_j}\left(\bar{\rho}\,\tilde{u_j}\,k\right) = \bar{\rho}P - \bar{\rho}\varepsilon + \frac{\partial}{\partial x_j}\left[\left(\bar{\mu} + \frac{\bar{\mu}_t}{P_{rk}}\right)\frac{\partial k}{\partial x_j}\right] \qquad 2\text{-}31$$

$$\frac{\partial}{\partial t}(\bar{\rho}\varepsilon) + \frac{\partial}{\partial x_j}\left(\bar{\rho}\tilde{u_j}\varepsilon\right) = C_{\varepsilon 1}\frac{\bar{\rho}P\varepsilon^2}{k} - C_{\varepsilon 2}\frac{\bar{\rho}\varepsilon^2}{k} + \frac{\partial}{\partial x_j}\left[\left(\bar{\mu} + \frac{\bar{\mu}_t}{P_{r\varepsilon}}\right)\frac{\partial \varepsilon}{\partial x_j}\right] \qquad 2\text{-}32$$

where P is the turbulent kinetic energy production rate given by equation :

$$P = \bar{\vartheta_t}\left(\frac{\partial \tilde{u_i}}{\partial x_j} + \frac{\partial \tilde{u_j}}{\partial x_i} - \frac{2}{3}\frac{\partial \tilde{u_m}}{\partial x_m}\delta_{ij}\right)\frac{\partial \tilde{u_i}}{\partial x_j} - \frac{2}{3}k\frac{\partial \tilde{u_m}}{\partial x_m} \qquad 2\text{-}33$$

With the constants [15]:

$$C_\mu = 0.09, \qquad C_{\varepsilon 1} = 1.44, \qquad C_{\varepsilon 2} = 1.92, \qquad P_{rk} = 1.0, \qquad P_{r\varepsilon} = 1.3$$

Viscous effects are more important than turbulent effects in the vicinity of the wall. A wall function is therefore applied in this region and the turbulence model solves the field in the rest of the flow domain. In the wall function, the velocity scale is taken as $q = k^{0.5}$ and the length scale is modelled as:

$$l = \frac{C_\mu^{3/4}k^{3/2}}{\varepsilon} \qquad 2\text{-}34$$

k and ε are related by semi-empirical expressions to the friction speed u_τ:

$$k = \frac{u_\tau^2}{\sqrt{C_\mu}} \qquad 2\text{-}35$$

$$\varepsilon = \frac{C_\mu^{3/4}k^{3/2}}{ky} \qquad 2\text{-}36$$

The turbulent viscosity is expressed by:

$$\vartheta_t = \frac{C_\mu k^2}{\varepsilon} \qquad 2\text{-}37$$

In the standard wall law approach, the velocity profile is estimated from the wall to the first mesh using the following relationships:

$$u^+ = y^+ \quad for \quad y^+ < 11.5 \qquad 2\text{-}38$$

$$u^+ = \frac{1}{k} ln(Ey^+) \quad for \quad y^+ > 11.5 \qquad 2\text{-}39$$

where the constants k and E are determined experimentally and are 0.4 and 9.0 respectively. The wall law concept is valid in the case where the value of the distance from the centre of the first neighbouring cell to the wall is such that $y^+ > 30$.

k-ω model

The $K - \omega$ model is a model with two transport equations. The equations to be solved are: the turbulent kinetic energy equation k and the specific dissipation rate ω. The turbulent viscosity is expressed by : $\vartheta_t = C_\mu \frac{k}{\omega}$, and the transport equations are illustrated by the following equations:

$$\frac{\partial}{\partial t}(\bar{\rho}k) + \frac{\partial}{\partial x_j}(\bar{\rho}\tilde{u_j}k) = \bar{\rho}P - \bar{\rho}\omega k + \frac{\partial}{\partial x_j}\left[\left(\bar{\mu} + \frac{\bar{\mu}_t}{P_{rk}}\right)\frac{\partial k}{\partial x_j}\right] \qquad 2\text{-}40$$

$$\frac{\partial}{\partial t}(\bar{\rho}\omega) + \frac{\partial}{\partial x_j}(\bar{\rho}\tilde{u_j}\omega) = C_{\omega 1}\frac{\bar{\rho}P\omega}{k} - C_{\omega 2}\bar{\rho}\omega^2 + \frac{\partial}{\partial x_j}\left[\left(\bar{\mu} + \frac{\bar{\mu}_t}{P_{r\omega}}\right)\frac{\partial \omega}{\partial x_j}\right] \qquad 2\text{-}41$$

With the constants [16] :

$$C_\mu = 0.09, \qquad C_{\omega 1} = 0.555, \qquad C_{\omega 2} = 0.833, \qquad P_{rk} = 2.0, \quad P_{r\omega} = 2.0$$

The conditions for k and ω on the wall are:

$$k = 0 \quad for \quad y = 0 \qquad 2\text{-}42$$

$$\omega = 0.72\frac{\vartheta}{y^2} \quad for \quad y = y_1 \qquad 2\text{-}43$$

where y_1 is the normal distance from the wall to the centre of the first mesh. To obtain accurate solutions, the centre of the first mesh must be positioned closer to the wall. This model therefore requires a very fine mesh in the vicinity of the solid surfaces. A scaled distance close to unity $y^+ = 1$ is generally recommended.

SST-k-ω model

The results obtained by the $K-\omega$ model, according to Menter, are very sensitive to the value of ω imposed outside the boundary layer, so the $SST-K-\omega$ model represents an alternative to the $K-\omega$ model. It combines the two $K-\omega$ and $K-\varepsilon$ models. Two equations are solved, one for the specific dissipation ω and the other for the turbulence kinetic energy K, so the equations for K and ω are:

$$\frac{\partial}{\partial t}(\bar{\rho}k)+\frac{\partial}{\partial x_j}\left(\bar{\rho}\tilde{u_j}k\right)=\bar{\rho}P-C_u\bar{\rho}\omega k+\frac{\partial}{\partial x_j}\left[(\bar{\mu}+\sigma_k\bar{\mu}_t)\frac{\partial k}{\partial x_j}\right] \qquad 2\text{-}44$$

$$\frac{\partial}{\partial t}(\bar{\rho}\omega)+\frac{\partial}{\partial x_j}\left(\bar{\rho}\tilde{u_j}\omega\right)=\frac{\bar{\rho}P\gamma}{\bar{\mu}_t}-\beta\bar{\rho}\omega^2+\frac{\partial}{\partial x_j}\left[(\bar{\mu}+\sigma_\omega\bar{\mu}_t)\frac{\partial\omega}{\partial x_j}\right]+(1-F_1)2\bar{\rho}\sigma_{\omega2}\frac{1}{\omega}\frac{\partial k}{\partial x_j}\frac{\partial\omega}{\partial x_j} \qquad 2\text{-}45$$

The constants σ_k ,σ_ω ,β and γ are determined from the relation [17]:

$$\phi=F_1\phi_1+(1-F_1)\phi_2 \qquad 2\text{-}46$$

2.2.3 Unsteady Reynolds-Averaged Navier-Stokes (URANS)

The Unsteady Reynolds-Averaged Navier-Stokes (URANS) model is a turbulence modeling approach used in computational fluid dynamics (CFD) to simulate unsteady flows. It is an extension of the Reynolds-Averaged Navier-Stokes (RANS) model, which is widely used for steady-state flows. The URANS model is particularly useful for simulating flows that involve unsteady or transient phenomena, such as those encountered in turbomachinery, aerospace, and chemical processing applications.

The URANS model is based on the Reynolds-Averaged Navier-Stokes (RANS) equations, which are derived by averaging the Navier-Stokes equations over a period of time. This averaging process removes the high-frequency fluctuations in the flow, leaving only the low-frequency, large-scale motions. The RANS equations are then solved using a turbulence model, which provides the necessary closure to the equations by relating the Reynolds stresses to the mean velocity and pressure fields.

The URANS model is similar to the RANS model in that it also uses a turbulence model to close the equations. However, unlike the RANS model, which assumes a steady-state flow, the URANS model allows for unsteady flows by incorporating time-dependent

terms in the equations. These terms account for the unsteady nature of the flow, such as the effects of turbulence and the movement of the flow over time.

The URANS model is widely used in CFD simulations due to its ability to capture the unsteady behavior of complex flows. It is particularly useful for simulating flows that involve unsteady or transient phenomena, such as those encountered in turbomachinery, aerospace, and chemical processing applications. The URANS model is also used in conjunction with other turbulence models, such as Large Eddy Simulations (LES) and Direct Numerical Simulations (DNS), to provide a more detailed understanding of the flow behavior.

2.2.3.1 Differences between RANS and URANS models

The main difference between the Reynolds-Averaged Navier-Stokes (RANS) model and the Unsteady Reynolds-Averaged Navier-Stokes (URANS) model lies in the way they handle the temporal derivative of velocity components. The RANS model does not account for this derivative, whereas the URANS model does.

In the RANS model, the flow is assumed to be steady-state, and the equations are solved by averaging the Navier-Stokes equations over time. This approach is suitable for flows that are temporally stationary, such as those encountered in many industrial applications. However, it is not suitable for flows that involve unsteady or transient phenomena, such as those encountered in turbomachinery, aerospace, and chemical processing applications.

The URANS model, on the other hand, is an extension of the RANS model that allows for the inclusion of unsteady terms in the equations. This is achieved by retaining the temporal derivative of velocity components in the URANS equations. This allows the model to capture the unsteady behavior of the flow, which is particularly important in applications where the flow is not temporally stationary.

2.2.4 Large Eddy Simulation (LES)

Turbulent flow is a system with a wide range of length and time scales. Analysis of an energy spectrum shows this to be true for all turbulent flows. Numerical simulation of turbulence must therefore be able to capture all the scales involved. However, the limited power of computers means that not all these scales can be represented. This led to the development of the large-scale simulation method. This method directly simulates the large turbulent scales, while the small structures are modelled. In other words, the large-scale simulation approach consists of decomposing the energy spectrum of a turbulent flow into two main parts: the first is that of the large scales, whose spatial and temporal evolution is simulated using the filtered Navier-Stokes equations, while the second part consists of the small scales. These small scales in fact represent the part of the energy spectrum not resolved by the mesh and therefore require appropriate modelling to take account of its influence on the large-scale structures.

This section describes the concept of filtering which makes it possible to distinguish large scale eddies from small scale eddies. As we might expect, the distinction between large and small scales is directly linked to the size of the mesh used in the simulations. Schematically, Figure 2-1 illustrates this distinction for a given mesh size. We can see that the small unresolved scales.

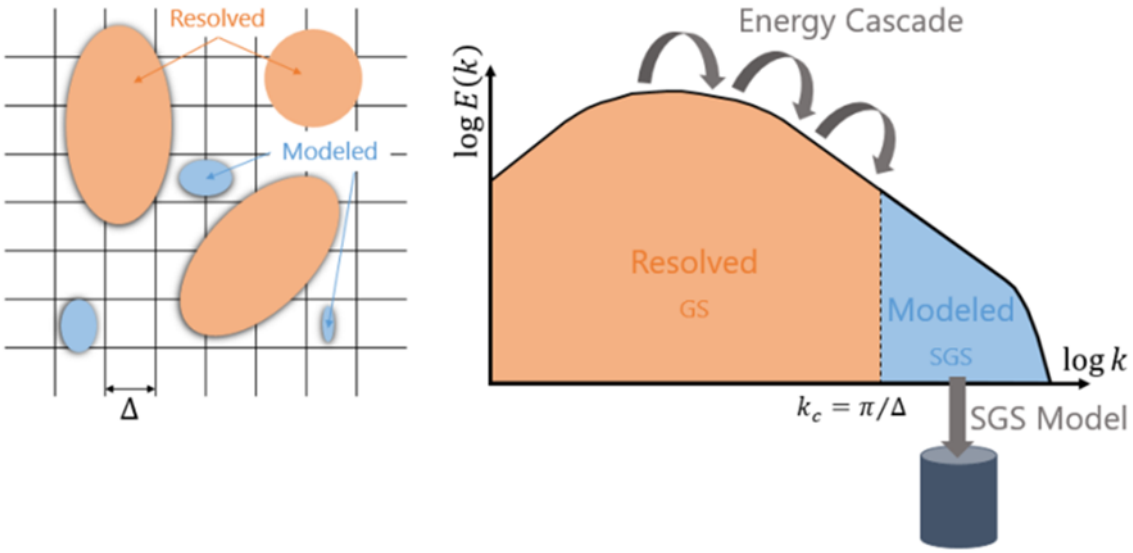

Figure 2-2 Representation of large scales resolved and small scales not resolved by the mesh.

represent eddy structures whose size is smaller than that of the mesh discretisation step, whereas the size of the large-scale eddies is larger than that of a mesh cell these structures can therefore be solved numerically. This section also presents the large-scale momentum equation, known as the filtered Navier-Stokes equation. This section concludes by outlining the modelling features required to adequately represent unresolved small scales.

represent eddy structures whose size is smaller than that of the mesh discretisation step, whereas the size of the large-scale eddies is larger than that of a mesh cell these structures can therefore be solved numerically. This section also presents the large-scale momentum equation, known as the filtered Navier-Stokes equation. Also, this section concludes by outlining the modelling features required to adequately represent unresolved small scales.

2.2.4.1 Concept of filtering:

The reason behind the large-scale simulation method, which consists of capturing the large scales and modelling the small ones, is as follows: the large vortex structures contain the most energy and are therefore responsible for transporting the majority of the fields present within a flow. These structures are very different from one flow to another because they depend on the geometry being studied. On the other hand, small structures are much more universal and therefore easier to model. The initial problem is to distinguish between large and small scales. To do this, we introduce the notion of filtering. Thus, if we consider the turbulent field u_i we define the filtered field $\overline{u_i}$ as being:

$$\overline{u_i} = \int_D G(x, x')\, u_i(x')\, dx' \qquad 2\text{-}47$$

where D is the application domain and $G(x, x')$ is the filter function. The filtered field u_i, represents the large-scale field. It is therefore the filter function $G(x, x')$ which determines the portion of the fluctuations in the observed flow which is contained within the large scales. Note that the integral (2-46) is a convolution product consisting of selecting a certain frequency content of the u_i field.

In concrete terms, this eliminates the high-frequency components of the velocity field, without which an extremely fine mesh would have to be used to capture these high

frequencies. As Lesieur, 1994, points out: ‘’The action of this filter generates a fictitious flow which is almost identical to the real flow in the large scales above Δx, but has no fluctuations in the smaller scales‘’.

It is important to realise that the discretisation of the Navier-Stokes equations corresponds to implicit filtering. To illustrate this, let's take the example given by Rogallo and Moin, 1984. Let's imagine for a moment that we want to wants to evaluate the first derivative of a continuous function $u\,(x)$ using a centred second-order scheme. We see that this evaluation consists of calculating the exact derivative of a second continuous function which is the average of the first. Mathematically, this proposition is written as follows:

$$\frac{u(x+h)-u(x-h)}{2h}=\frac{d}{dx}\left[\frac{1}{2h}\int_{x-h}^{x+h}u\,(\xi)\,d\xi\right] \qquad \textit{2-48}$$

Expression (2-47) therefore illustrates that the discretisation used in numerical calculation eliminates all scales smaller than the discretisation step h. In other words, the discretisation of the equations implicitly generates a system of filtered equations.

Thanks to the example we have just illustrated, we can see that the notion of filtering is intrinsically linked to the discretisation method used. In the next section, we will examine this observation more clearly.

2.2.4.2 Filters

This section presents the filters most commonly used in large-Eddy Simulations. These are the low-pass filter or ‘’Fourier cutoff ’’, the Gaussian filter and the box filter.

2.2.4.3 Fourier cut-off

Fourier filter is simply defined in spectral space by

$$\hat{\mathrm{G}}(k)=\begin{cases}1\ if k\leqslant k_c\\ 0\ if\ not\end{cases} \qquad \textit{2-49}$$

Where $\hat{G}(k)$ is the Fourier transform of the filter function G(x, x') and where k and k_c represent the wavenumber and cut-off wavenumber respectively. The cut-off wave number is defined as follows:

$$\boldsymbol{k_c = \frac{\pi}{\Delta}} \qquad 2\text{-}50$$

where Δ is the width of the filter. The Fourier filter therefore eliminates the frequency content of the flow whose wavenumbers are greater than the cut-off wavenumber k_c. It is important to note that the wavenumber is proportional to a frequency and inversely proportional to a length scale. However, the Fourier filter has the disadvantage of being an oscillatory function in physical space (Schiestel, 1993). It is for this reason that this filter is used with spectral methods.

2.2.4.4 Gaussian filter

The Gaussian filter is defined in physical space as follows:

$$G(x) = \sqrt{\frac{6}{\pi\Delta^2}} e^{-(\frac{6x^2}{\Delta^2})} \qquad 2\text{-}51$$

This filter has the advantage of being a smooth function and includes a small portion of the small scales within the filtered field. It is also easy to use in both physical and spectral space, since in both physical and spectral domains the filter function is expressed as a normal function.

2.2.4.5 Box filter

Very simple to use, this filter was used in one of the first LES simulations by Deardoff, 1970. It simply consists of performing an average within the volume of a mesh cell in physical space. More specifically, the application of this filter to the turbulent field u_i results in the filtered quantity $\overline{u_i}$ defined as follows:

$$\overline{u_i} = \frac{1}{\Delta x_1 \Delta x_2 \, \Delta x_3} \int_{x_3-\Delta x_3/2}^{x_3+\Delta x_3/2} \int_{x_2-\Delta x_2/2}^{x_2+\Delta x_2/2} \int_{x_1-\Delta x_1/2}^{x_1+\Delta x_1/2} u_i \, dx_1 \, dx_2 \, dx_3 \qquad 2\text{-}52$$

where Δx_1, Δx_2 and Δx_3 define the sides of the discretisation volume. This type of filtering therefore only captures scales larger than the size of the volume under consideration. The box filter therefore accurately represents the implicit filtering of the equations by the discretisation scheme. It is therefore considered that this filter is used when finite difference, finite element or finite volume discretisation methods are employed. Note that whereas the Fourier filter represents an oscillatory function in physical space, the box filter represents an oscillatory function in spectral space.

2.2.4.6 Filter properties

Given that we decompose the instantaneous field u_i of a turbulent flow into a filtered part known as the large-scale part and a component corresponding to the small scales known as the sub-grid scale (SGS) part, the instantaneous field u_i can be written as follows:

$$u_i = \overline{u_i} + u_i' \qquad 2\text{-}53$$

With

u_i →instantaneous field quantity

$\overline{u_i}$ →filtered part of the field (large scales)

u_i' →part of the field on small scales

The properties of a filter are different from those of a Reynolds average. Unlike a Reynolds average, a filter operation satisfies the following rules:

$$\overline{\overline{u_i}} \neq \overline{u_i} \text{2-11} \qquad 2\text{-}54$$

$$\overline{u_i'} \neq 0 \text{ 2-12} \qquad 2\text{-}55$$

Large uncaptured structures are defined by $\overline{u_i'}$ and are expressed as follows:

$$\overline{u_i'} = \overline{u_i} - \overline{\overline{u_i}} \qquad 2\text{-}56$$

Graphically, equation (2-52) can be illustrated by examining the energy spectrum of a turbulent quantity u_i as shown in Figure 2-2 (Piomelli, 1994). This figure shows the energy

spectrum curves associated with the instantaneous field u_i, the filtered field $\overline{u_i}$ and the doubly filtered field $\overline{u_i}$. The more the $\overline{\overline{u_i}}$ field is filtered, the more the signal corresponding to it is attenuated: the various terms present in the Fourier series making up the signal to be filtered are therefore reduced with each filtering operation.

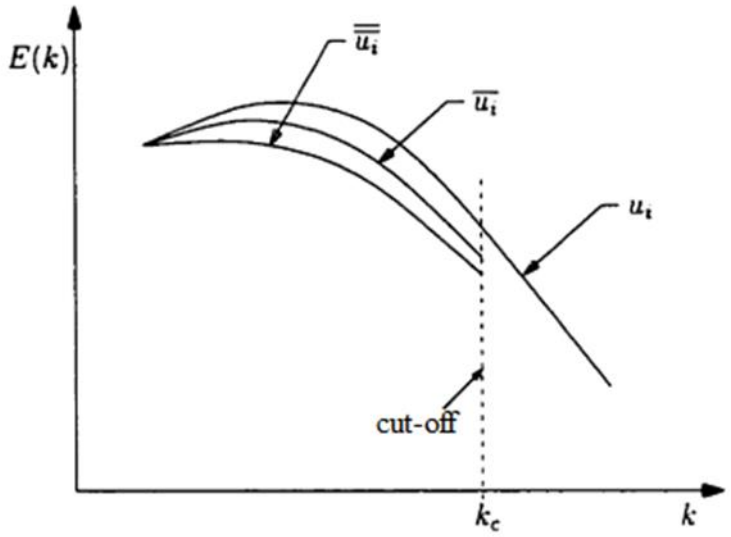

Figure 2-3 Energy spectrum with several filtering operations.

2.2.4.7 Filtering the Navier-Stokes equations

By using large-scale simulation, we aim to understand the evolution of the major structures responsible for transporting mass, momentum and energy. This involves filtering the various conservation equations governing fluid flow. For the purposes of this project, the fluid is assumed to be Newtonian, compressible and isothermal. By performing a filtering operation on the continuity equation and on the Navier-Stokes equation of instantaneous motion, we obtain the following filtered equations:

$$\frac{\partial \bar{\rho}}{\partial t} + \frac{\partial \bar{\rho}\overline{u_i}}{\partial x_i} = 0 \qquad 2\text{-}57$$

$$\frac{\partial \bar{\rho}\overline{u_i}}{\partial t} + \frac{\partial \bar{\rho}\overline{u_i}\overline{u_j}}{\partial x_j} + \frac{\partial \bar{p}}{\partial x_i} - \frac{\partial \overline{\tau_{ij}}}{\partial x_j} + \frac{\partial \tau_{ij}}{\partial x_j} = \overline{S_i} \qquad 2\text{-}58$$

where ρ is the density of the fluid, ϑ is the kinematic viscosity and $\bar{p}$ is the pressure. Examination of equation (2.1) reveals that the main unknown in the problem is $\overline{u_i}$, the large-scale velocity field, and that in order to solve this equation the convection term must be

expressed as a function of the main unknown. To do this, we substitute the relation (2-53) into the filtered product of the instantaneous velocities $\overline{u_\iota u_j}$. After a few manipulations, we obtain the filtered Navier-Stokes equation:

$$\frac{\partial \bar{\rho}\bar{u_\iota}}{\partial t} + \frac{\partial \bar{\rho}\bar{u_\iota}\bar{u_j}}{\partial x_j} = -\frac{\partial \bar{p}}{\partial x_i} + \frac{\partial \overline{\tau_{\iota j}}}{\partial x_j} - \frac{\partial \tau_{ij}}{\partial x_j} + \overline{S_E} \qquad \textit{2-59}$$

where τ_{ij} represents the sub-grid stress tensor expressed as follows:

$$\tau_{ij} = \overline{\overline{u_\iota}\overline{u_j}} - \overline{u_\iota}\overline{u_j} + \overline{\overline{u_\iota}u_j'} + \overline{\overline{u_j}u_\iota'} + \overline{u_\iota' u_j'} \qquad \textit{2-60}$$

Equation (2-60) can also be expressed in simplified form:

$$\tau_{ij} = \overline{u_\iota u_j} - \overline{u_\iota}\overline{u_j} \qquad \textit{2-61}$$

Interactions between the large and small scales take place via the sub-grid constraints τ_{ij}. This sub-grid tensor appears when filtering non-linear convection terms. The sub-grid constraints are unknown in the equation of motion (2-59) and therefore require modelling.

2.2.4.8 Subgrid-scale models

Subgrid-scale models (SGS) are a crucial component of large eddy simulations (LES), as they account for the unresolved scales of turbulence that are not captured by the numerical grid. There are several types of SGS, each with its strengths and limitations. Here are some of the most common types of SGS used in ANSYS CFX :

Smagorinsky-Lilly model

The Smagorinsky-Lilly model is a prevalent eddy viscosity model employed in large eddy simulations (LES) for turbulent flows. It operates on the concept of eddy viscosity, a measure of the turbulent viscosity within the flow. While the Smagorinsky model is straightforward and easy to implement, it has some limitations. Specifically, it does not account for the backscatter of energy from small scales to large scales, potentially leading to an overestimation of turbulent viscosity in certain flow regions.

The Smagorinsky model could be summarised as:

$$\tau_{ij} - \frac{1}{3}\tau_{kk}\delta_{ij} = -2(C_s\Delta)^2|\bar{S}|S_{ij} \quad \textit{2-62}$$

In the Smagorinsky-Lilly model, the eddy viscosity is modeled by

$$\mu_{sgs} = \rho(C_s\Delta)^2|\bar{S}| \quad \textit{2-63}$$

Where the filter width is usually taken to be

$$\Delta = (Volume)^{\frac{1}{3}} \quad \textit{2-64}$$

And

$$\bar{S} = \sqrt{2S_{ij}S_{ij}} \quad \textit{2-65}$$

The effective viscosity is calculated from

$$\mu_{eff} = \mu_{mol} + \mu_{sgs} \quad \textit{2-66}$$

The Smagorinsky constant usually has the value:

$$C_s = 0.1 - 0.2 \quad \textit{2-67}$$

Dynamic subgrid-scale model

The Algebraic Dynamical Systems (ADS) model represents a more recent advancement in the field of machine learning. This model utilizes algebraic structures to represent the dynamics of complex systems. ADS models are particularly advantageous for modeling dynamic systems that involve recursive functions, making them applicable to a broad range of systems, including those in machine learning.

Filtering with the grid filter results in the normal LES equations, with τ_{ij} given by

$$\tau_{ij} = \left(u_i u_j\right)^r - u_i^r u_j^r \quad \textit{2-68}$$

Filtering again with the test filter results in a similar set of equations, but with a different subgrid-scale stress term, given by

$$T_{ij} = \left(u_i u_j\right)^{rt} - u_i^{rt} u_j^{rt} \qquad 2\text{-}69$$

where the superscript rt indicates grid filtering followed by test filtering. The two subgrid-scale stress terms are related by the Germano identity:

$$\mathcal{L}_{ij} = T_{ij} - \tau_{ij}^{t} \qquad 2\text{-}70$$

Where

$$\mathcal{L}_{ij} = \left(u_i^r u_j^r\right)^t - u_i^{rt} u_j^{rt} \qquad 2\text{-}71$$

Is the resolved turbulent stress. The Germano identity is used to calculate dynamic local values for C_s by applying the Smagorinsky model to both T_{ij} and τ_{ij}. The anisotropic part of $\mathcal{L}_{ij}$ is the represented as

$$\mathcal{L}_{ij} - \delta_{ij}\mathcal{L}_{kk}/3 = -2C_S M_{ij} \qquad 2\text{-}72$$

Where

$$M_{ij} = (\Delta^t)^2 |S^{rt}| S_{ij}^{rt} - (\Delta^r)^2 \left(|S^r| S_{ij}^r\right)^t \qquad 2\text{-}73$$

C_s may now be computed as

$$C_S^2 = -\frac{1}{2}\frac{\mathcal{L}_{kl} S_{kl}^r}{M_{mn} S_{mn}^r} \qquad 2\text{-}74$$

In practice, ADS requires stabilization. Often, this has been done by averaging C_s in a homogeneous direction. In cases where this is not possible, local averaging has been used in place of an average in a homogenous direction.

Wall-adapting local eddy-viscosity (WALE) model

In the WALE model the eddy viscosity is modeled by:

$$\mu_t = \rho \Delta_s^2 \frac{\left(S_{ij}^d S_{ij}^d\right)^{3/2}}{\left(\overline{S}_{ij}\overline{S}_{ij}\right)^{5/2} + \left(S_{ij}^d S_{ij}^d\right)^{5/4}} \qquad 2\text{-}75$$

$$\Delta_s = C_w V^{1/3} \qquad 2\text{-}76$$

$$S_{ij}^{d} = \frac{1}{2}\left(\overline{g}_{ij}^{2} + \overline{g}_{ji}^{2}\right) - \frac{1}{3}\delta_{ij}\overline{g}_{kk}^{2} \quad \textit{2-77}$$

$$\overline{g}_{ij} = \frac{\partial \overline{u_i}}{\partial x_j} \quad \textit{2-78}$$

$$\Delta_s = C_w V^{1/3} \quad \textit{2-79}$$

$$S_{ij}^{d} = \frac{1}{2}\left(\overline{g}_{ij}^{2} + \overline{g}_{ji}^{2}\right) - \frac{1}{3}\delta_{ij}\overline{g}_{kk}^{2} \quad \textit{2-80}$$

$$\overline{g}_{ij} = \frac{\partial \overline{u_i}}{\partial x_j} \quad \textit{2-81}$$

$$\overline{g}_{ij}^{2} = \overline{g}_{ik}\overline{g}_{kj} \quad \textit{2-82}$$

Where S_{ij} is the rate-of-strain tensor for the resolved scale defined by

$$\overline{S_{ij}} = \frac{1}{2}\left(\frac{\partial \overline{u_i}}{\partial x_j} + \frac{\partial \overline{u_j}}{\partial x_i}\right) \quad \textit{2-83}$$

Where the constant $C_w = 0.325$

2.2.4.9 Characteristics of a subgrid-scale model

A sub-grid scale model in large eddy simulation (LES) is designed to account for the effects of smaller-scale turbulence that are not captured by the grid resolution. The characteristics of an SGS model can vary based on the specific application and the type of turbulence being modeled. Below are some general characteristics of SGS models:

1. **Grid Resolution Dependence:**

SGS models are typically dependent on grid resolution, meaning their performance and accuracy can significantly vary with the size of the grid cells used in the simulation. This dependency arises because SGS models are intended to represent the effects of smaller-scale turbulence that the grid does not resolve.

2. **Non-locality:**

SGS models often incorporate non-local effects, meaning the model's behavior is influenced by the state of the flow at locations beyond the current grid cell. This is particularly important in turbulent flows where smaller-scale turbulence can substantially impact larger-scale flow behavior.

3. **Non-linearity:**

SGS models can exhibit non-linearity, where the model's output may depend on the square or higher powers of the input variables. This non-linearity is crucial for capturing the complex interactions between smaller-scale turbulence and larger-scale flow.

4. **Turbulence Model Classification and Blending:**

Some SGS models, particularly those leveraging machine learning, can classify and blend different turbulence models based on local flow conditions. This adaptability enhances the model's accuracy by responding to changing flow conditions.

5. **Energy Dissipation Rate Modeling:**

SGS models can be designed to model the energy dissipation rate, which is the process by which energy transfers from larger-scale flow to smaller-scale turbulence. This is especially important in high Reynolds number flows, where the energy dissipation rate significantly impacts flow behavior.

6. **Fractal Interpolation:**

Certain SGS models, such as the fractal sub-grid scale model, employ fractal interpolation techniques. These models reconstruct the sub-grid velocity field using the filtered values on the LES coarse grid through fractal interpolation. The characteristics of the reconstructed signal depend on the stretching parameters, which relate to the fractal dimension of the signal.

7. **Dynamic Structure:**

Some SGS models incorporate dynamic structures that change over time and space. This feature is essential for capturing the complex interactions between smaller-scale turbulence and larger-scale flow.

8. A Priori and A Posteriori Testing:

SGS models are typically validated using a combination of a priori and a posteriori methods. A priori testing evaluates the model's performance based on its theoretical properties and the flow characteristics being modeled. A posteriori testing assesses the model's performance based on its ability to accurately predict flow behavior in specific simulations.

These characteristics outline the general attributes of SGS models in LES. The specific features of any given SGS model will depend on its application, the type of turbulence being modeled, and the model's design intricacies.

2.2.4.10 Wall modelling

Turbulent flows are significantly influenced by the presence of solid walls. In areas very close to the walls, viscosity effects are created, reducing fluctuations in tangential velocities (parallel to the wall). Outside this zone, turbulence appears more rapidly as a result of the production of turbulent kinetic energy due to the mean velocity gradient. A number of experiments have shown that the near-wall region can be subdivided into two layers: the innermost layer and the viscous sublayer, known as laminar flow, which are almost identical. Molecular viscosity plays a dominant and important role in heat transfer, further from the wall in the logarithmic layer turbulence dominates the mixing process, however there is a region in the logarithmic layer called the buffer layer where the effects of molecular viscosity and turbulence are of equal importance. The figure below illustrates the subdivisions of the region near the wall.

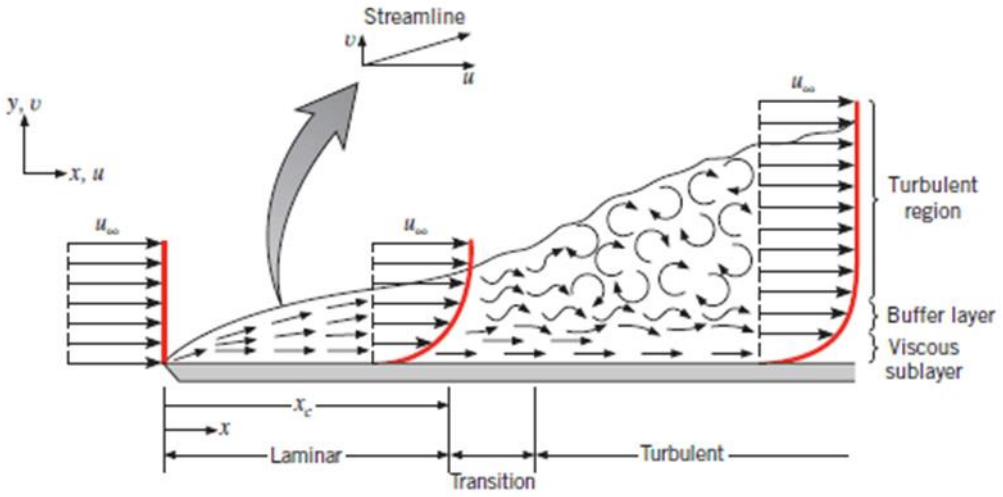

Figure 2-4 Boundary layer different zones

2.2.4.11 Wall treatment

The treatment of the wall region is very important for the numerical simulation of turbulent flow. Two approaches are commonly used to model the flow in this region.

The first approach is to solve the equations of the problem down to the solid wall on which the boundary condition is applied (called the near wall).

The other alternative that can be considered is to stop the calculation at a certain distance from the wall and use a wall law to link the calculated region to the wall (called the wall law), in which case the wall law is not used to solve the flow but rather to calculate the appropriate boundary conditions to be applied at the first node.

The law approached in ANSYS CFX is an extension of the LAUNDER and Spalding method, in the logarithmic region the tangential velocity near the wall is related to the shear wall τ_ω by means of a logarithmic relationship for the velocity near the wall is given by the following equation:

$$u^+ = \frac{u_t}{u_\tau} = \frac{1}{k} ln(y^+) + C \qquad 2\text{-}84$$

Where

$$y^+ = \frac{\Delta y u_\tau}{v} \qquad 2\text{-}85$$

And

$$u_\tau = \sqrt{\frac{\tau_\omega}{\rho}} \qquad 2\text{-}86$$

With:

u^+ is the velocity close to the wall, u_τ is the friction velocity, u_t is the known velocity tangent to the wall at a distance of Δy from the wall, y^+ is the distance from the wall, τ_ω is the wall shear stress, k is Von Karman's constant and C is a logarithmic constant depending on the roughness of the wall.

In terms of meshes, the two approaches for modelling close to the wall the choice of y^+ .

For the first approach (near wall) consists of solving the equations of the problem down to the interior of the viscous sublayer, in this case it is customary to use a mesh whose first node is very close to the wall, located at $y^+ \approx 1$. The $K-\omega$ and SST turbulence models are thus designed to resolve right up to the wall.

But the second approach (wall law) the first mesh must be located beyond the buffer subgrid $y^+ \geq 30$.The turbulence model $K-\varepsilon$ uses this method which reduces the number of computational meshes in the boundary layer.

2.2.4.12 Estimation de l'épaisseur de la couche limite

According to ANSYS CFX software, estimates will be based on correlations for a plate with Reynolds number :

$$Re_L = \frac{\rho\, u_\infty L}{\mu} \qquad 2\text{-}87$$

With a characteristic flow velocity u_∞, the Reynolds number based on chord length Re_L and the length of the plate L.

the shear stress c_f is given by :

$$c_f = 0.025 Re_x^{-1/7} \qquad 2\text{-}88$$

With Re_x Reynolds number based on the distance along the chord, x is the length of the plate.

The definition of Δy^+ for this estimate is :

$$\Delta y^+ = \frac{\Delta y \, u_\tau}{v} \qquad \textit{2-89}$$

With :

Δy : being the mesh spacing between the wall and the first wall node.

The shear stress is defined by :

$$C_f = 2\left(\frac{u_\tau}{u_\infty}\right)^2 \qquad \textit{2-90}$$

From the previous equation we can write the following equation:

$$\Delta y = L\,\Delta y^+ \sqrt{80}\, Re_x^{1/14} \frac{1}{Re_L} \qquad \textit{2-91}$$

For simplification purposes, it is assumed that: $Re_x = C\, Re_L$, where C represents the fraction, when Re_x is very small it is assumed that $C^{\frac{1}{14}} \approx 1$.

So the equation becomes (2-90) :

$$\Delta y = L \;\; \Delta y^+ \sqrt{80}\, Re_L^{-13/14} \qquad \textit{2-92}$$

Δy^+ Being the target to be reached at a distance x to have the first point in the viscous sub-layer.

Chapter 3 Simulation Steps

3. 1 Introduction

Most physical phenomena are governed by partial differential equations such as mass and heat transfer. Numerical methods are very useful in solving these partial differential equations, because the non-linearity of these equations and the complexity of the problems make them difficult to solve using analytical methods.

The development of numerical simulation tools and the power of computing resources have resulted in a large number of computer codes dedicated to the treatment of complex three-dimensional problems, particularly in the fields of fluid mechanics and turbomachinery. The best-known calculation codes are : ANSYS CFX, GAMBIT, FLUENT, STARCD, FEMLAB, NUMECA, etc. The software used in this work to numerically model the compressible flow in a centrifugal compressor is ANSYS-CFX.

3. 2 Finite volume Method

La méthode des volumes finis, largement décrite par Pantankar. S.V (1980), et introduite dans le domaine du calcul numérique des écoulements par Mc Donal (1971), Mac-Cormak et Paully (1972), pour la résolution des écoulements bidimensionnels, et par Rizi et Inouye (1973), pour les résolutions des écoulements tridimensionnels. Sa grande simplicité de mise lui a donné un essor depuis les années 1970-1980. Elle est l'origine de la majorité des codes de calculs.

L'avantage de la résolution par la méthode de volumes finis réside dans la limpidité de la discrétisation du domaine d'écoulement, ainsi que dans le caractère conservatif des équations, (tout ce qui sort d'un volume de contrôle entre dans l'autre).

The finite volume method is a numerical method for solving partial differential equations that arise in fluid mechanics. In FVM, the domain is divided into a finite number of control volumes, and the governing equations are integrated over each control volume. The conservation equations are then discretized using finite difference approximations, and the resulting algebraic equations are solved iteratively to obtain the solution.

3. 3 Process of a numerical simulation

A numerical simulation involves three primary steps: preparation, solution, and results processing.

a) **Pre-processing: Preparation of the Problem Data**
   - Geometry: Create or import the model geometry.
   - Mesh Generation: Discretize the geometry into a finite mesh.
   - Define Phenomena: Specify physical and chemical processes.
   - Fluid Properties: Assign material and fluid properties.
   - Boundary Conditions: Set up loads, supports, temperature, flow inlets, and outlets.

b) **Solution: Solving the Problem by a Numerical Method**
   - Select Method: Choose and configure the numerical method (e.g., finite element, finite volume).
   - Run Simulation: Execute the solver and monitor convergence, adjusting settings as needed.

c) **Post-processing: Visualization and Analysis of Results**
   - Visualize Domain and Mesh: Check the computational domain and mesh.
   - Plot Results: Generate velocity vectors, streamlines, and contour plots.
   - Surface Extraction: Analyze specific regions by extracting surfaces.
   - Graph Manipulation: Adjust plots for better visualization.
   - Export Figures: Save visualizations in formats like WMF and PS for reporting.

3. 4 Ansys CFX software flowchart

CFX, developed by ATA Technology, is a comprehensive suite of Computational Fluid Dynamics (CFD) tools. This software offers various multiphase models and numerical schemes, enabling users to model a wide range of fluid mechanics problems. Like many software packages, CFX includes several tools and modules for:

- Creating geometries.
- Generating meshes.
- Performing calculations

3.4.1 Creating geometries

The initial step involves defining the geometry of the centrifugal compressor wheel and diffuser using CFX-BladeGen, a specialized software tool for designing and analyzing turbomachinery blades, including those for turbines, compressors, pumps, and fans. CFX-BladeGen is part of the ANSYS suite of computational fluid dynamics (CFD) tools.

Based on the geometrical coordinates of the hub, shroud, and blade provided by Ziegler (2002), the computational domain has been constructed for both the impeller and the vaned diffuser. Structured grids have been generated using Turbogrid for the following components, as shown in Figure 1: (A) a single channel of the impeller and a portion of the convergent duct, and (B) a single channel of the vaned diffuser and a portion of the vaneless diffuser.

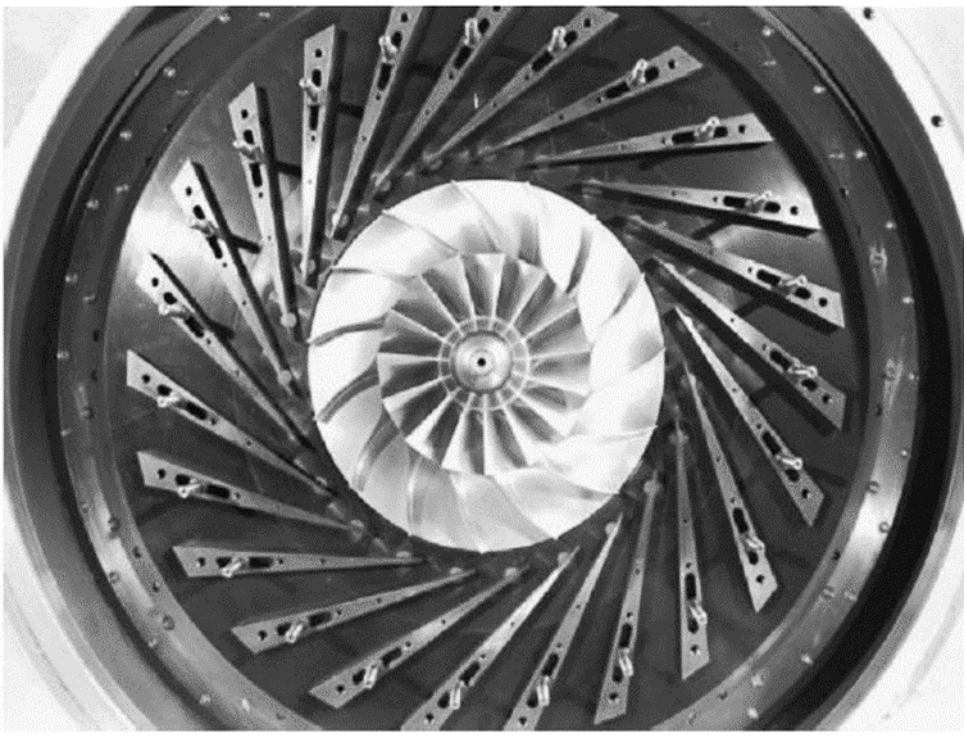

Figure 3-1 frontal view of the centrifugal compressor stage[14].

Table 1 Technical data of compressor for nominal speed and diffuser reference geometry [14]

Compressor		
Rotational speed at design point	N_0	35,200 rpm
Rotational speed at 80%	N_{80}	28,160 rpm
Maximum total pressure ratio	$\pi_{t,\,max}$	4.07
Maximum isentropic efficiency (tot/tot)	ηstt, max	0.834
Mass flow at maximum efficiency	$\dot{m}_{corr}$	1.956 kg/s
Impeller		
Exit radius	r_2	135 mm
Number of blades	Z_I	15
Blade backsweep angle at exit	β_{bs}	38˚
Diffuser		
Radial gap	r_4/r_2	1,10
Diffuse height	b	11.1 mm
Number of blades	Z_D	23
Vane angle	α_{4ss}	16.5˚
Vane wedge angle	α_V	6.615˚

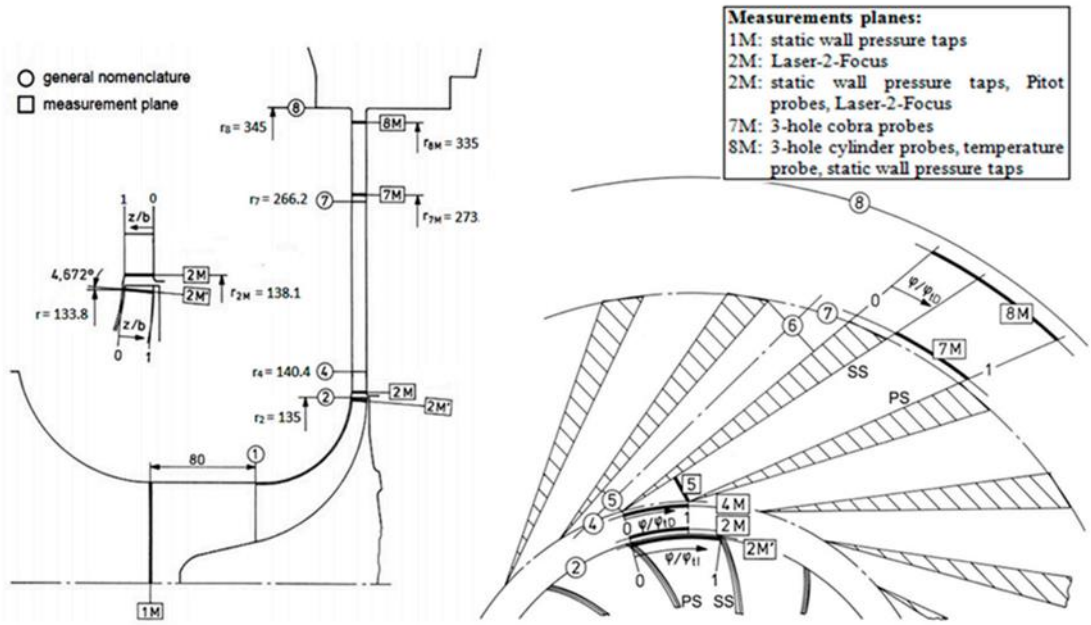

Figure 3-2 Measurement planes in meridional (left) and blade to blade (right) view [14].

First Step: Design of the Meridian Vein

Define the flow path in the meridional plane, which is essential for determining how the fluid will move through the impeller.

- **Curves for Hub and Shroud Surfaces:**
  - **Hub Curve:** This curve represents the inner boundary of the flow path, closest to the axis of rotation. It defines how the fluid enters and moves near the central part of the impeller.
  - **Shroud Curve:** This curve represents the outer boundary of the flow path, away from the axis of rotation. It defines how the fluid exits and moves near the outer edges of the impeller.
- **Types of Curves:**
  a) **Bézier Curve with Four Control Points:** A cubic Bézier curve uses four points to define its shape. The curve starts at the first point, is pulled towards the second and third points (but does not necessarily pass through them), and ends at the fourth point.

Control Points: These are the points that influence the shape of the curve. Moving these points changes the curvature, allowing for smooth transitions and specific shapes needed for efficient flow.

b) **Bézier Curve with (N) Control Points:** This is a general form of the Bézier curve that can have any number of control points (N). More control points provide greater flexibility and control over the curve's shape.

Flexibility: This allows for more complex shapes that can better fit specific design requirements.

c) **B-spline Curve with (N) Control Points:** B-spline curves offer even greater flexibility and control. Unlike Bézier curves, which are influenced by all control points, B-splines allow for local control.

Local Control: Adjusting one control point affects only a portion of the curve, making it easier to refine specific segments without altering the entire curve.

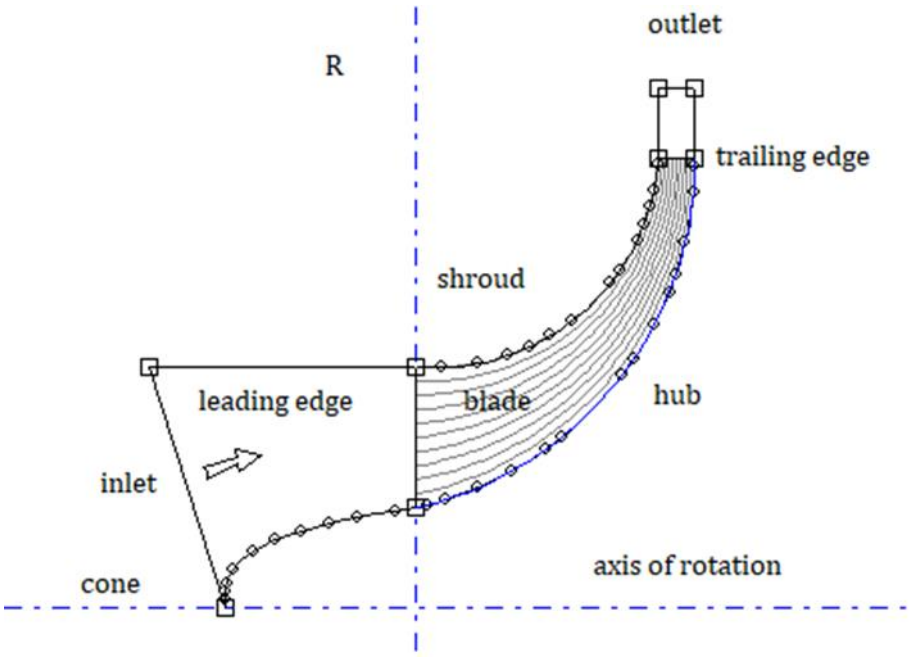

Figure 3-3 Meridian plane of rotor.

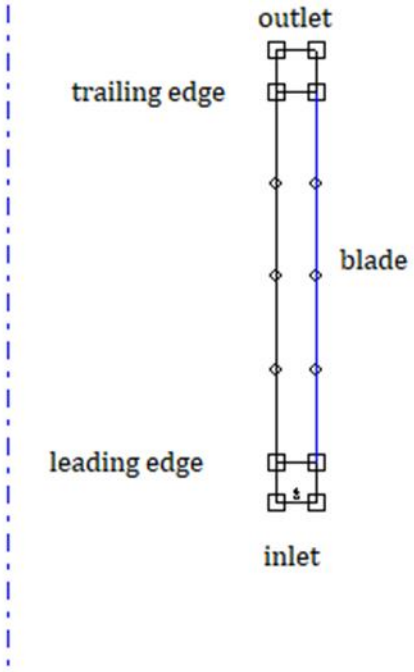

Figure 3-4 Meridian plane of stator.

Second Step: Define Pitch Angles and Recovery Angle

Precisely define the blade's orientation and recovery characteristics to optimize fluid flow.

- **Pitch Angles (β):** These angles describe how the blades are tilted relative to the flow direction at various points along the impeller's length.
  Function of Meridian Distance: The pitch angles are not constant but vary along the length of the blade. This variation is critical for guiding the fluid efficiently through the impeller.
- **Recovery Angle (Θ):** This angle pertains to how the blade recovers and redirects the flow. It affects the aerodynamic performance and energy conversion efficiency.
- **Conformal Transformation:**
  - Transformation of Coordinates: Convert the coordinates from the original 3D frame (R(x,y,z)) to a reference frame (R(M′,Θ)), where M′ is the meridian distance and Θ is the angle.
  - Purpose: This transformation ensures that the blade angles are accurately represented and adjusted according to the meridian distance, providing a more precise design.

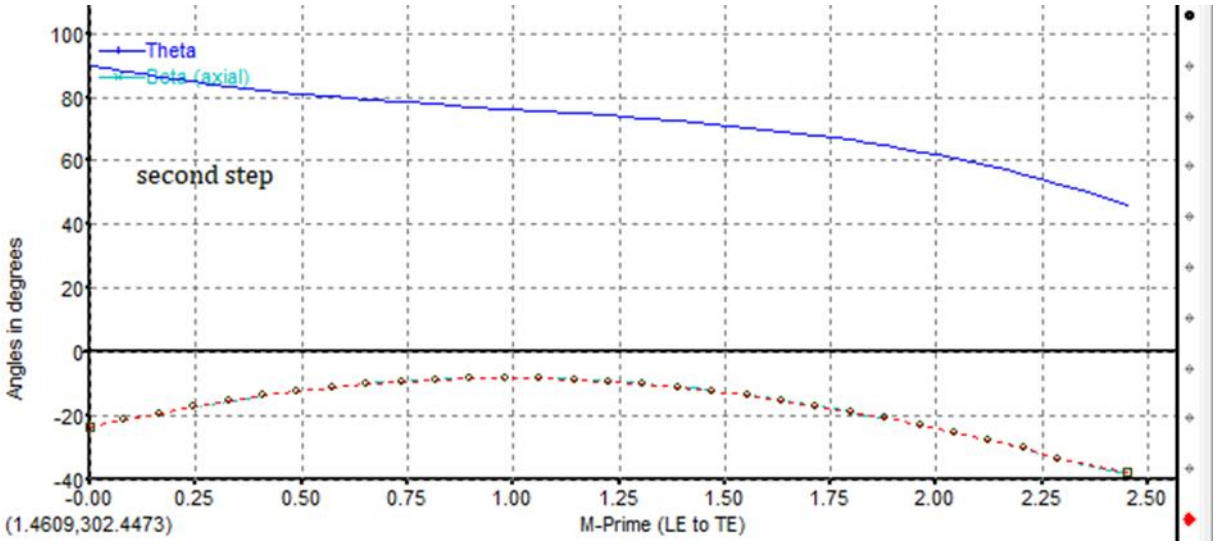

Figure 3-5 The pitch angles β and the recovery angle Θ of rotor.

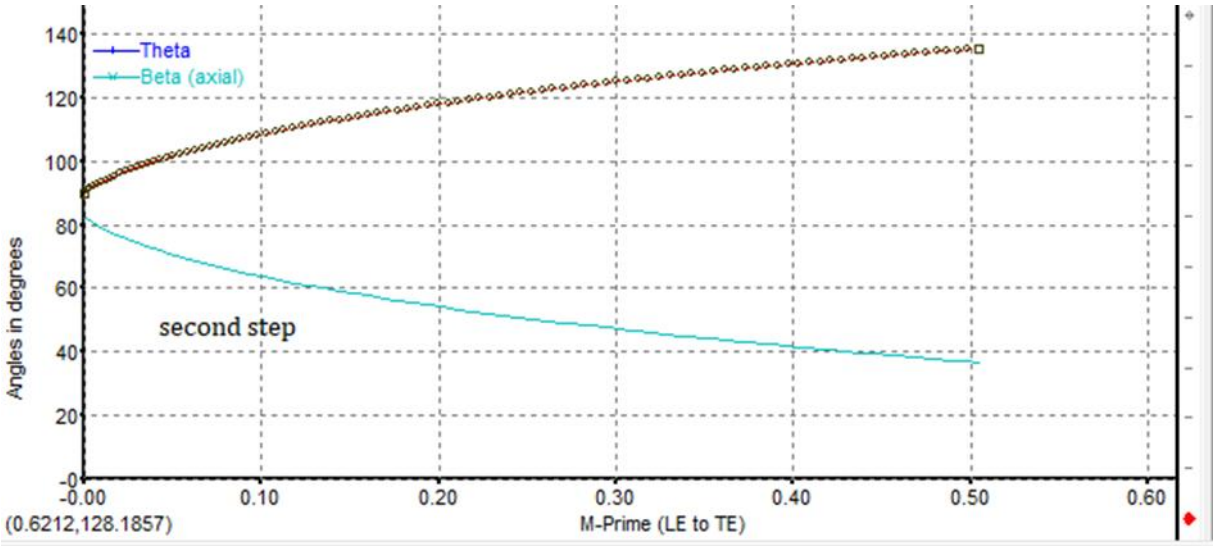

Figure 3-6 The pitch angles β and the recovery angle Θ of stator.

Third Step: Define Blade Thickness

Establish a profile for blade thickness to ensure structural integrity and aerodynamic performance.

- **Thickness Function:** Define how the thickness of the blade varies from the hub (inner part) to the shroud (outer part).

- **Importance:** Blade thickness affects both the mechanical strength and the aerodynamic characteristics. It must be optimized to prevent structural failure while maintaining efficient fluid flow.

Fourth Step: Create the 3D Geometric Shape

Integrate all the 2D design elements into a cohesive 3D model of the blade.

- **3D Construction:** Use the defined hub and shroud curves, pitch angles, recovery angles, and thickness profile to build the 3D geometry.
- **Visualization:** Employ 3D visualization tools to inspect the blade's shape, ensuring it meets design criteria and performance expectations.
- **Refinement:** Adjust the 3D model as necessary, based on simulation results and performance analysis.

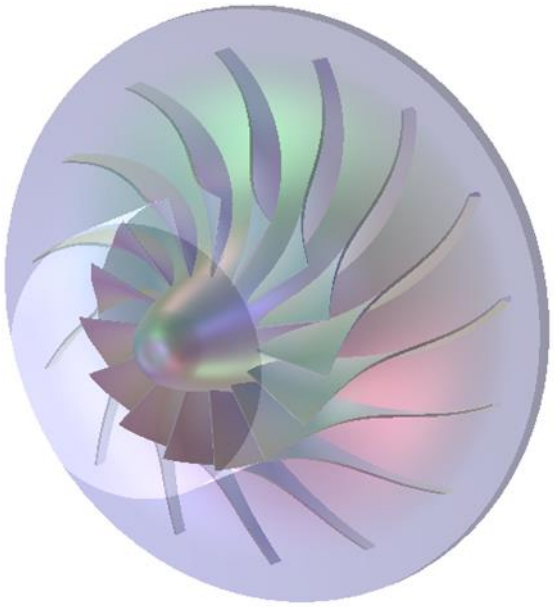

Figure 3-7 Presentation of rotor in 3D.

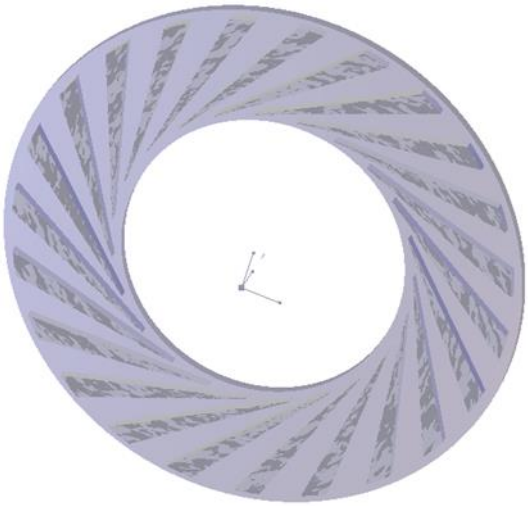

Figure 3-8 Presentation of stator in 3D.

3.4.2 Generating meshes

Before you can use ANSYS TurboGrid to create a mesh, you need to provide it with specific information. This includes the locations of the geometry files for the hub, shroud, and blades, the type of mesh topology you want to use, and how you want the mesh nodes to be distributed. All this information is stored in data objects known as CCL (CFX Command Language) objects. After you have configured these CCL objects, you can instruct ANSYS TurboGrid to generate the mesh.

ANSYS TurboGrid is a powerful tool that creates high quality meshes using Automatic Topology Meshing (ATM) technology. This technology ensures that the mesh fits smoothly and accurately to the blade geometry, resulting in a high-resolution mesh that supports fast and precise fluid dynamics analysis.

TurboGrid is used after the stator and rotor of the turbomachinery have been constructed. It takes the geometry created by BladeGen, which is the tool used to design the blades, and uses it to generate the mesh.

By providing the necessary information and following these steps, TurboGrid can efficiently produce high-quality meshes for accurate simulations of turbomachinery components.

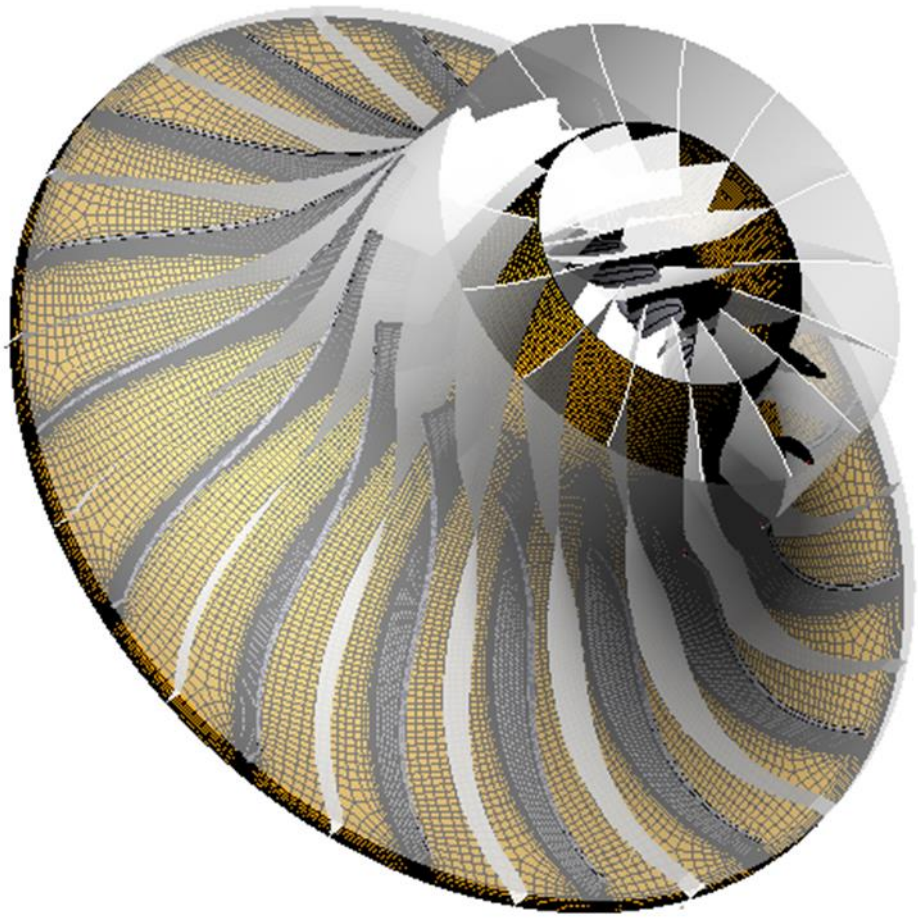

Figure 3-9 Mesh of rotor.

a) Unstructured mesh

The moving part, known as the rotor, and the fixed part, referred to as the diffuser, along with the various interactions between the rotating wheel and the casing, necessitate the use of an unstructured mesh. This requirement arises because the intersection zone of the two interfaces the moving parts and the fixed part-lies within the computational domain.Unstructured meshes are crucial in this context due to their flexibility in handling complex geometries and interactions. Unlike structured meshes that use a regular grid pattern, unstructured meshes can adapt more easily to the intricate and irregular shapes found where the rotor and diffuser meet. This ensures that the detailed interactions between the moving

rotor and the stationary casing are accurately captured in the simulation, leading to more precise modelling and analysis of the turbomachinery.

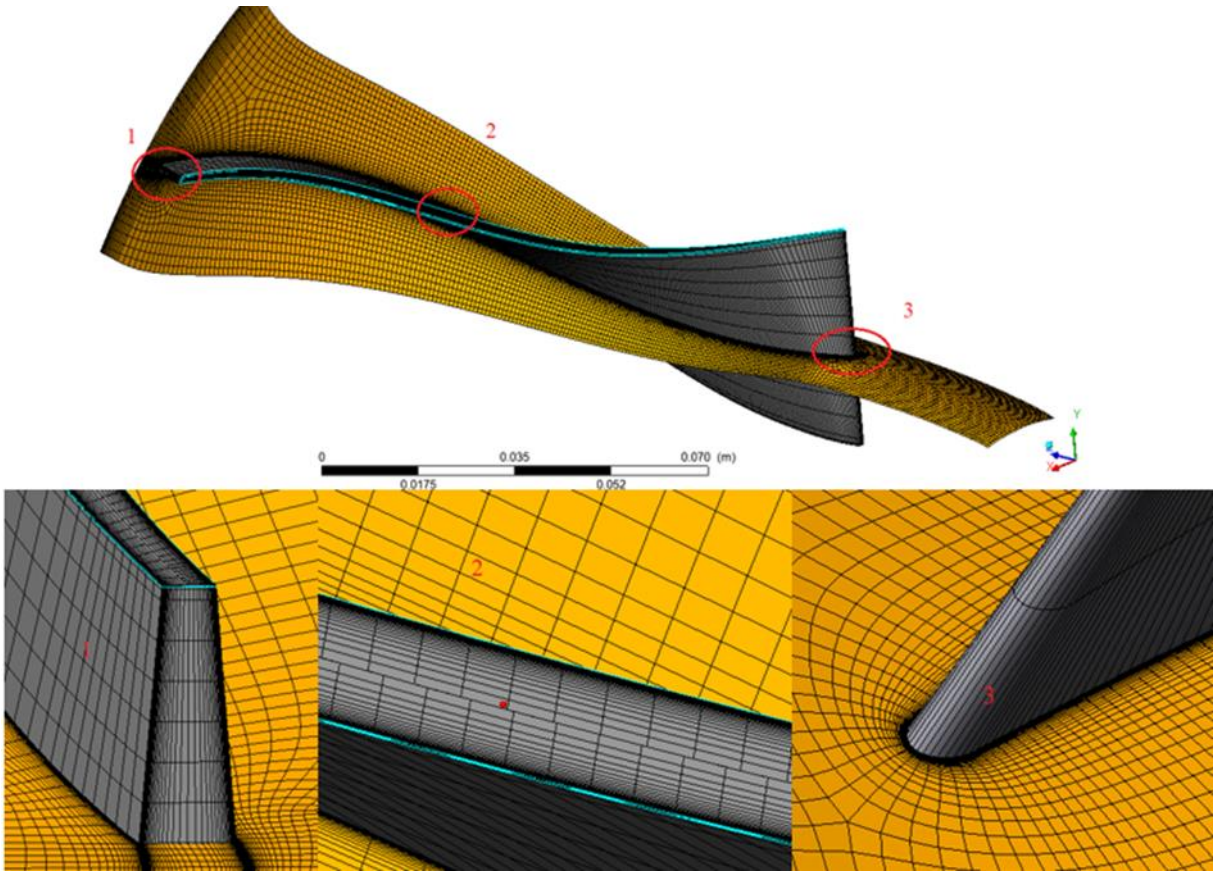

Figure 3-10 Impeller passage grid.

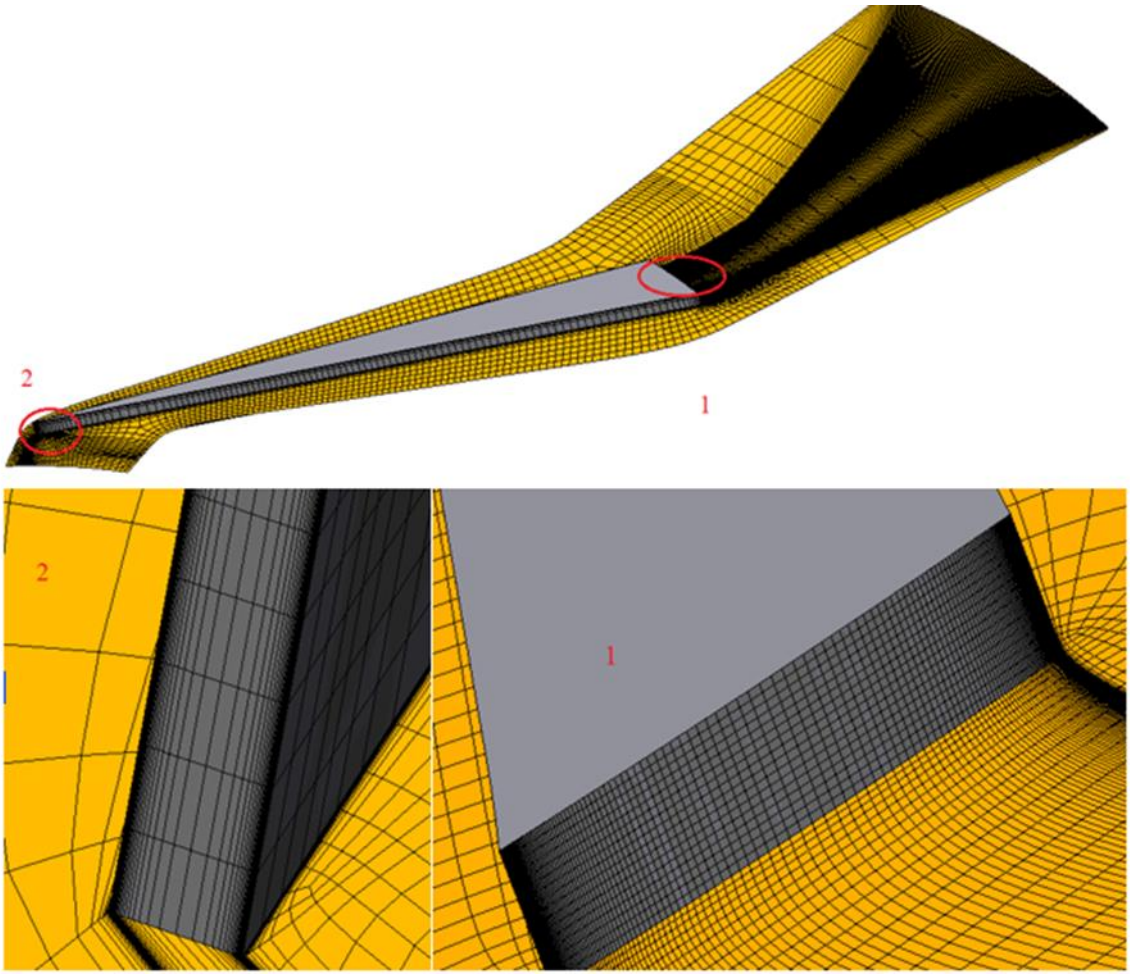

Figure 3-11 Diffuser passage grid.

b) Machine data

"Machine Data" encompasses parameters and settings that define a machine's characteristics and performance, including dimensions, material properties, boundary conditions, and operational parameters. This data is essential for accurate simulations and reliable results.

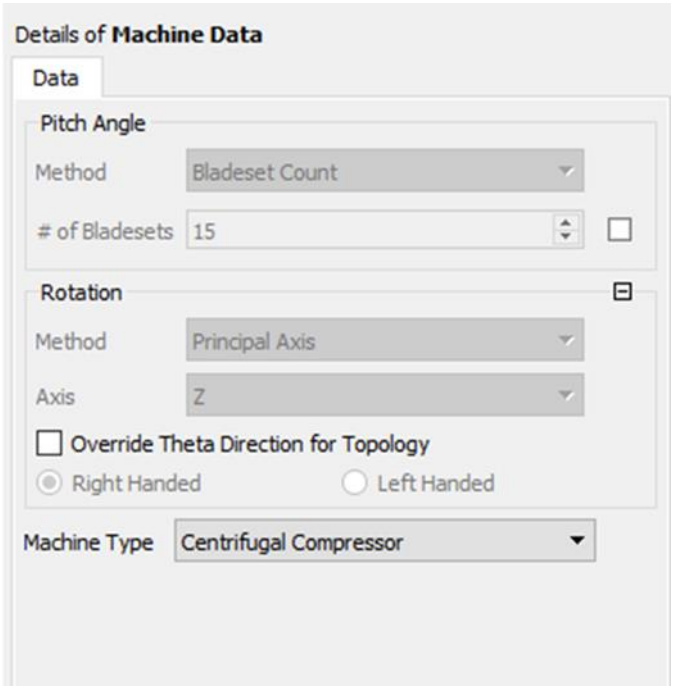

Figure 3-12 Machine data.

c) Mesh topology

different mesh topologies H, J, C, L, and O types are used for creating meshes around blades and walls. Each topology is suited to specific geometric features, ensuring that the computational mesh can accurately represent the flow domain and capture important details of the fluid dynamics around the blade.

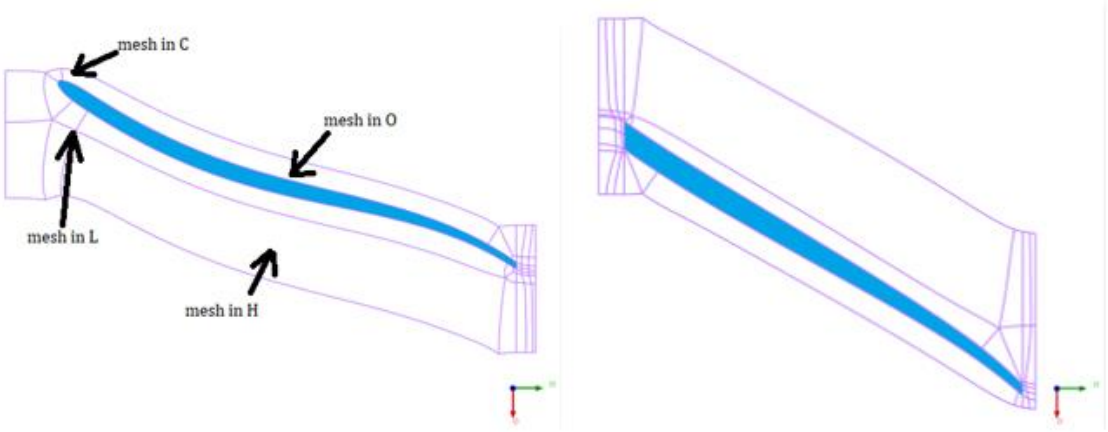

Figure 3-13 Mesh topology.

d) Mesh Data

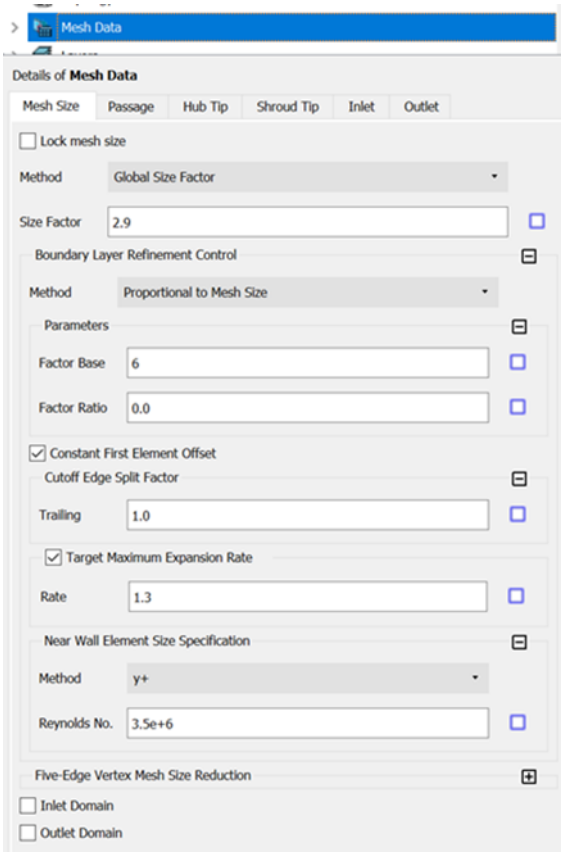

Figure 3-14 Mesh Data “Mesh size”.

The Mesh Data object includes configurations that influence the entire mesh. Blade-specific mesh data objects have a portion of these configurations and impact the mesh for each blade within the blade set individually. Meanwhile, complex blade end mesh data objects affect the mesh for each complex blade end individually.

Global Size Factor: The Global Size Factor method defines the overall mesh size. To increase the resolution of the mesh, increase the size factor using the Size Factor setting. Note that the change in overall mesh size is not linear. In this mode, if you change the spanwise mesh size or the boundary layer refinement, or make any local edge refinements to the mesh, the Global Size Factor will stay fixed and the overall mesh size may change. This factor,

when used with proportional refinement, can be used to scale the mesh size for a mesh refinement study.[18]

Boundary Layer Refinement Control

In the Boundary Layer Refinement Control settings, the boundary layer region is defined by the topology blocks along the edges of the blade.

- **Proportional to Mesh Size :** This option controls the number of elements across the boundary layer region in proportion to the values specified for Factor Base and Factor Ratio. This method maintains similar expansion rates when the Global Size Factor is changed. If the blade has a cut-off edge, Factor Ratio also controls the number of elements along the cut-off edge.[18]

Constant First Element Offset: When Constant First Element Offset is selected, TurboGrid applies a double-sided node distribution, which means the expansion rate is not constant for the boundary layer. In this scenario, the near-wall expansion rates provided in the Boundary Layer Control object represent the approximate minimum and maximum values derived from a sample of the layer values.

Cutoff Edge Split Factor: The Cutoff Edge Split Factor setting is available only when Constant First Element Offset is selected. In cases where the leading edge and/or trailing edge is cut-off, you can specify a factor for each cut-off edge to control the number of elements along that edge (as viewed in any given layer). [18]

Target Maximum Expansion Rate: The Target Maximum Expansion Rate setting is available only when Constant First Element Offset is selected. Selecting Target Maximum Expansion Rate enables the specification of a target maximum expansion rate. TurboGrid attempts to prevent the expansion rate (at any place around the blade profile) from exceeding the specified maximum in different ways. [18]

Near Wall Element Size Specification: The Near Wall Element Size Specification setting determines how the near-wall node spacing is defined on the Passage and Hub/Shroud Tip tabs. This spacing refers to the distance between a wall (such as a hub, shroud, or blade) and the first layer of nodes adjacent to the wall. The Method options for calculating are:

- **Absolute:** The Absolute method enables you to directly set the near wall spacing. This specification, found on the Passage or Hub/Shroud Tip tab, requires a dimensional value expressed in units of distance.

- **Y Plus:** The y^+method allows you to set the near wall spacing, Δy, in accordance with a target value of y^+. The target value of y^+ may then be specified on the Passage and Hub/Shroud Tip tabs, as applicable (that is, when a near wall size is required by the specified distribution method).The following formula relates the near wall spacing to y^+:

$$\Delta y = L\Delta y^{+}\sqrt{80}Re_{x}^{\frac{1}{14}}\frac{1}{Re_{L}} \qquad 3\text{-}1$$

where L is the blade chord, Δy^{+} is the specified target Re_x value, y^{+} is the Reynolds number based on the distance along the chord (measured from the leading edge), and Re_L is the Reynolds number based on chord length. Ansys TurboGrid approximates L as the algebraic average of the chord lengths of each blade profile in the blade file. You must specify Re_L . Ansys TurboGrid approximates Re_x as being equal to the specified value of Re_L. [18]

Five-Edge Vertex Mesh Size Reduction: An ATM-based mesh may contain one or more vertices that each join exactly five edges. At these locations, the mesh generation process will tend to pull the mesh away from the five-edge vertex to make the surrounding element edges more orthogonal, resulting in relatively larger elements surrounding the vertex than the rest of the mesh in their vicinity. The Five-Edge Vertex Mesh Size Reduction > Factor setting, when set to a value less than 1.0, will reduce this tendency, trading off between mesh orthogonality for sizing. [18]

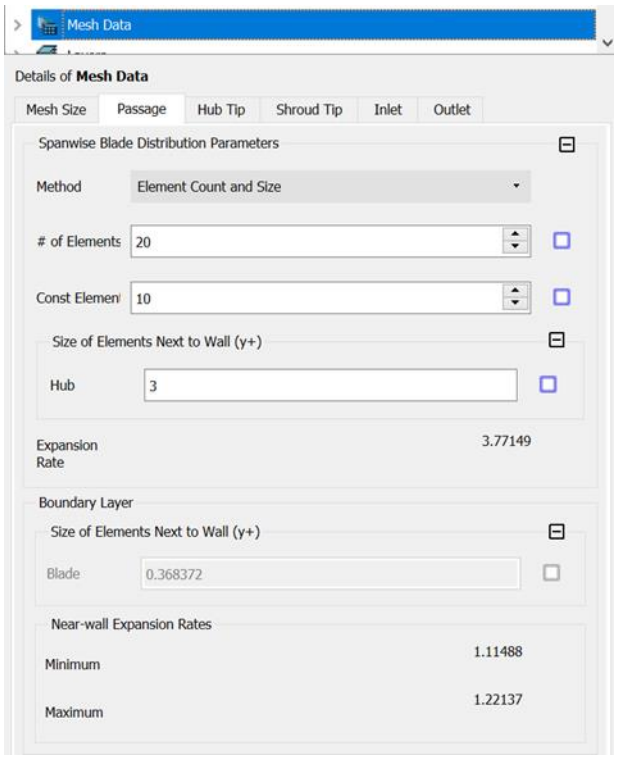

Figure 3-15 Mesh Data “Passage”.

In ANSYS TurboGrid, the Passage Tab is used to configure mesh settings for blade passages. This tab allows users to control node distribution along the blade span and optimize mesh quality for accurate simulation results of rotating machinery.

the "Spanwise Blade Distribution Parameters" manage the distribution of mesh elements along the blade's span (from hub to shroud). This setting is vital for accurately capturing the blade geometry and flow characteristics. Different methods, such as Constant, Proportional, and Custom, allow users to control the mesh density and distribution to balance accuracy and computational efficiency.

e) Mesh statistics

Mesh quality refers to how well the finite element mesh represents the model geometry and balances element size and number. A high-quality mesh has elements with good shape, size, aspect ratio, skewness, and smoothness. Elements should ideally be regular shapes, with similar sizes and aspect ratios, low skewness, and smooth transitions. ANSYS provides tools to assess and improve mesh quality, ensuring accurate and reliable simulation results.

Mesh quality recommendations :

- Low orthogonal quality or high skewness values are not recommended.
- Generally try to keep minimum orthogonal quality > 0.1, or maximum skewness <0.95 However these values may be different depending on the physics and the location of the cell.
- Fluent reports negative cell volumes if the mesh contains degenerate cells.

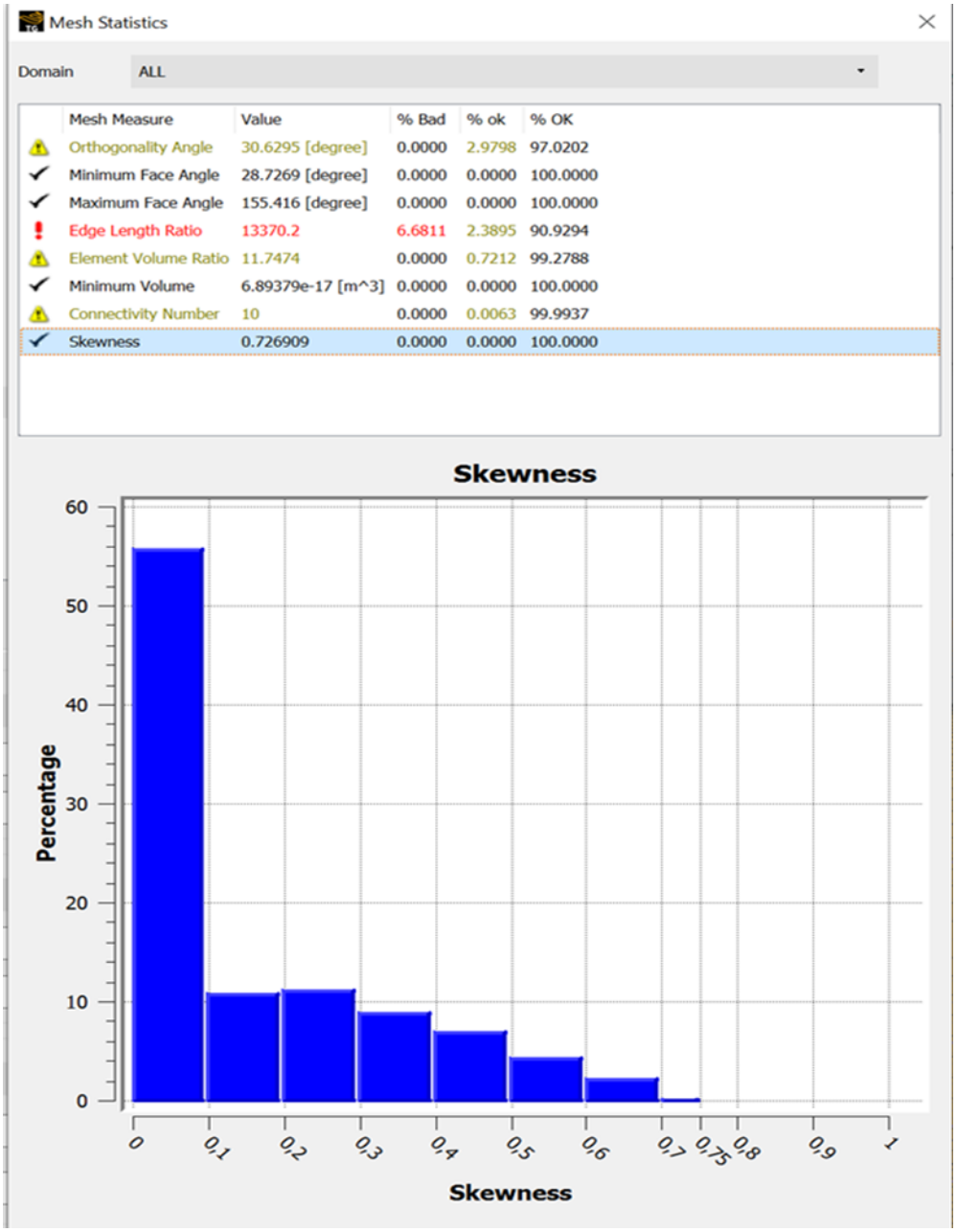

Figure 3-16 Mesh statistics.

Two methods for determining skewness:

1) Equilateral volume deviation:

$$Skewness = \frac{optimalcellsize - cellsize}{optimalcellsize} \quad 3\text{-}2$$

Applies only for triangles and tetrahedrons

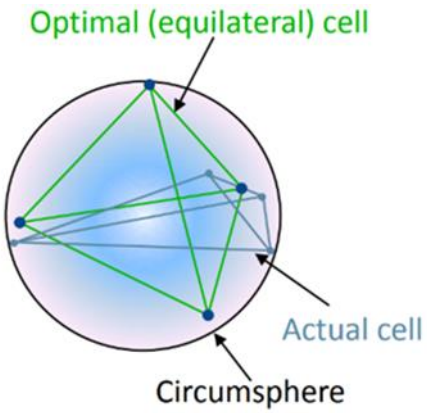

2) Normalized angle deviation:

$$Skewness = max[\frac{\theta_{mzx} - \theta_c}{180 - \theta_c}, \frac{\theta_c - \theta_{min}}{\theta_c}]3\text{-}1 \quad 3\text{-}3$$

Where $\theta_c$is the equiangular face/cell (60 for tets and tris, and 90 for quads and hexas)

- Applies to all cell and face shapes .
- Used for hexa, prisms and pyramids.

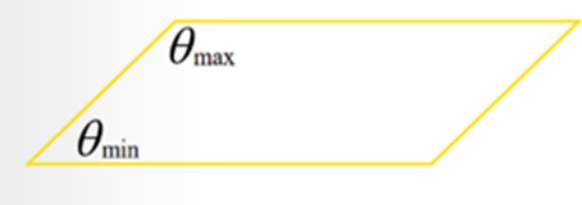

Skewness mesh metrics spectrum

Excellent	Very good	Good	Acceptable	Bad	Unacceptable
0-0.25	0.25-0.50	0.50-0.80	0.80-0.94	0.95-0.97	0.98-1.00

The mesh for a turbomachine depends on the following conditions:

1- Maximum face angle: this is the largest angle of all the faces touching the node, and measures the distortion. The value of this angle is 165˚.

2- Minimum face angle: this is the smallest angle between two edges touching the node, the value of this angle is 15˚.

3- Connectivity number: this is the number of elements connected to a node, with a maximum value of 12 and a minimum value of 0.

4- Volume element ratio: this is the ratio of the large volume to the small volume associated with a node; this ratio is positive.

5- Edge length ratio: this is the ratio of the distance between the longest edge and the shortest edge on the same face, with a maximum value of 10.

6- Minimum volume: this is the positive volume of the mesh to ensure that no negative volume exists in the passage of the fluid.

3.4.3 Performing calculations:

Once the stator and rotor meshes are created using TURBOGRID, the simulation process begins with ANSYS CFX to analyze the fluid dynamics within the compressor stage. This simulation allows for a detailed flow analysis of the compressible fluid through the blade geometry. Besides using the mesh generated by TURBOGRID, we will also define the boundary conditions. ANSYS CFX will then perform the calculations and present the results.

The simulation in CFX involves three main components:

- **Setup:** Configuration of the simulation parameters and boundary conditions.
- **Solution:** Execution of the computational fluid dynamics (CFD) calculations.
- **Results:** Visualization and analysis of the simulation outcomes.

a) Setup

The simulation begins by selecting the TURBO mode in the configuration, which is specifically designed for setting up turbomachinery simulations. The mesh for each component of the stator and rotor is imported from TurboGrid. Basic parameters and boundary conditions are then identified and set.

In CFX-Setup, the model of the stage interface allows for the repetition of the flow field in multiple regions with identical rotation. As a result, only one region needs to be solved, and the boundaries are set as periodic.

Consequently, the simulation involves only a single stator blade and a single rotor blade. This method is efficient and significantly reduces the computational effort required.

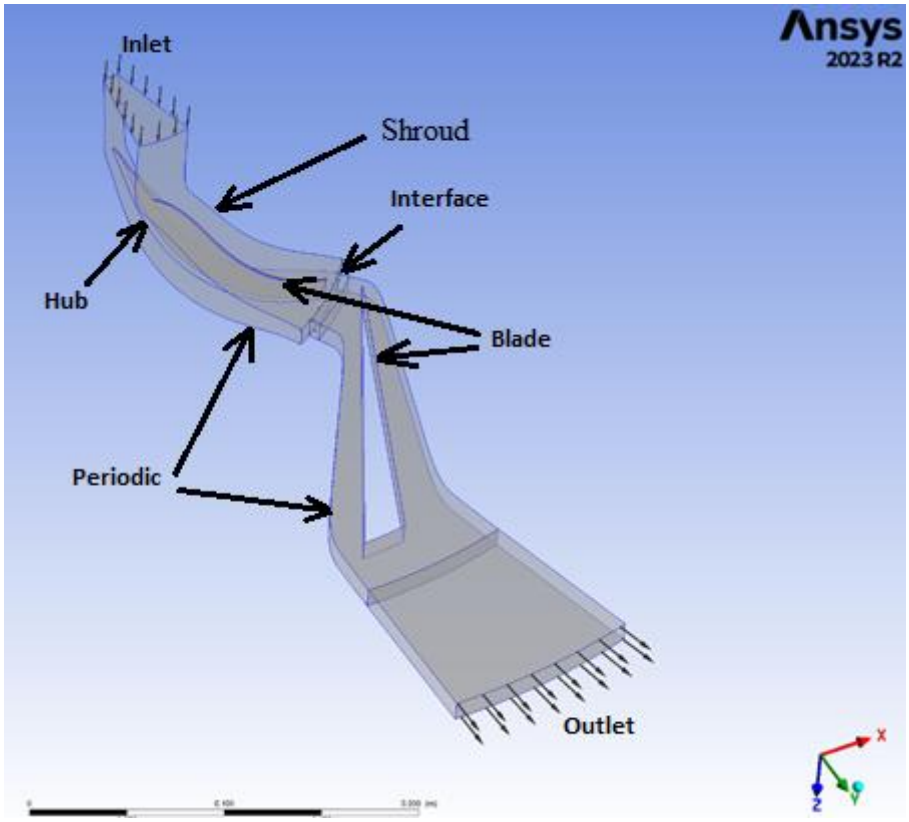

Figure 3-17 Computational domain of simulation

Starting the turbo mode:

a. basic parameters:

- specification of the type of machine as a radial compressor.
- The type of analysis: steady state (in RANS simulation case).
- The type of analysis: transient (in URANS and LES simulation case).

The time dependence of the flow characteristics can be specified as steady state or transient, the steady state simulation, by definition, considers the flow characteristics do not change with time, it requires no real time information to describe it and vice versa.

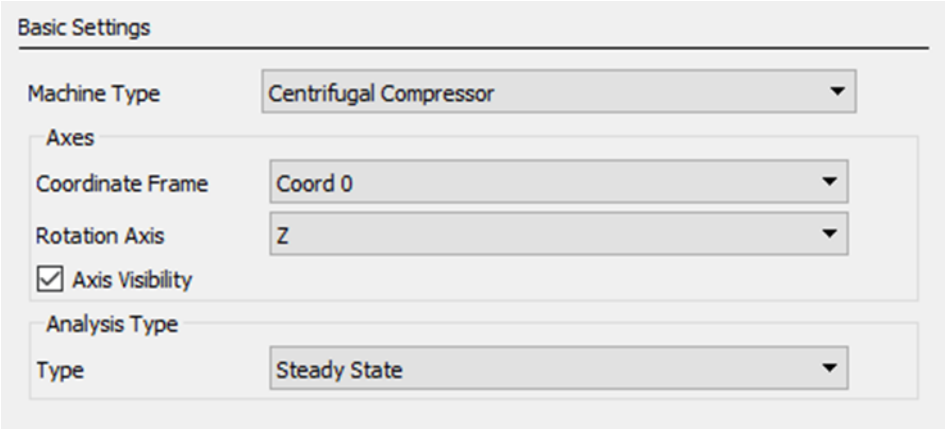

Figure 3-18 Basic settings "unsteady simulation".

Plus in the transient case we need to specify the time needed (total time and time steps) for our simulation.

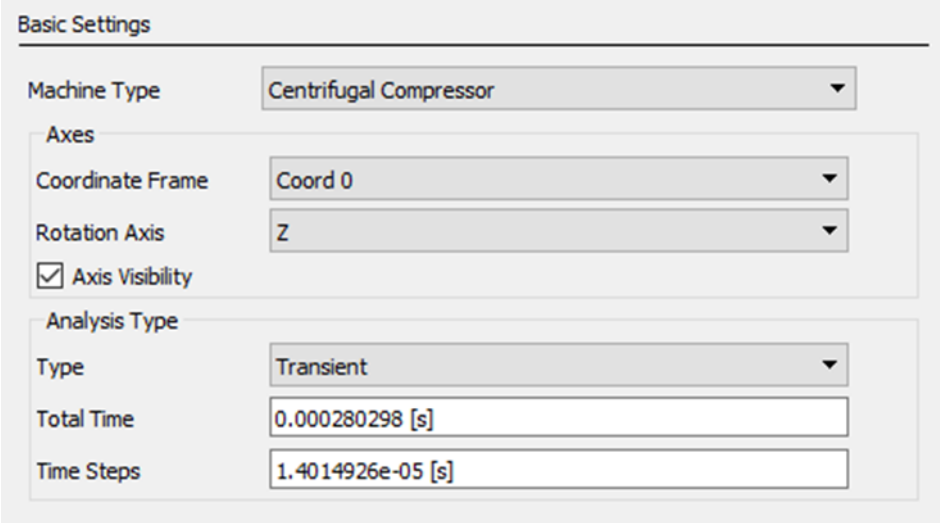

Figure 3-19 Basic settings "unsteady simulation".

b. creation of a system composed of stator and rotor:

- the first component 'stator' is specified with a stationary status.
- the second component 'the rotor' is added with a rotating status.

- the rotation speed is 28541 [RPM].

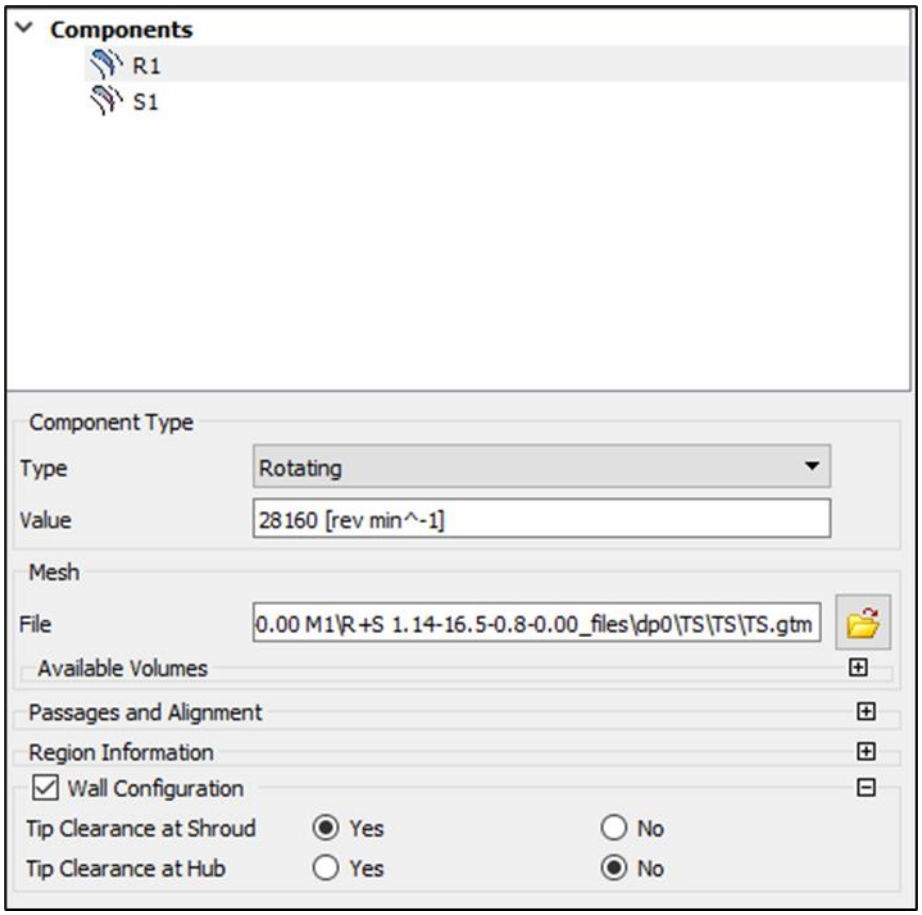

Figure 3-20 The creation of a system composed of stator and rotor.

c. Physical definition:

Fluid flow equations can be closed (numerically) by specifying conditions on the outer boundaries of the calculation domain.

All possible variables at the location of the study must be specified in order to place restrictions on the mathematical formulation that allow for a unique resulting solution. The specified boundary conditions should be sufficient to ensure a unique solution. To carry out our simulation, the boundary conditions are fixed by :

- total pressure in Intel .
- mass flow rate in outlet.

heat transfer is not included in the analysis. The turbulence selected as SST for RANS, URANS and in LES turbulence is selected as LES WALE.

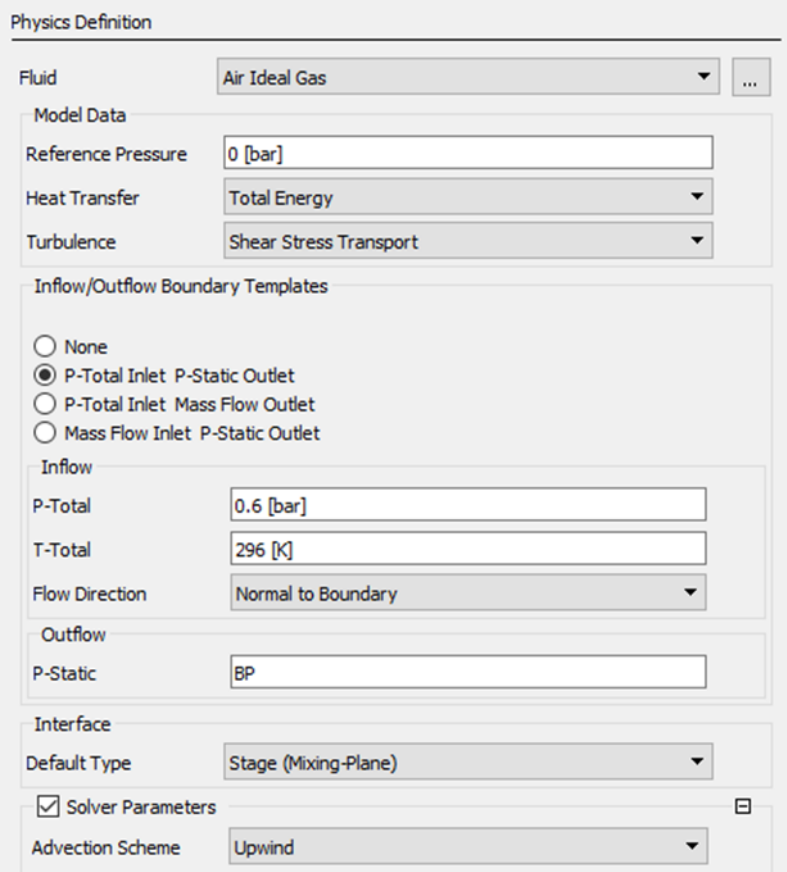

Figure 3-21 Physics Definition.

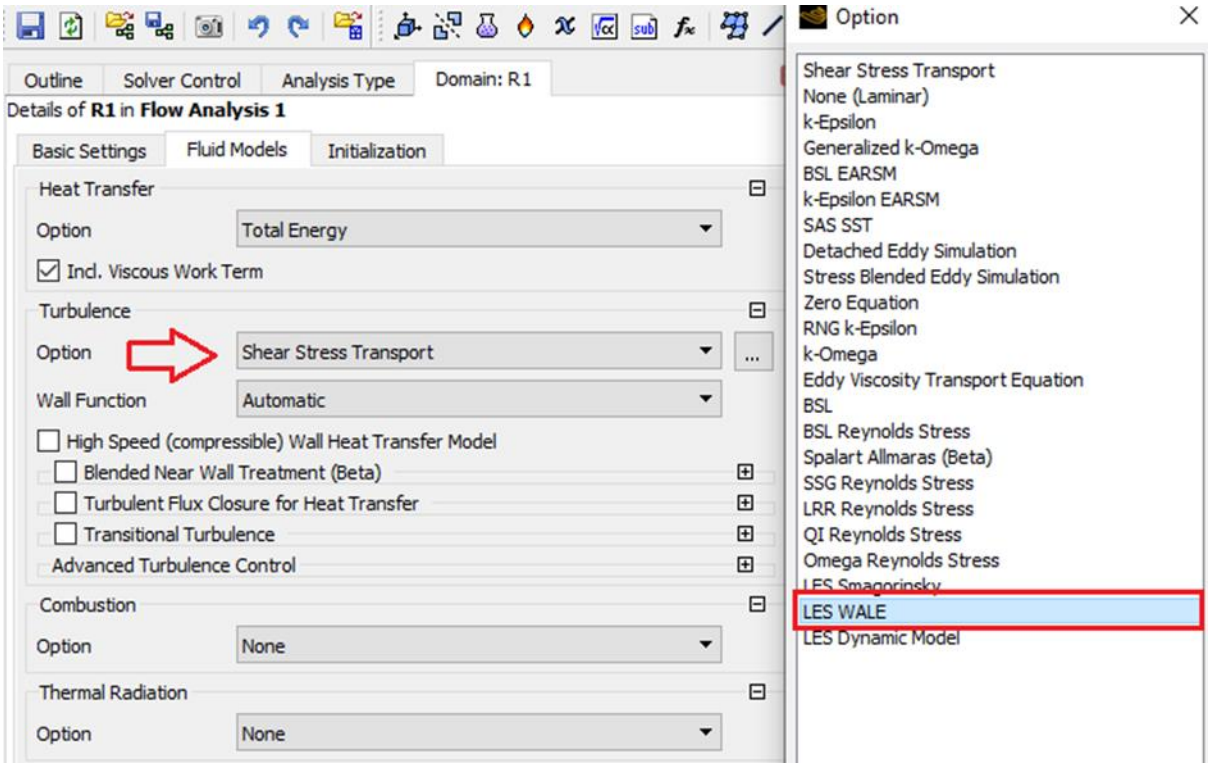

Figure 3-22 Fluid models.

b) Solver Control:

In this part we have limited the number of iterations to 600 maximum and error 10e-5 in order to achieve a good results.

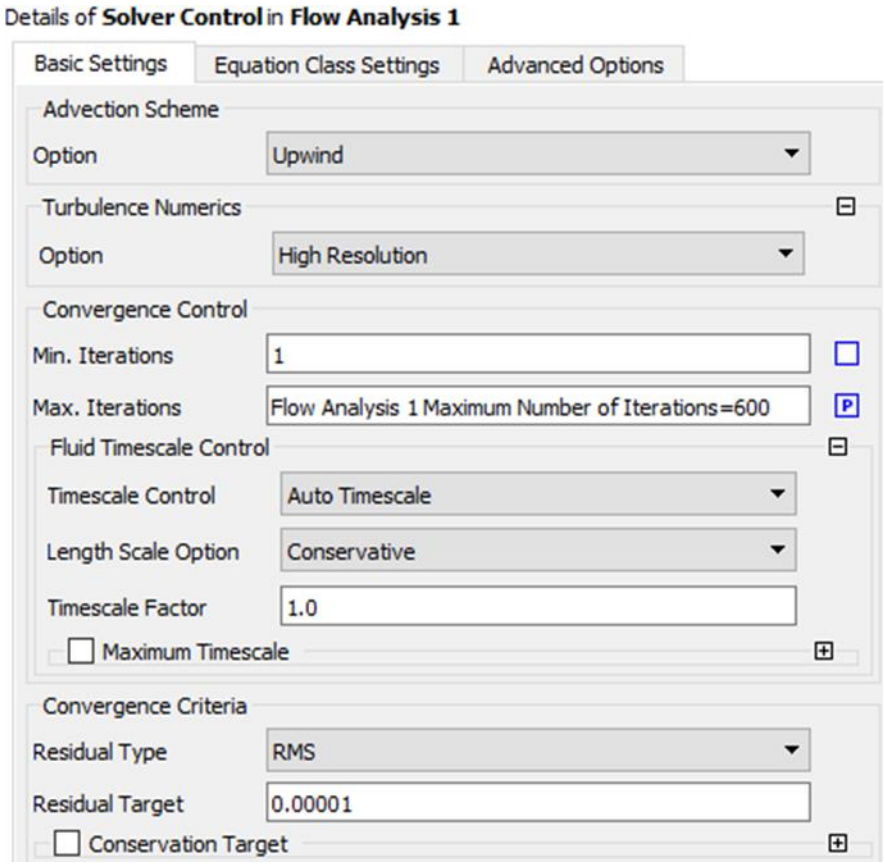

Figure 3-23 Solver Control "steady simulation".

The main differences between the iteration between the steady-state (RANS) and the transient (URANS and LES) are:

- **Min. Coeff. Loops:** This option determines the minimum number of iterations per timestep, and has a default value of 1.
- **Max. Coeff. Loops:** This option determines the maximum number of iterations per timestep, and has a default value of 10.

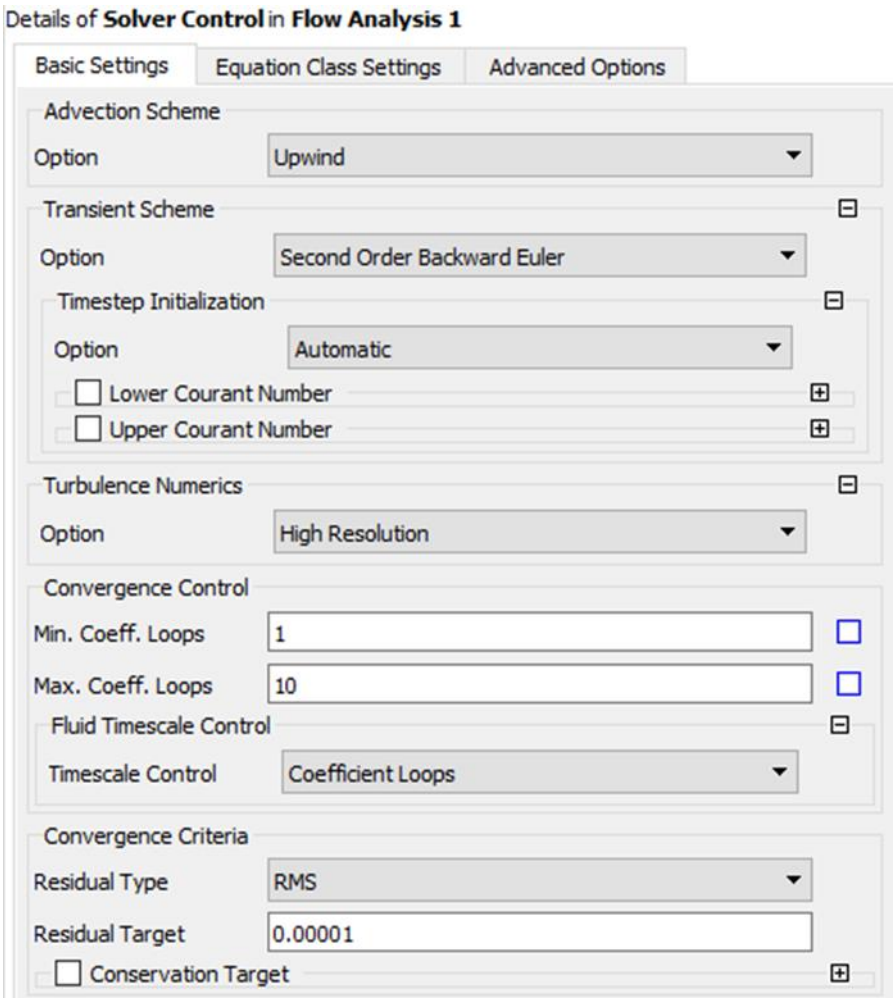

Figure 3-24 Solver Control "unsteady simulation".

3. 5 Boundary conditions for the impeller-diffuser

Table 2 The calculation limit conditions

Characteristics	**ANSYS CFX . 23**
Simulation Domain	An inter-blading channel (periodicity condition)
Simulation regime	Steady (RANS) Unsteady (URANS and LES)
Mesh	Structure
Fluid	Ideal gas (Compressible air)

Boundary condition at the entrance	Total pressure [Pa]
Boundary condition at the exit	Variable mass flow rate [kg/s]
Turbulence module	SST, LES WALE
numerical scheme	Second order (High Resolution)
Average residue	10^{-4}

Chapter 4 Results And Discussion

4. 1 Introduction

In this chapter, we will discuss the results of our simulations for the compressor stage with different models to observe the specification of each model and how it affects the aerothermodynamics parameters and the flow structure.

We will begin with the mesh sensitivity study evaluating the error between our simulations and the experimental data and confirming that our results are mesh-independent

4. 2 Mesh sensitivity and results validation

In CFD simulations the fluid domain is discretized into a mesh where quantities will be calculated on the center of elements, edges, or nodes depending on the solution scheme.

The finer the mesh the more precise the results are until a certain mesh density is reached from which a finer mesh won't have an impact on the precision of the solution, in this case, we can say that our solution is mesh-independent.

The impeller and diffuser fluid domains have been meshed separately and the two domains will be joined in ansys CFX.

First set of simulations was conducted with a mesh with a total element count of approximately 900,000 elements, the size was increased to reach approximately 2,480,000 elements in total, and then it was increased again to 5,000,000 elements in total. In the last mesh, the difference is that we've chosen a single point of the pressure ratio/ mass flow we will perform this number of mesh which is necessary in the unsteady simulation.

Below is a graphical representation of the performance map of our compressor obtained from the three meshes and the experimental data.

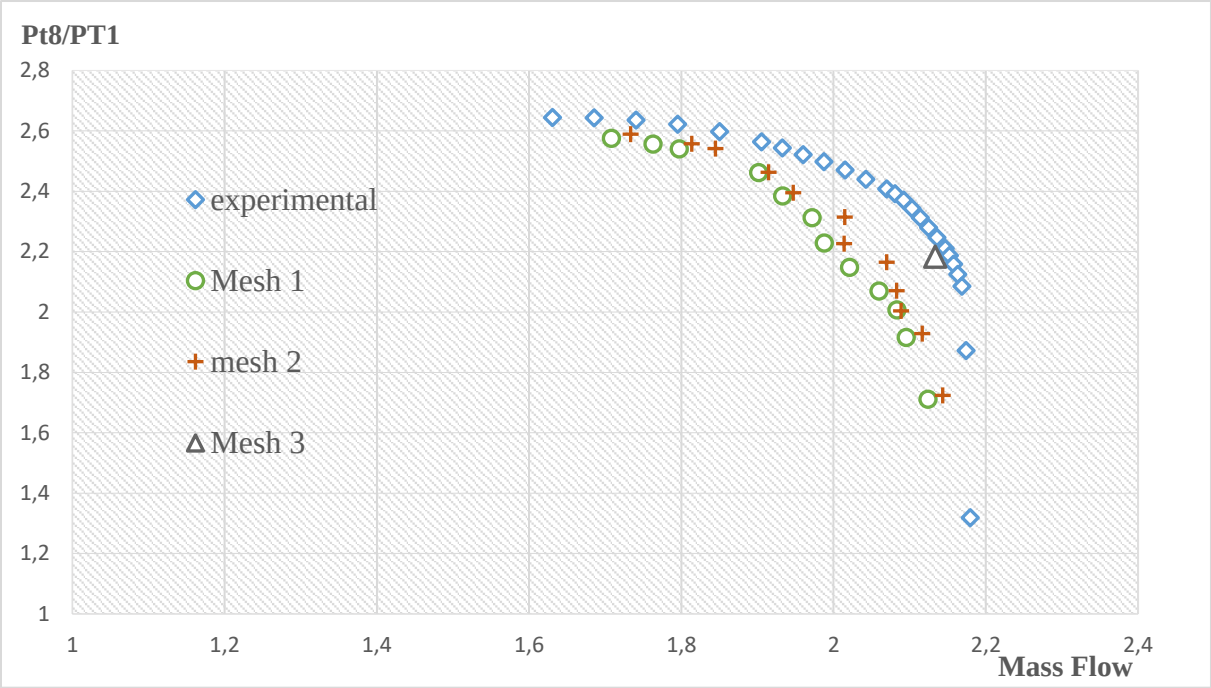

Figure 4-1 Mesh sensitivity.

Table 3 Calculation results.

Numerical calculation	**Number of elements**	**Pressure ratio(EXP)**	**Pressure ratio(CFX)**	**%Relative error**
Mesh 1	879172	2,1879	2,14877	1,7926
Mesh 2	2479437	2,1879	2,16541	1,0321
Mesh 3	5181568	2,1879	2,1831	0,2236

4. 3 Y^+ validation

In this study, the near-wall resolution was carefully validated to ensure y^+ values were predominantly below 5 for all simulations, utilizing the $k-\omega-SST$ turbulence model for RANS and URANS, and the WALE model for LES. While the optimal y^+ range for these models ideally targets values below 1, achieving y^+ values under 5 is still highly valuable. This ensures that the boundary layer, including the viscous sub-layer, buffer layer, and the fully turbulent region, is well-resolved. Such resolution is crucial for accurately capturing shear stresses, pressure gradients, and thermal characteristics. For the k-omega SST model, y^+ values below 5 help maintain the robustness and accuracy in predicting flow separation

and adverse pressure gradients. Similarly, for the LES WALE model, these y^+ values enable the capture of detailed turbulent structures and near-wall eddies, ensuring a detailed representation of entropy and flow dynamics. The validation confirms that the chosen mesh refinement adequately supports the high-fidelity requirements of the turbulence models, contributing to reliable and accurate simulation results for the centrifugal compressor performance analysis.

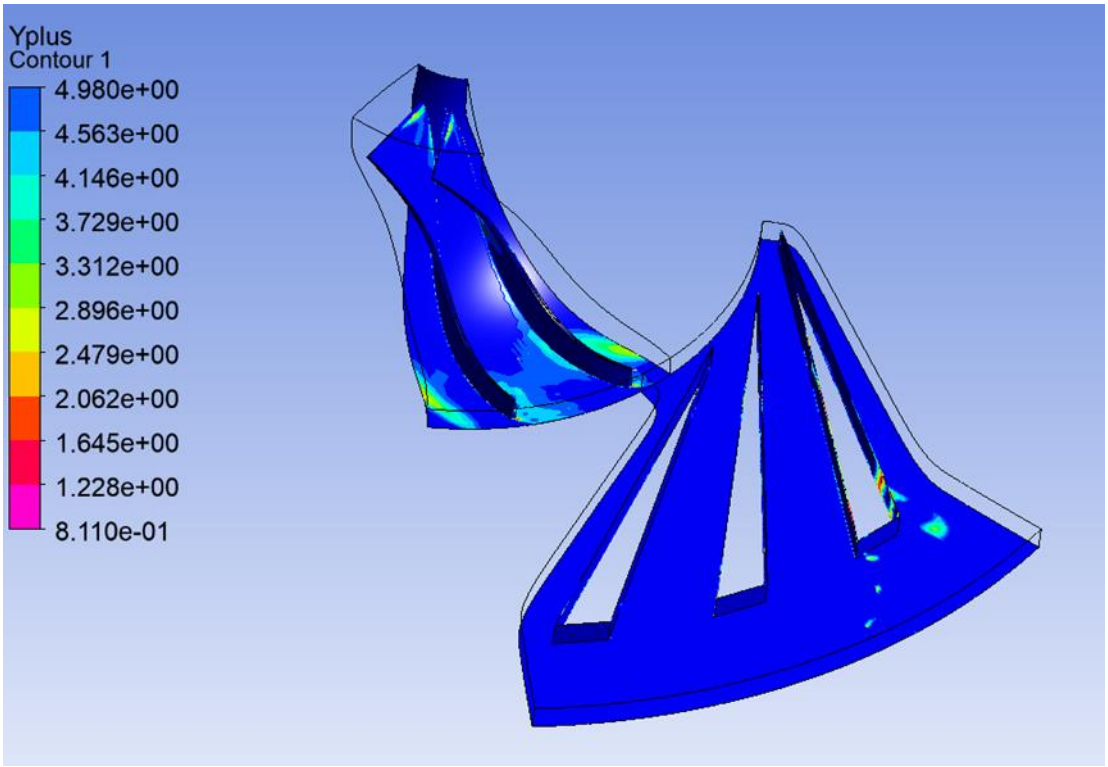

Figure 4-2 Y^+ comtour.

4. 4 Simulation results and discussion

In this section, we present and analyze the results of the centrifugal compressor simulations conducted using three different turbulence models: Reynolds-Averaged Navier-Stokes (RANS), Unsteady Reynolds-Averaged Navier-Stokes (URANS), and Large Eddy Simulation (LES). Each model offers a distinct approach to capturing the turbulent flow phenomena within the compressor, and comparing these models provides insights into their respective strengths and limitations.

The analysis is performed across three critical planes within the compressor to comprehensively evaluate the flow characteristics:

- Meridional Projection
- Blade-to-Blade Plane
- Orthogonal Cut

Through these planes, we compare key flow parameters such as Mach number, pressure distributions, temperature and entropy.

4.4.1 Blade-To-Blade Projection Plane Analysis

4.4.1.1 Relative Static Pressure Analysis

RANS Model

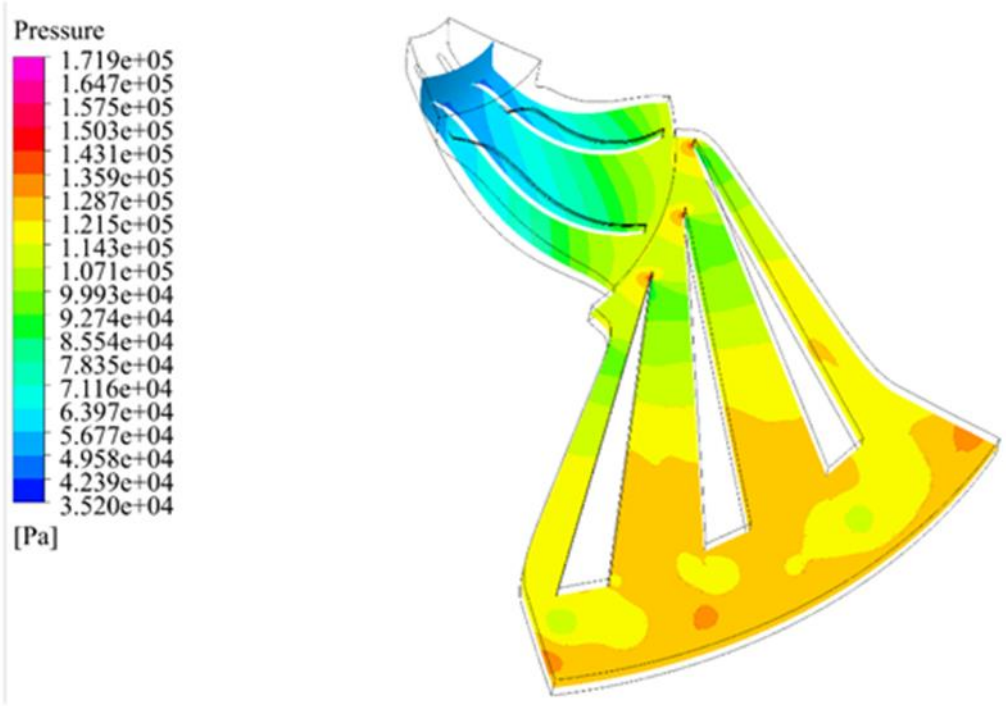

Figure 4-3 Relative Static pressure distribution in the blade-to-blade plane (RANS).

- **Description:**

  The static pressure distribution in the RANS model shows a gradient from high pressure (red) near the outlet to lower pressure (blue) near the inlet.

- **Observations:**
    - The high-pressure region is concentrated towards the outer radius of the compressor.
    - The low-pressure region is visible near the inlet and along the hub and shroud surfaces.
    - The pressure gradient appears relatively smooth, indicating a steady-state flow assumption.

URANS Model

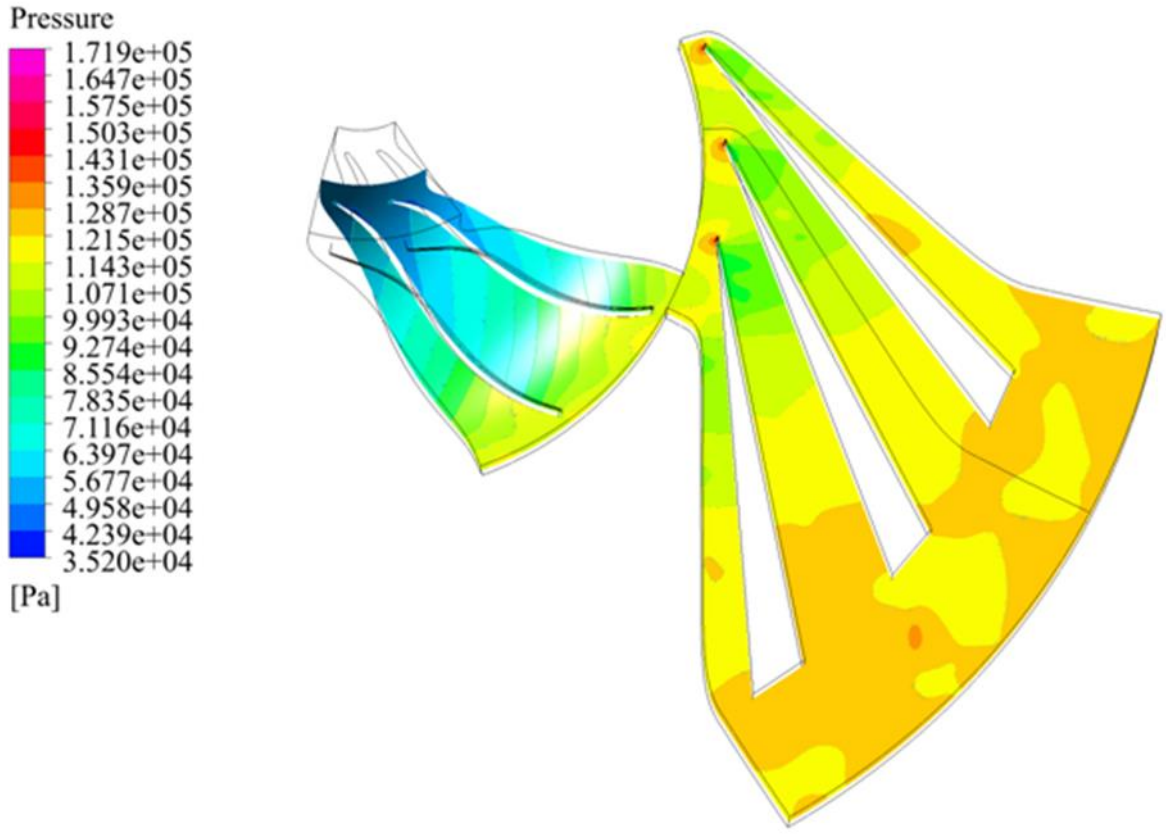

Figure 4-4 Relative Static pressure distribution in the blade-to-blade plane (URANS).

- **Description:**

The static pressure distribution in the URANS model displays a similar overall pattern to the RANS model, but with more variation and detail.

- **Observations:**
  - There is a more pronounced variation in pressure distribution, especially near the outlet and along the blades.
  - The pressure contours indicate unsteady effects, with slight fluctuations compared to the RANS model.
  - The overall pressure gradient follows the same trend as RANS, but the details suggest more complex flow dynamics.

LES Model

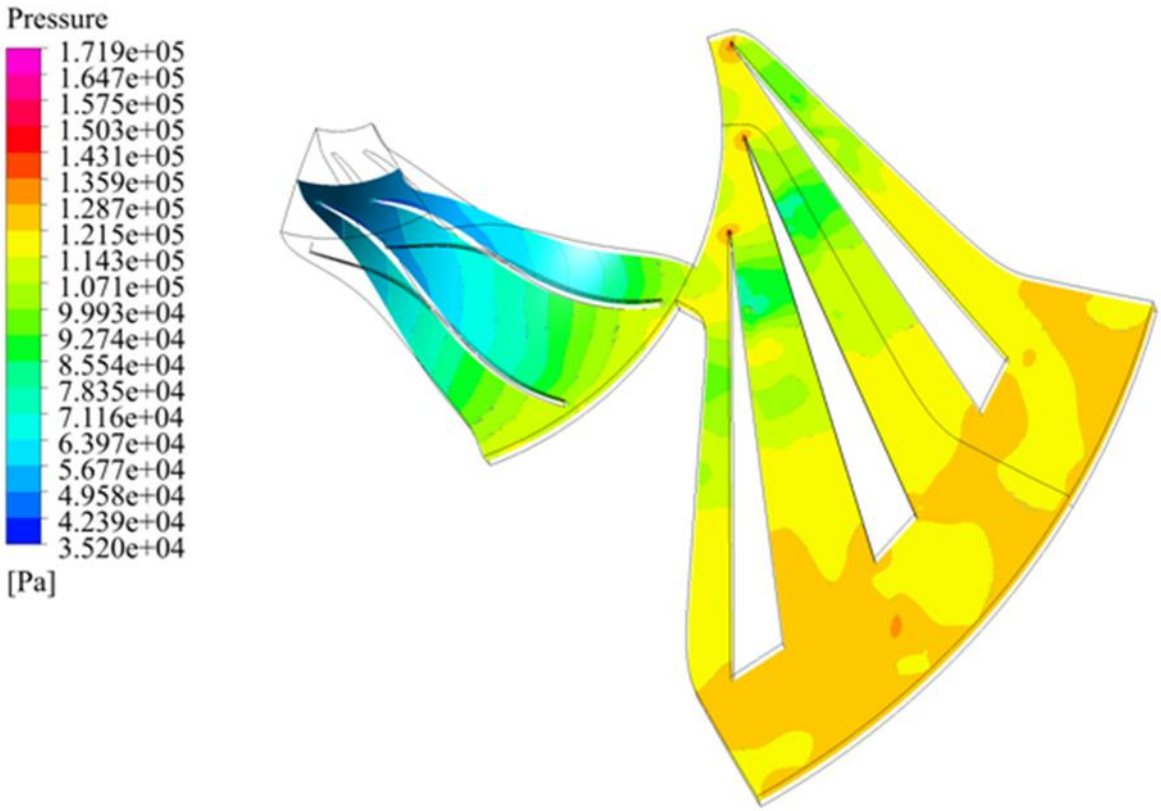

Figure 4-5 Relative Static pressure distribution in the blade-to-blade plane (LES).

- **Description:**

The static pressure distribution in the LES model shows the highest level of detail and complexity among the three models.

- **Observations:**
    - The pressure contours are more intricate, capturing small-scale structures and variations in the flow.
    - There are noticeable fluctuations and variations throughout the flow field, indicating the unsteady and turbulent nature of the flow.
    - The high-pressure regions are more localized and detailed, with clear distinctions between high and low-pressure zones.

Comparative Analysis:

- **Overall Trends**
    - All three models show a high-pressure region near the outlet and a low-pressure region near the inlet, following the expected behavior in a centrifugal compressor.
- **RANS vs. URANS**
    - The RANS model provides a smooth pressure gradient, suitable for steady-state analysis but lacks detailed flow structures.
    - The URANS model introduces unsteady effects, capturing more variations in the pressure field compared to RANS. This suggests better capturing of transient phenomena and flow instabilities.
- **URANS vs. LES**
    - The URANS model shows more detail than RANS but less than LES. It captures some unsteady effects but not the full complexity of the turbulent flow.
    - The LES model provides the highest level of detail, capturing small-scale turbulent structures and variations that RANS and URANS models miss. This makes LES the most accurate for resolving detailed flow features but also the most computationally expensive.

4.4.1.2 Analysis of Relative Total Pressure Distribution:

RANS Model:

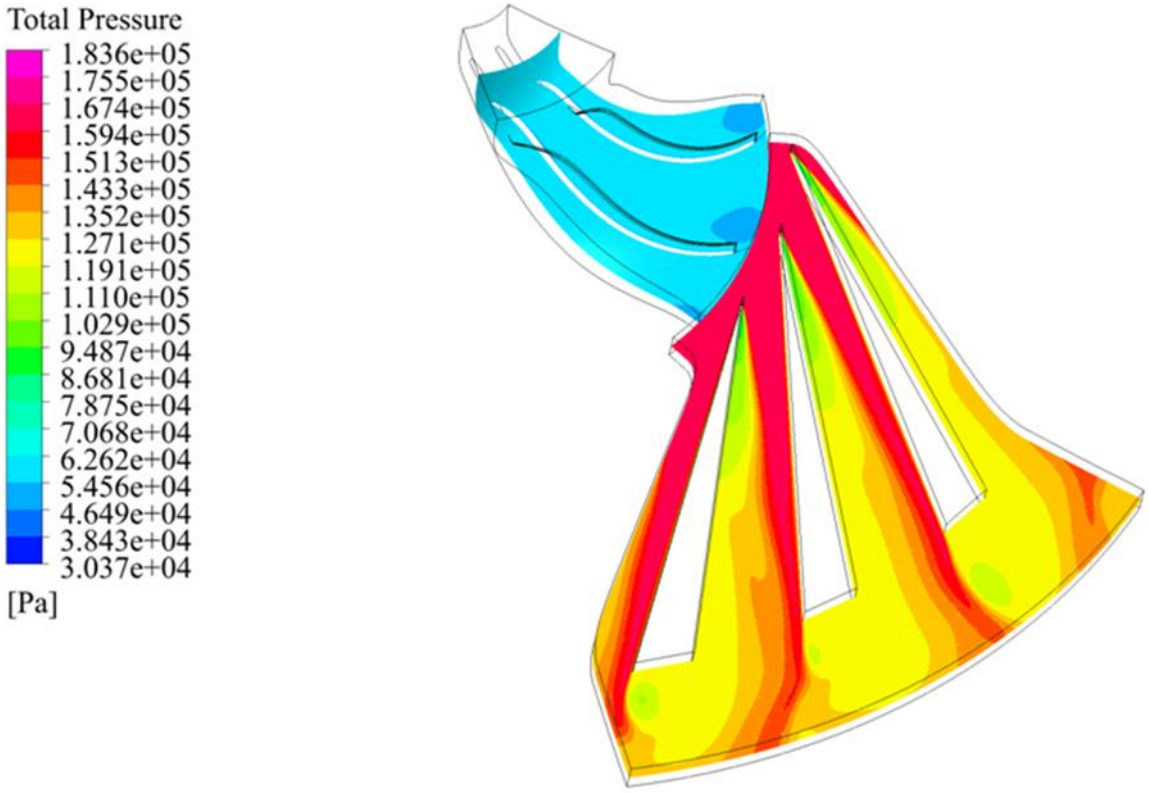

Figure 4-6 Relative Total pressure distribution in the blade-to-blade plane (RANS).

- **Description:**
  - The RANS model shows a distinct high-pressure region near the outlet of the compressor, indicated by the red and yellow areas.
  - The total pressure appears to decrease progressively as we move towards the inlet, transitioning from yellow to blue.
- **Observations:**
  - The pressure distribution is relatively smooth, indicating the averaged nature of the RANS model, which does not resolve turbulent fluctuations.
  - The high-pressure zones are concentrated near the blade regions, showing efficient compression but with limited detail in the turbulent structures.

URANS Model:

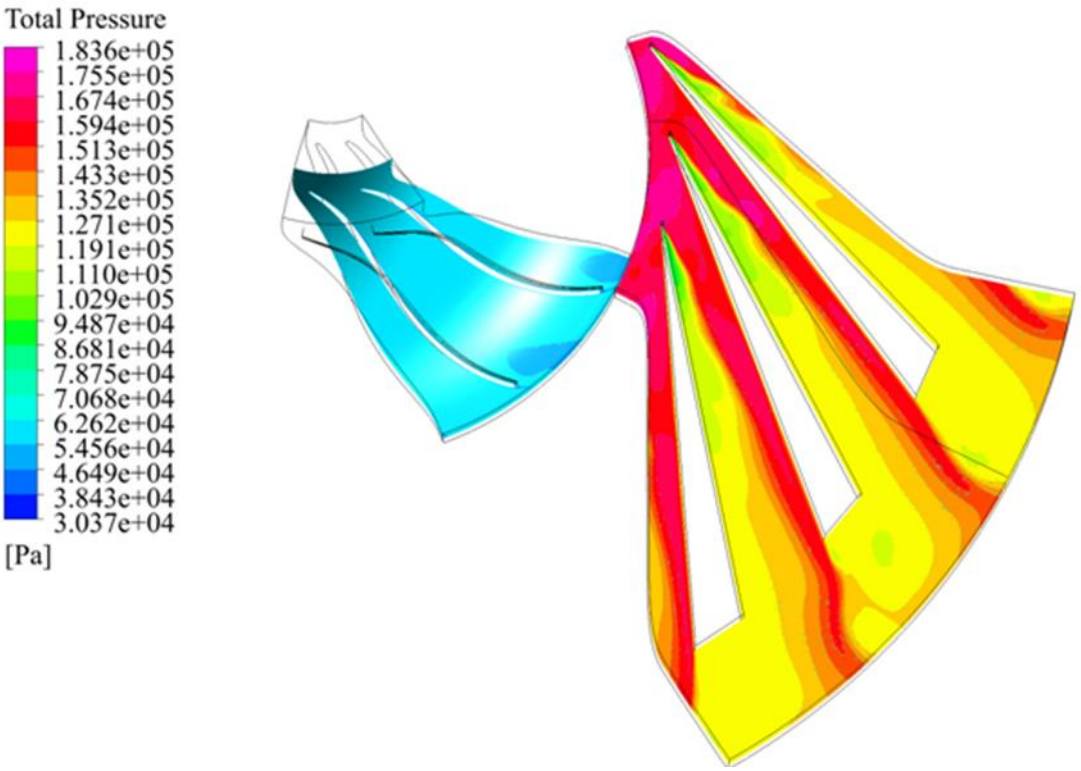

Figure 4-7 Relative Total pressure distribution in the blade-to-blade plane (URANS).

- **Description:**
    - Similar to RANS, the URANS model shows high-pressure regions near the outlet.
    - There are slight variations in pressure distribution near the blades compared to the RANS model, with a somewhat more detailed depiction of the pressure changes.
- **Observations:**
    - URANS captures some unsteady effects, leading to a slightly more complex pressure field.
    - There are subtle differences in the pressure contours, especially near the blade edges, indicating improved resolution of transient effects.

LES Model:

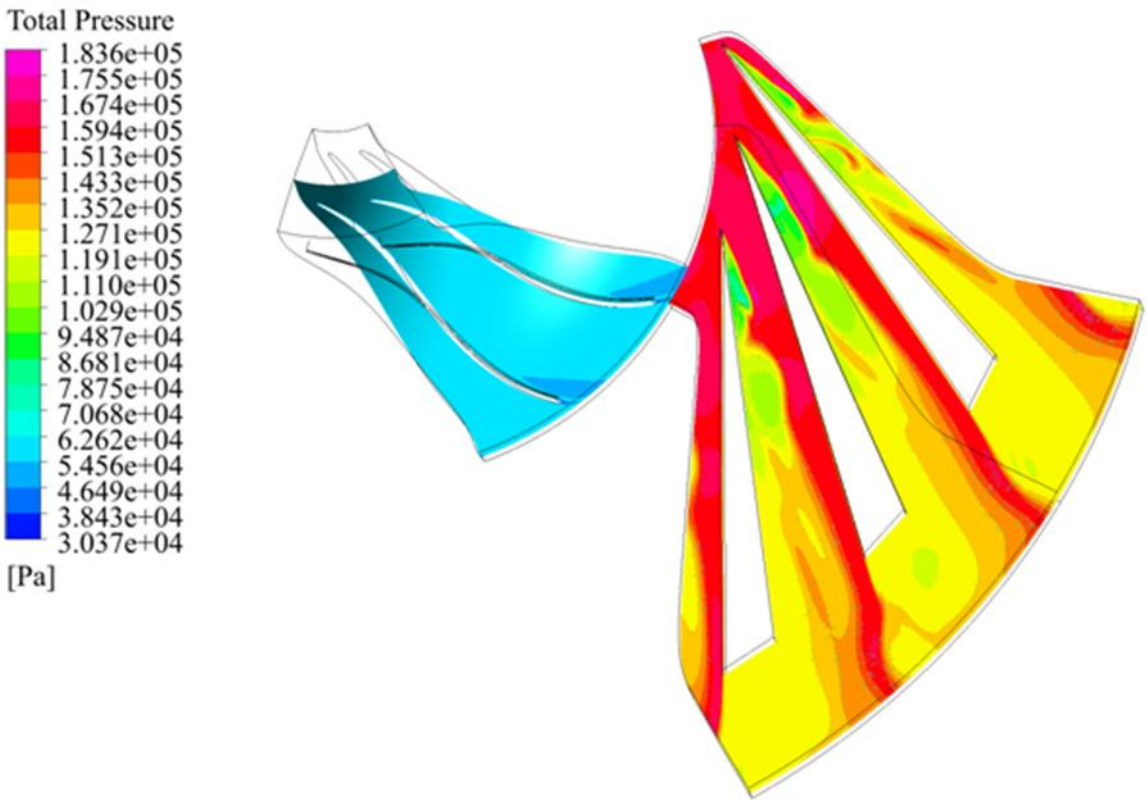

Figure 4-8 Relative Total pressure distribution in the blade-to-blade plane (LES).

- **Description:**
  - The LES model shows a much more detailed and varied pressure distribution compared to RANS and URANS.
  - High-pressure regions are still prominent near the outlet, but the pressure contours show finer details and more irregular patterns.
- **Observations:**
  - LES captures the turbulent structures more accurately, providing a highly detailed pressure distribution.
  - The pressure field is more intricate, with smaller-scale variations indicating the presence of resolved turbulent eddies.

Comparative Analysis:

- **High-Pressure Regions:**

  All three models show high-pressure regions near the outlet of the compressor. However, the RANS model shows a more smoothed-out pressure distribution, while LES provides a highly detailed depiction with more localized variations.

- **Transition and Gradients:**

  The RANS model provides the smoothest transition from high to low pressure, which is expected due to its averaging nature. URANS shows some improvement in capturing transient effects, resulting in a slightly more complex pressure field.

  LES, on the other hand, shows the highest level of detail, capturing the fine-scale turbulence and pressure gradients that are not visible in RANS or URANS.

- **Model Selection Impact:**

  - **RANS:** Best for a quick, averaged view of the pressure distribution. Suitable for initial design stages where computational resources are limited.
  - **URANS:** Offers a middle ground, capturing some transient effects and providing more detail than RANS. Useful when a balance between accuracy and computational cost is needed.
  - **LES:** Provides the most detailed and accurate pressure distribution, capturing fine-scale turbulence. Best for detailed studies and final validation stages but requires significant computational resources.

4.4.1.3 Relative Static Temperature Analysis

RANS Model

Figure 4-9 Relative Static temperature distribution in the blade-to-blade plane (RANS).

- **Description:**

  The static temperature distribution in the Meridional Projection plane using the RANS model shows a smooth and gradual temperature gradient. The temperature increases from the inlet to the outlet, with the highest temperatures observed near the outlet of the compressor.

- **Observations:**

  - The temperature distribution is relatively uniform, indicating minimal turbulent mixing.
  - The highest temperatures are concentrated near the outer periphery towards the outlet.

- The core region shows a steady increase in temperature without significant variations.

URANS Model

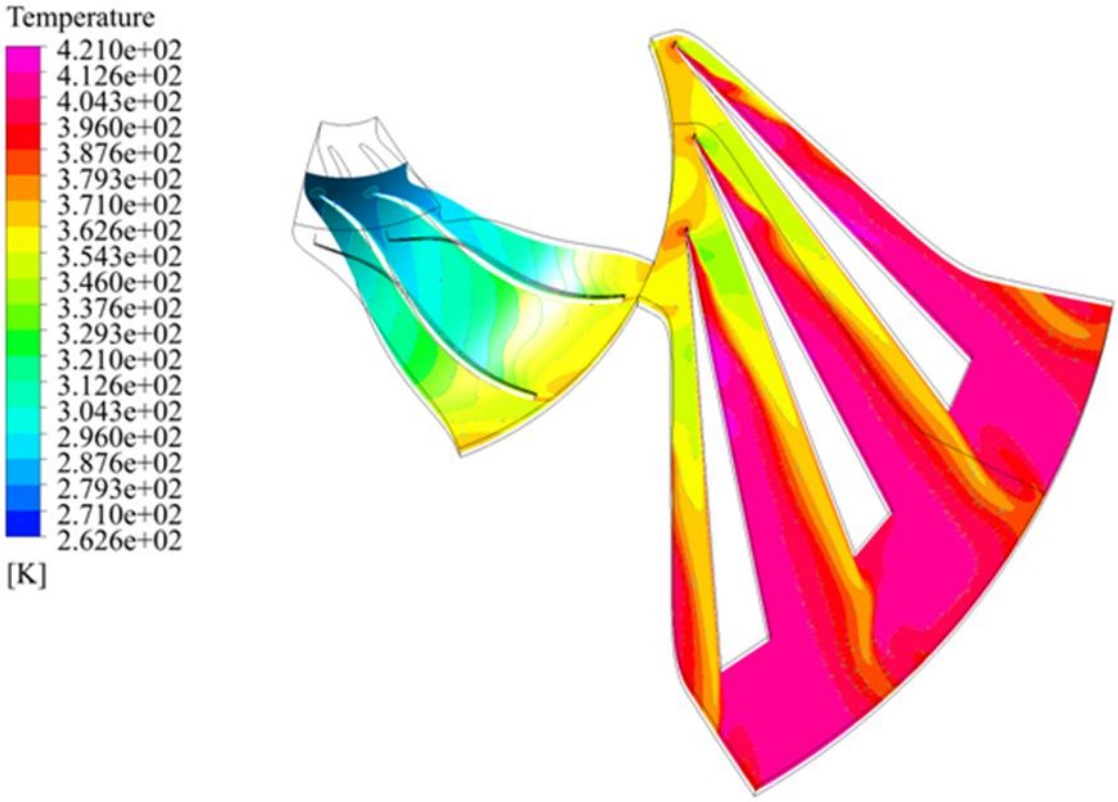

Figure 4-10 Relative Static temperature distribution in the blade-to-blade plane (URANS).

- **Description:**

  The static temperature distribution using the URANS model also shows an overall increase in temperature from the inlet to the outlet. However, there are noticeable transient effects that introduce minor temperature fluctuations throughout the flow field.

- **Observations:**

  - Temperature distribution shows more variations compared to RANS, reflecting transient phenomena.

- The highest temperatures are still concentrated near the outlet but with more evident fluctuations.
- Some regions show localized temperature peaks, suggesting intermittent turbulent mixing.

LES Model

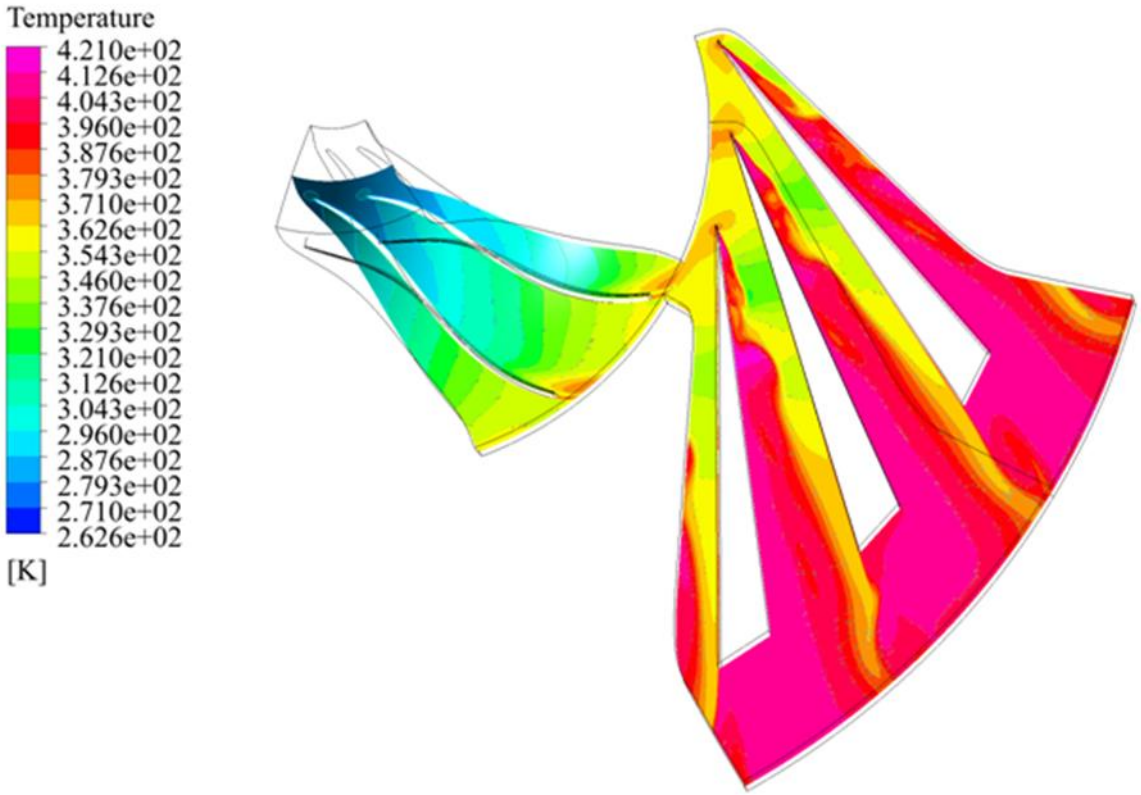

Figure 4-11 Relative Static temperature distribution in the blade-to-blade plane (LES).

➢ **Description:**

The LES model provides a highly detailed static temperature distribution with significant variations and fine-scale structures. The temperature increases from the inlet to the outlet with pronounced fluctuations due to resolved turbulent eddies.

➢ **Observations:**

- The temperature field exhibits high-resolution details with significant spatial variations.

- The highest temperatures are observed near the outlet, with intricate patterns indicating complex flow interactions.
- The temperature distribution captures fine-scale turbulent mixing, showing a more realistic representation of the flow field.

Comparative Analysis:

- **Overall Trends:**
  - All models show an increase in temperature from the inlet to the outlet of the compressor.
  - The LES model captures the most detailed and realistic temperature distribution, while the RANS model shows the smoothest and most averaged field.
  - The URANS model provides an intermediate level of detail, capturing some transient effects but not as extensively as LES.
- **RANS vs. URANS:**
  - The URANS model introduces transient effects, leading to more temperature variations compared to the smoother RANS model.
  - URANS captures some localized temperature peaks, reflecting the intermittent nature of turbulent flows, which are averaged out in RANS.
- **URANS vs. LES:**
  - The LES model shows significantly more detail than the URANS model, with high-resolution temperature fluctuations and fine-scale turbulent structures.
  - LES captures the intricate interactions and mixing in the flow field that are only partially resolved by the URANS model.

4.4.1.4 Analysis of Relative Total Temperature Distribution

RANS Model:

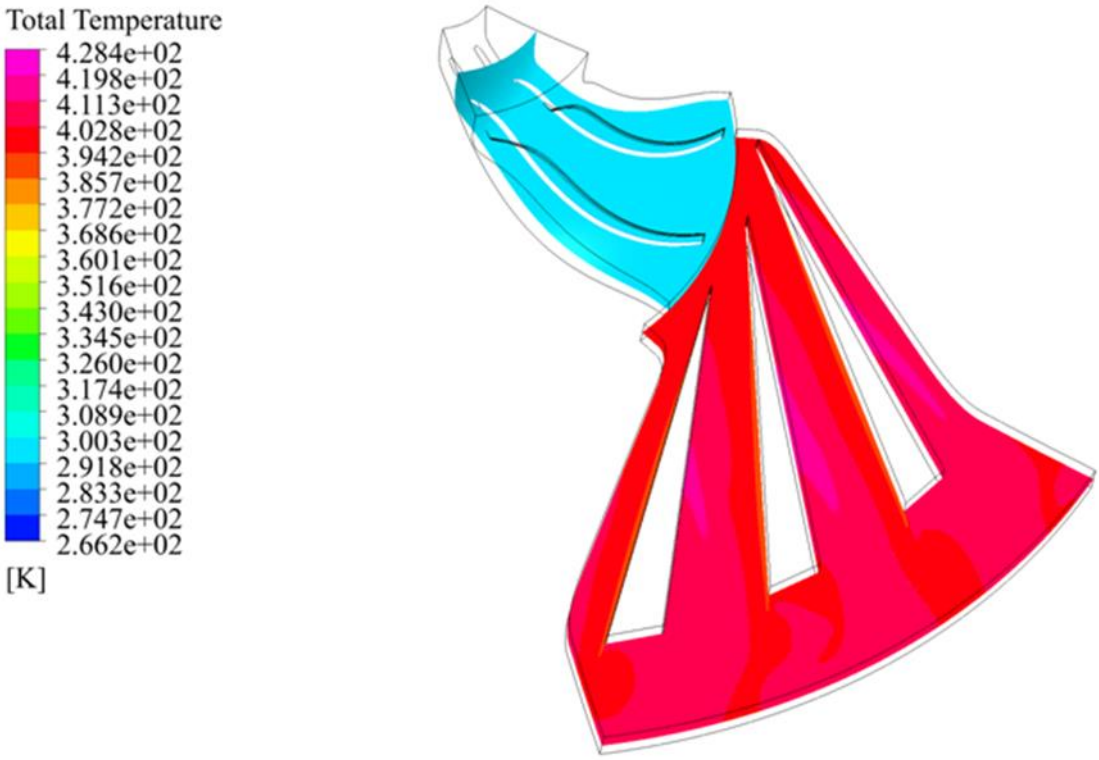

Figure 4-12 Relative Total temperature distribution in the blade-to-blade plane (RANS).

- **Description:**

  The total temperature distribution in the RANS model shows a relatively smooth gradient from the inlet to the outlet of the compressor. The highest temperatures are observed at the outlet near the blade regions, with temperatures reaching up to 428.4 K.

- **Observations:**

  - The temperature is uniformly distributed in the core flow region.
  - There are high-temperature regions along the trailing edges of the blades.

- The temperature drops significantly near the compressor's inlet, with values around 262.6 K.

URANS Model:

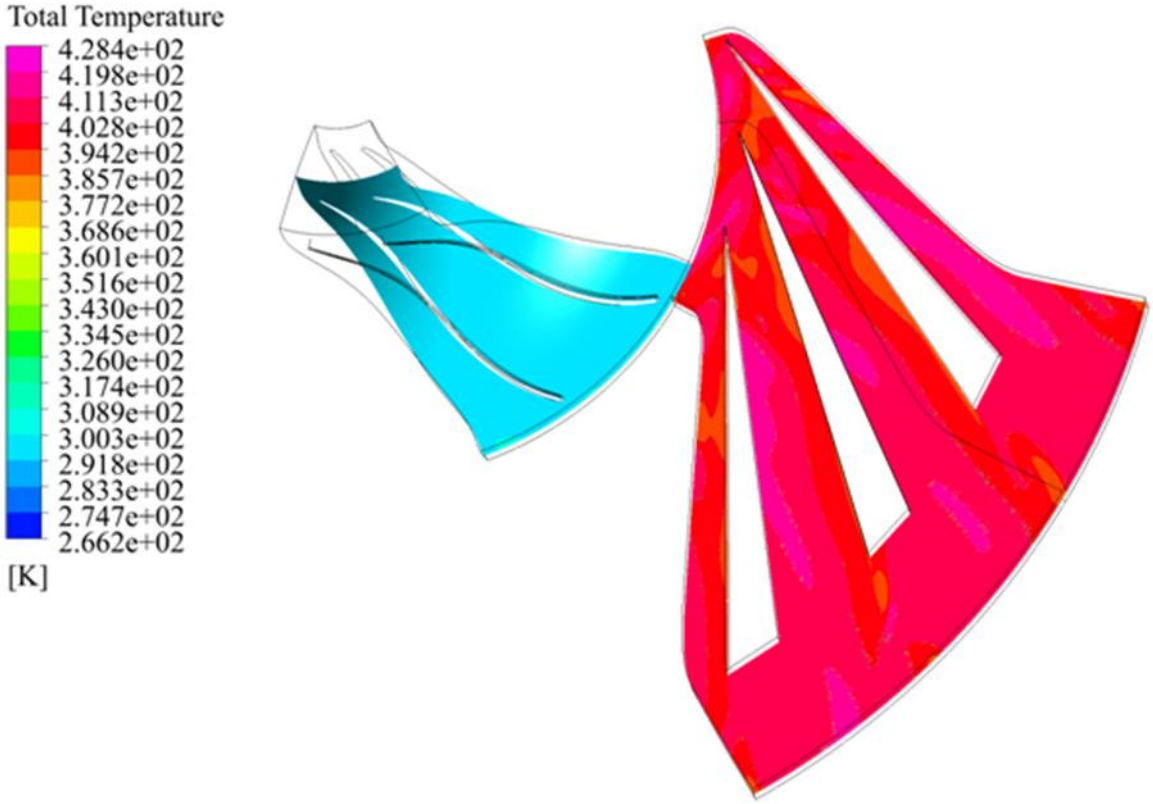

Figure 4-13 Relative Total temperature distribution in the blade-to-blade plane (URANS).

- **Description:**

  The URANS model depicts a similar overall temperature distribution to the RANS model, but with noticeable variations due to unsteady effects. The highest temperatures are also observed near the blade trailing edges, reaching up to 428.4 K.

- **Observations:**

  - Slightly more variation in the temperature contours compared to RANS.
  - The unsteady effects lead to minor temperature fluctuations in the core flow.

- The temperature distribution appears less smooth, indicating transient thermal structures.

LES Model:

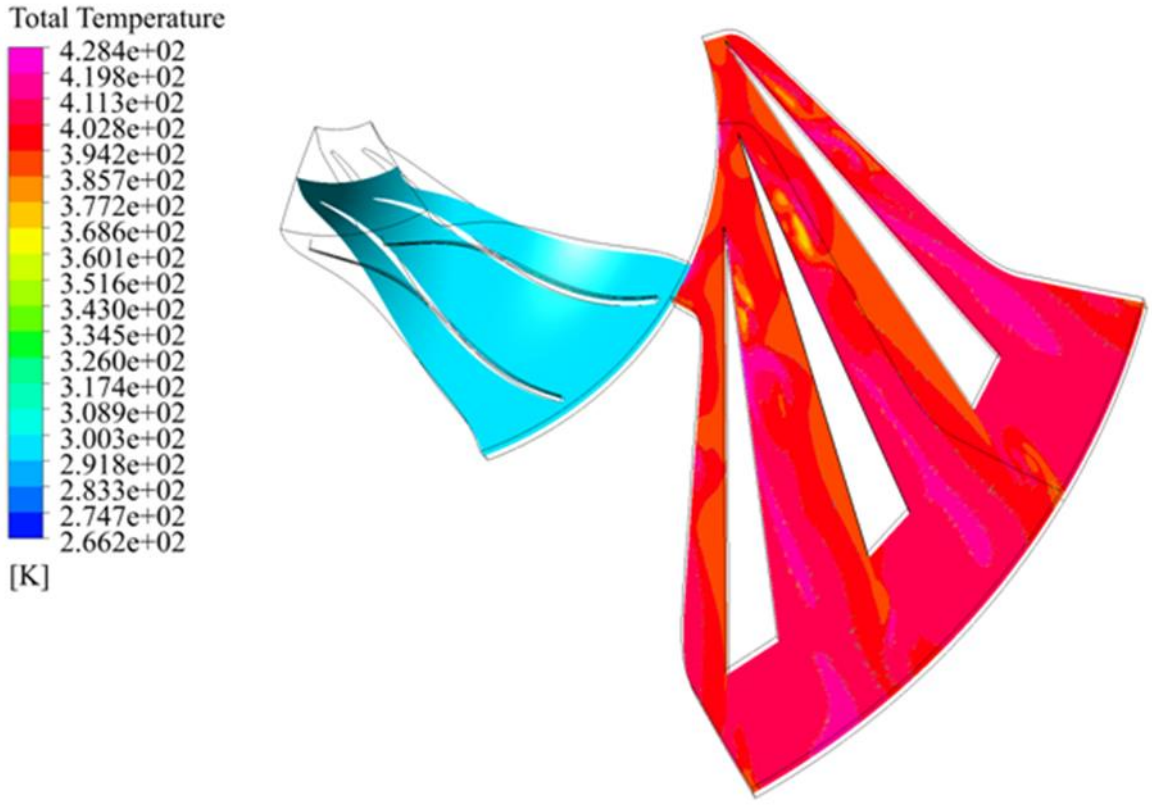

Figure 4-14 Relative Total temperature distribution in the blade-to-blade plane (LES).

- **Description:**

  The LES model shows a more detailed temperature distribution with higher resolution of thermal structures. The highest temperature regions are similar to the other models but show more fine-scale variations, reaching up to 428.4 K.

- **Observations:**

  - Significant small-scale temperature variations are captured.
  - The temperature distribution is less uniform, showing detailed thermal gradients and eddies.
  - High-temperature regions are more dispersed along the blade surfaces and in the wake regions.

Comparative Analysis:

- **High-Temperature Regions:**

  All models show the highest temperatures near the blade trailing edges, with RANS and URANS displaying similar distributions. LES provides a more detailed view of these high-temperature regions, capturing finer thermal structures.

- **Transition and Gradients:**

  The RANS model shows smooth temperature gradients, while the URANS model introduces minor fluctuations due to unsteady effects. The LES model, however, captures detailed transitions and small-scale temperature gradients that are not visible in the RANS or URANS models.

- **Model Selection Impact:**

  - **RANS:** Suitable for a general overview of temperature distribution with less computational cost, but may miss finer details.
  - **URANS:** Provides some unsteady effects, giving a slightly more realistic temperature distribution than RANS, but still limited in capturing detailed structures.
  - **LES:** Offers the most detailed temperature distribution, capturing small-scale variations and transient effects, but at a significantly higher computational cost.

4.4.1.5 Relative Mach Number Analysis

RANS Model:

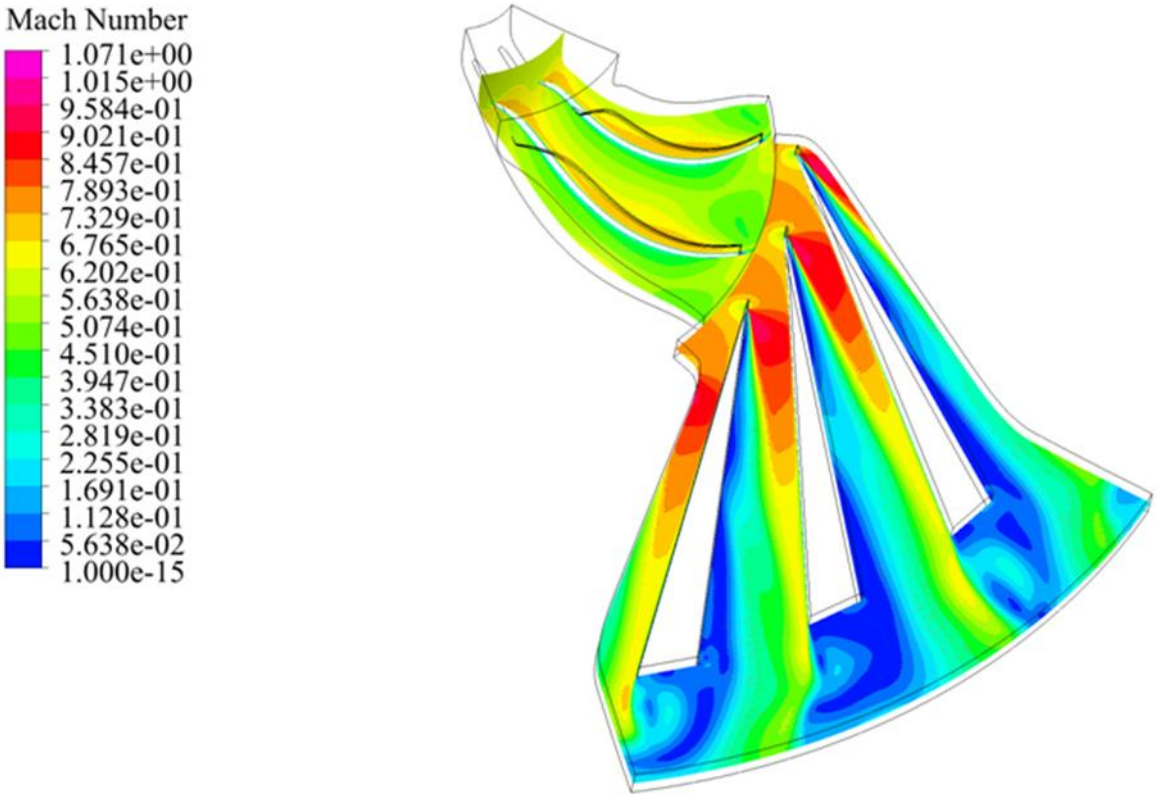

Figure 4-15 Relative Mach number distribution in the blade-to-blade plane (RANS).

- **Description:**

  The RANS model provides an averaged view of the flow, which is beneficial for capturing steady-state characteristics in the compressor.

- **Relative Mach Number Distribution:**
  - **Inlet Region:** The Mach number is relatively low at the inlet, as expected, since the flow is subsonic and gradually accelerates as it moves through the compressor.
  - **Impeller Passage:** There is a noticeable increase in the Mach number as the flow progresses through the impeller blades. The highest Mach numbers are observed at the trailing edges of the blades and near the blade tips, where the flow accelerates significantly.

- **Diffuser and Outlet:** The Mach number decreases in the diffuser section as the flow decelerates and converts kinetic energy into pressure. The RANS model shows a relatively smooth transition in Mach number from the impeller to the diffuser.

➢ **Observations:**

- The Mach number peaks around the leading edges and tips of the blades, indicating strong acceleration and possible shock formation or high-speed flow regions.
- The overall distribution is smooth, highlighting the steady-state nature of the RANS simulation.
- Flow separation or recirculation is not prominently visible, suggesting that RANS captures a stable flow pattern.

URANS Model:

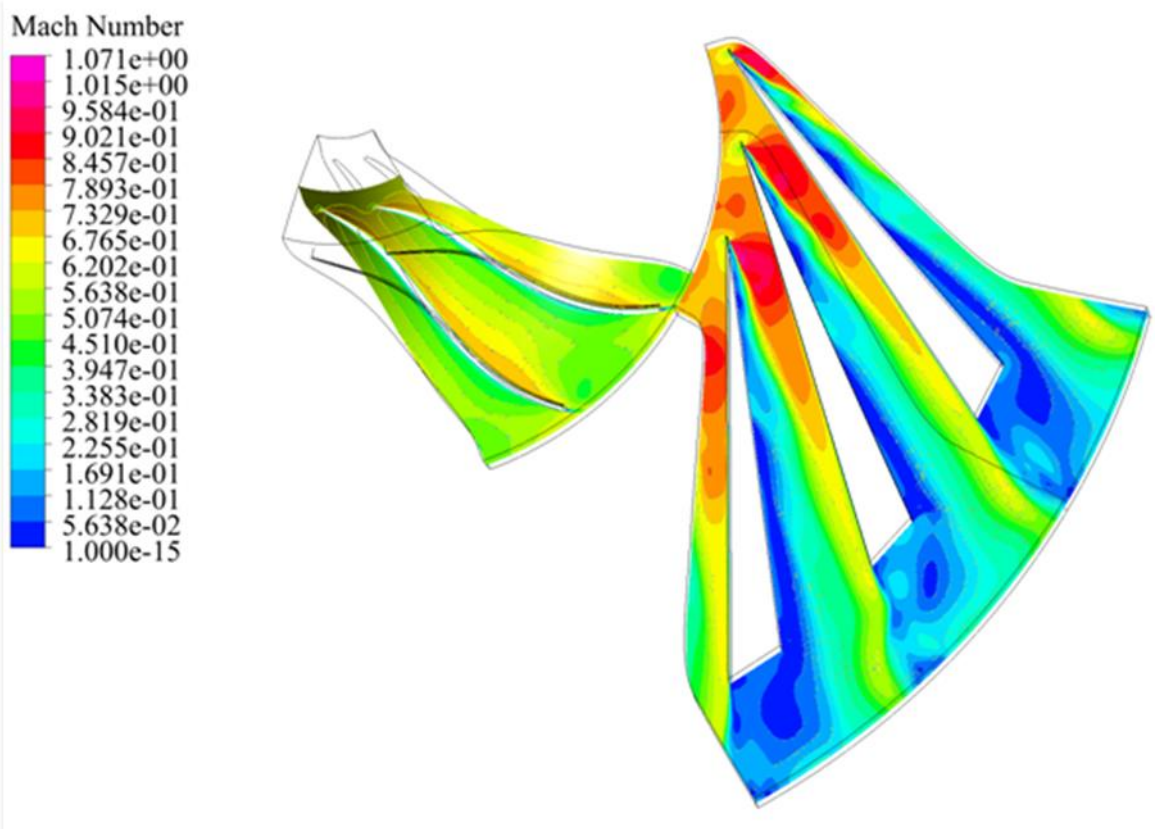

Figure 4-16 Relative Mach number distribution in the blade-to-blade plane (URANS).

- **Relative Mach Number Distribution:**
  - **Inlet Region:** Similar to RANS, the inlet Mach number is low, but URANS shows slight variations over time, suggesting some minor unsteady effects.
  - **Impeller Passage:** The Mach number increases significantly within the impeller blades, with a more pronounced and irregular pattern compared to RANS. This is indicative of transient interactions and possibly some unsteady blade loading.
  - **Diffuser and Outlet:** The Mach number in the diffuser shows fluctuations, capturing the transient behavior of the flow as it decelerates. The transitions between high and low Mach numbers are less smooth compared to RANS.
- **Observations:**
  - URANS captures unsteady flow features, with localized variations in Mach number that could indicate regions of flow separation or intermittent shock waves.
  - There is more complexity in the flow near the blade tips and trailing edges, reflecting the time-dependent nature of the flow.
  - The flow pattern is less smooth, with evidence of fluctuating high-speed regions, which may affect compressor performance and efficiency.

LES Model

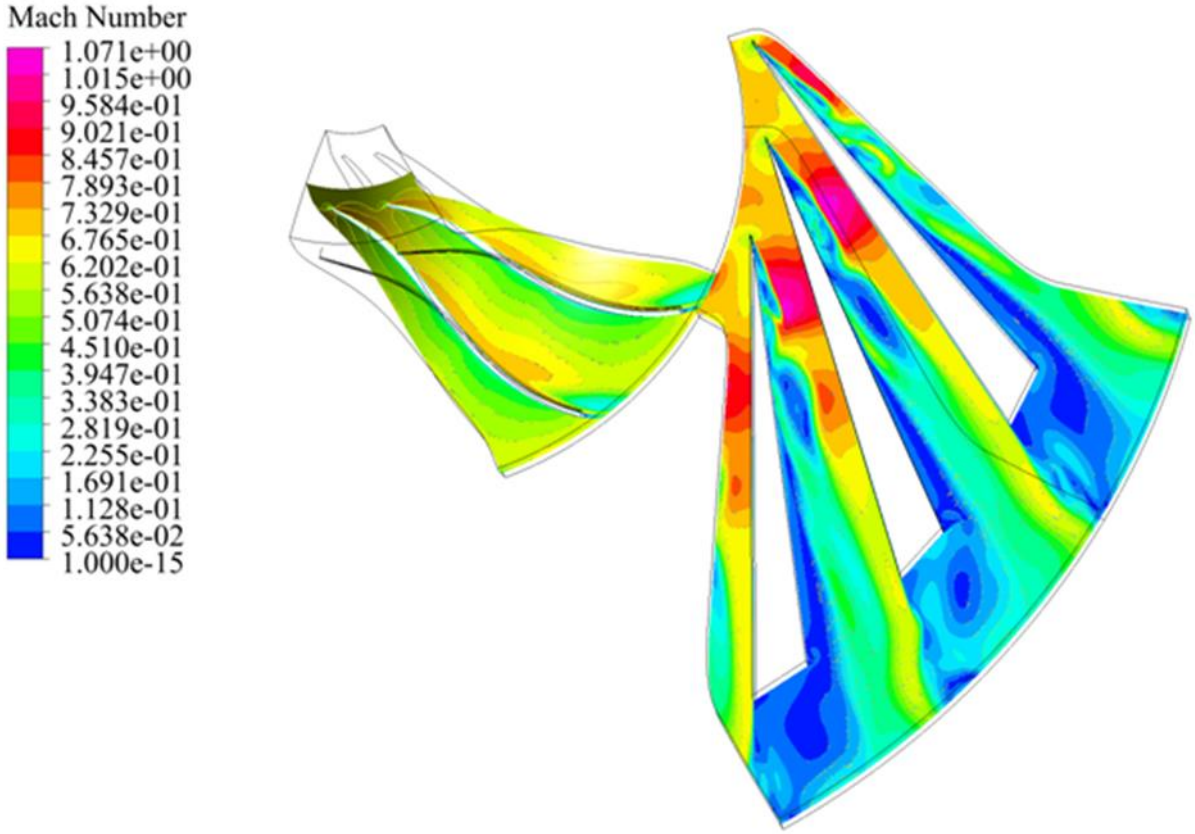

Figure 4-17 Relative Mach number distribution in the blade-to-blade plane (LES).

- **Relative Mach Number Distribution:**
  - **Inlet Region:** The LES model shows a more detailed and varied Mach number distribution at the inlet, reflecting the presence of small-scale turbulent eddies.
  - **Impeller Passage:** Within the impeller blades, the Mach number varies significantly, capturing fine details of turbulent structures and their interactions with the blade surfaces. The regions of high Mach number near the blade tips and trailing edges are more localized and dynamic.
  - **Diffuser and Outlet:** The Mach number in the diffuser shows intricate patterns of deceleration, with clear evidence of turbulence affecting the flow. The LES model captures detailed vortical structures and their influence on Mach number distribution.

- **Observations:**
    - LES provides a highly detailed depiction of the Mach number, showing a range of high and low-speed regions caused by turbulent eddies and complex flow interactions.
    - The flow near the blade tips and trailing edges is more chaotic and dynamic, highlighting the influence of large eddy structures.
    - This model reveals fine-scale variations in Mach number, which are critical for understanding the impact of turbulence on compressor performance and efficiency.

Comparative Analysis:

- **RANS:** Provides a smooth, averaged distribution of the Mach number, suitable for understanding the steady-state performance of the compressor. It lacks the ability to capture transient and turbulent features in detail.
- **URANS:** Offers a middle ground, capturing some unsteady effects and providing a more detailed view than RANS but without the fine-scale resolution of LES. It highlights transient phenomena that could influence compressor dynamics.
- **LES:** Delivers the most detailed and dynamic view, capturing large-scale turbulent structures and their impact on Mach number distribution. It is ideal for understanding the intricate flow behaviors and their effects on compressor performance but at a higher computational cost.

4.4.1.6 Relative Static Entropy Analysis

RANS Model:

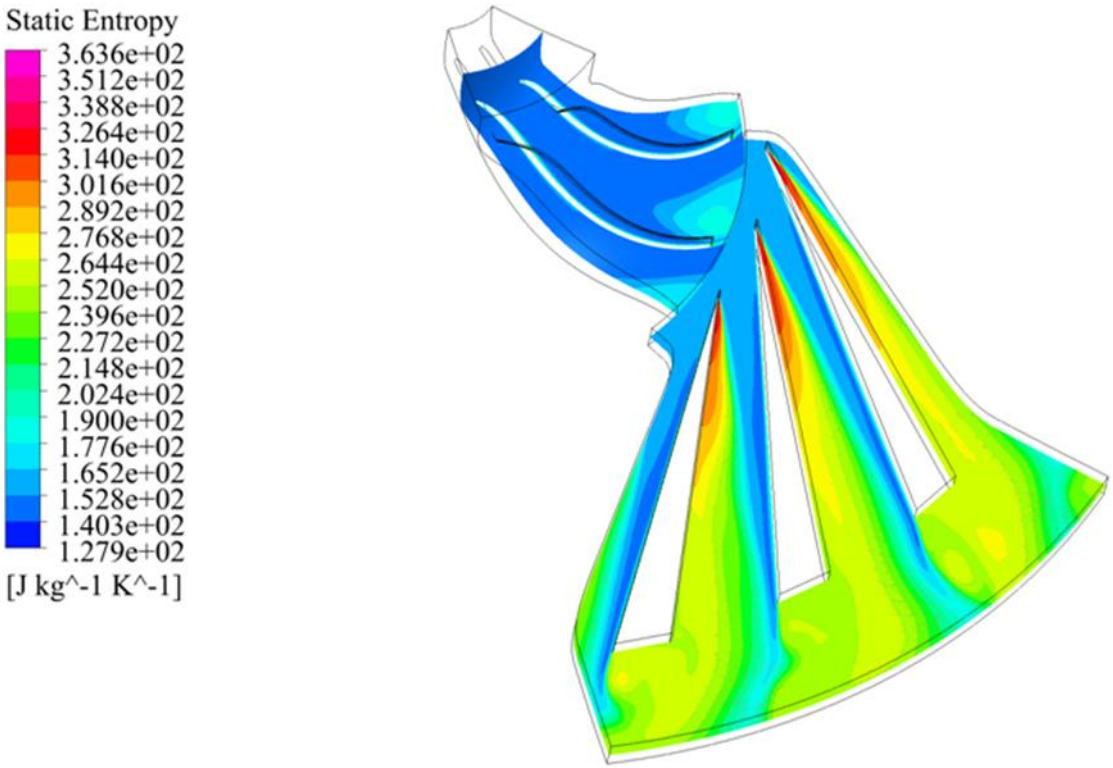

Figure 4-18 Relative Static entropy distribution in the blade-to-blade plane (RANS).

- **Overall Entropy Distribution:**
  - The static entropy values range from approximately 127.9 J/kg·K to 363.6 J/kg·K.
  - The blue regions (lower entropy) are predominantly found near the inlet and along the streamline in the upper part of the plane.
  - Higher entropy values (yellow to red regions) are observed near the blade leading and trailing edges, indicating higher losses and inefficiencies in these areas.
- **Flow Characteristics:**
  - The low entropy region suggests smoother flow and lower losses near the inlet.Higher entropy generation near the blades indicates areas with significant viscous dissipation and possible flow separation.

URANS Model:

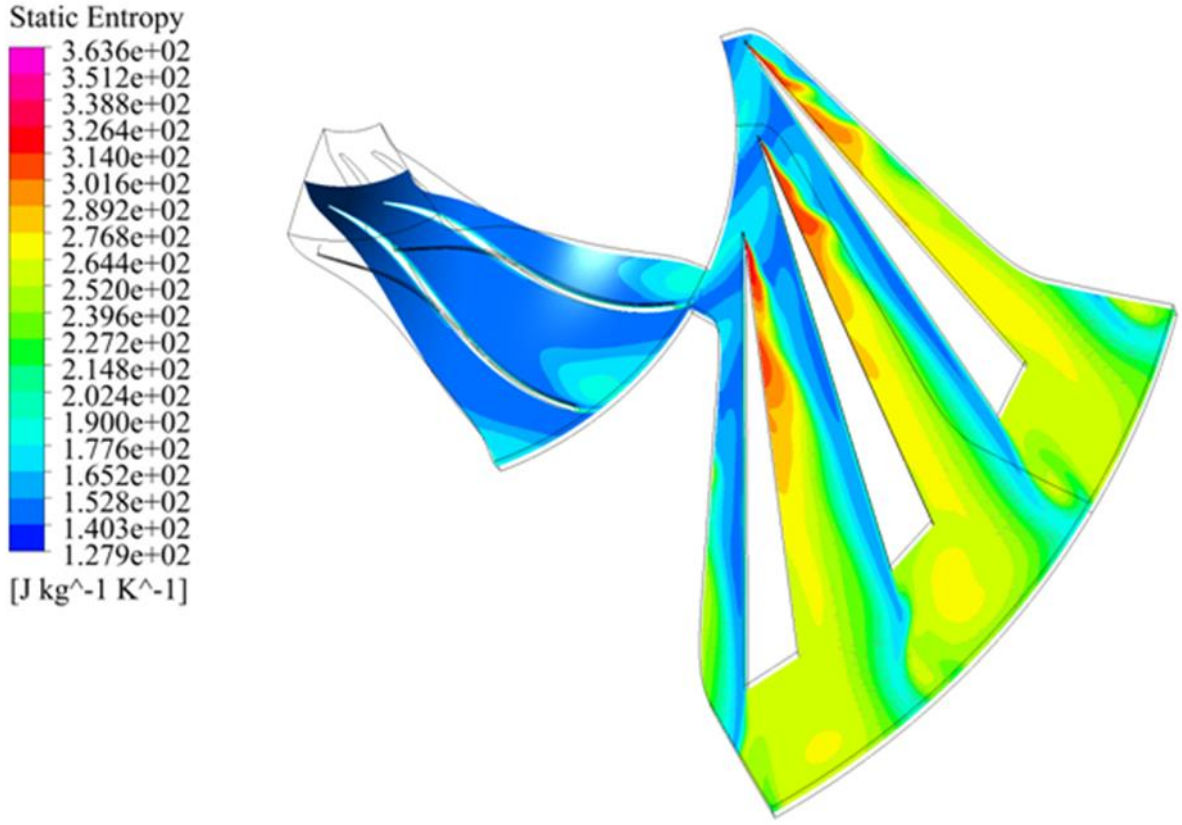

Figure 4-19 Relative Static entropy distribution in the blade-to-blade plane (URANS).

- **Overall Entropy Distribution:**
  - The static entropy values have a similar range, from approximately 127.9 J/kg·K to 363.6 J/kg·K.
  - The distribution pattern is somewhat similar to RANS, with blue regions near the inlet and higher entropy near the blades.
  - However, URANS shows slightly more detailed structures in the entropy distribution, with more defined regions of higher entropy.
- **Flow Characteristics:**
  - URANS captures more transient effects and unsteady flow features compared to RANS.
  - The more detailed high entropy regions suggest more accurate capturing of turbulent mixing and viscous dissipation.

- Overall, URANS may provide a better representation of the actual flow losses and inefficiencies.

LES Model:

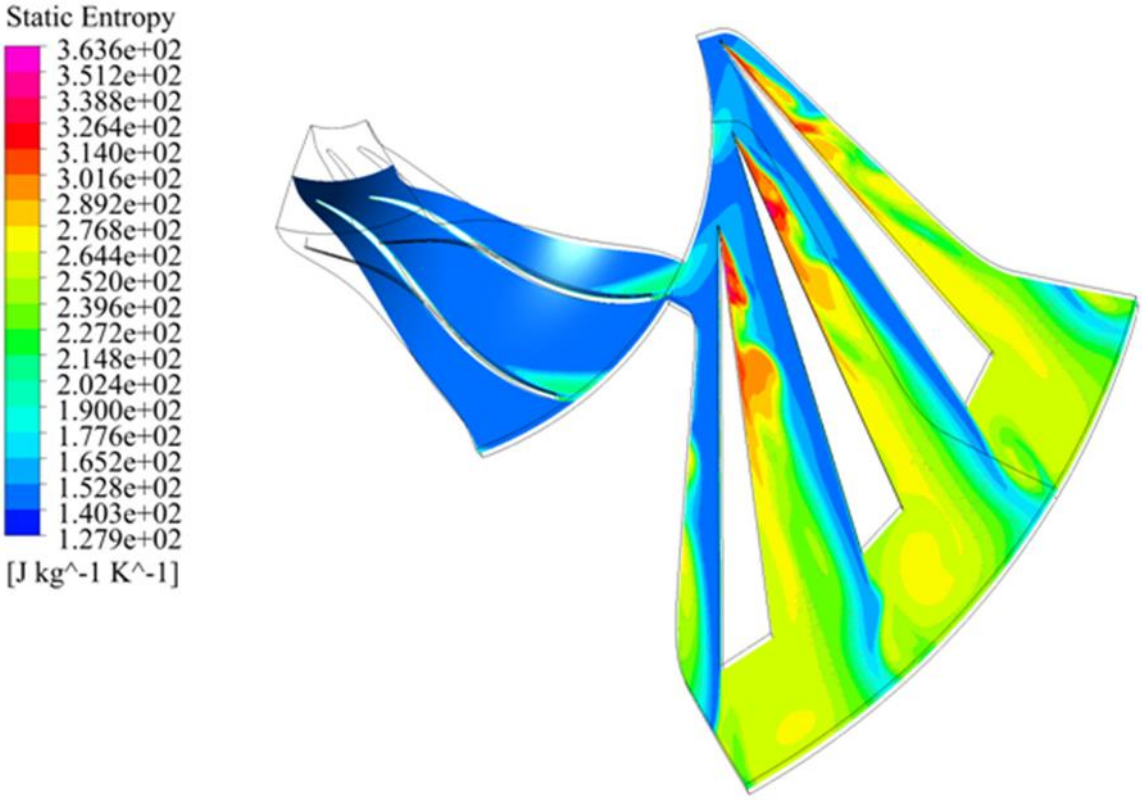

Figure 4-20 Relative Static entropy distribution in the blade-to-blade plane (LES).

- **Overall Entropy Distribution:**
  - The static entropy values again range from approximately 127.9 J/kg·K to 363.6 J/kg·K.
  - LES shows the most detailed entropy distribution among the three models, with a finer resolution of high entropy regions.
  - The high entropy regions near the blades are more pronounced and detailed, indicating higher fidelity in capturing small-scale turbulent structures.
- **Flow Characteristics:**
  - LES provides the most accurate depiction of the flow's unsteady and turbulent nature.
  - The detailed high entropy regions suggest that LES captures the fine-scale turbulent mixing and viscous dissipation more effectively.

- This high fidelity in capturing flow details is crucial for understanding the true nature of losses and inefficiencies in the compressor.

Comparative Analysis:

- **Entropy Generation and Losses:**
  - **RANS** shows a more averaged and less detailed entropy distribution, indicating its limitation in capturing transient and small-scale turbulent effects.
  - **URANS** improves upon RANS by incorporating unsteady effects, resulting in a more detailed entropy distribution and better representation of flow losses.
  - **LES** provides the most detailed and accurate entropy distribution, highlighting its superiority in capturing the intricate details of turbulent flow and associated losses.
- **Model Suitability:**
  - **RANS** is suitable for preliminary design and analysis due to its lower computational cost may not capture all flow details accurately.
  - **URANS** offers a balance between computational cost and accuracy, making it suitable for more detailed design analysis.
  - **LES** is the most computationally expensive but provides the highest accuracy, making it ideal for final design verification and detailed flow studies.

4.4.2 Meridional Projection Plane

4.4.2.1 Relative Static Pressure Analysis

RANS Model:

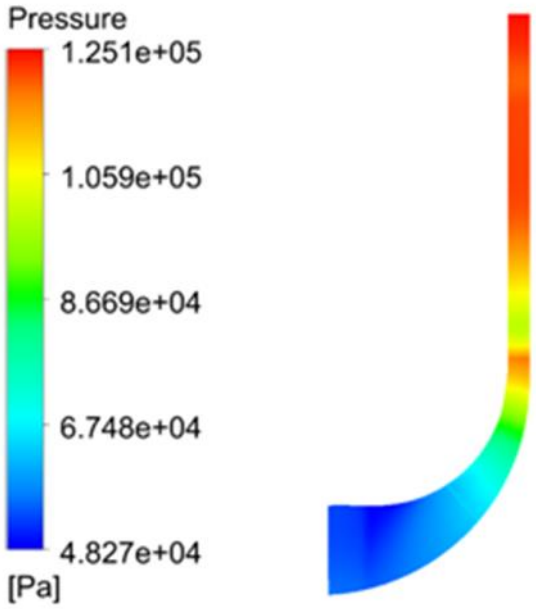

Figure 4-21 Relative Static pressure distribution in the meridional plane (RANS).

- **Description**:
  - The static pressure increases smoothly from the inlet (bottom) to the outlet (top).
  - The pressure distribution appears relatively uniform, with a clear gradient from low (blue) to high (red) pressure.
- **Key Characteristics**:
  - **Smooth Pressure Gradient**: The static pressure gradient is steady and smooth, indicating that the RANS model has captured the general trend of pressure increase but may have smoothed out smaller fluctuations.

- **Potential Limitations**: RANS might not fully capture detailed flow separation or secondary flow effects, leading to a more averaged and less detailed pressure field.

URANS Model:

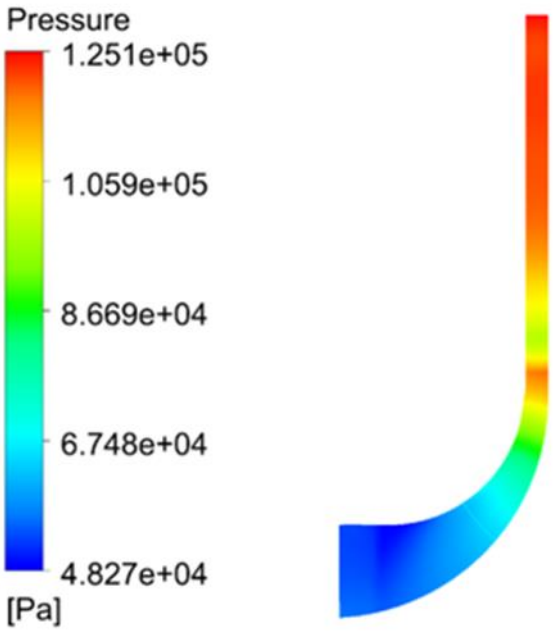

Figure 4-22 Relative Static pressure distribution in the meridional plane (URANS).

➢ **Description**:

- Similar overall pressure increase from inlet to outlet, but with slightly more variations compared to RANS.
- Slightly higher spatial resolution in the pressure field, especially near regions where flow acceleration or deceleration occurs.

➢ **Key Characteristics**:

- **Increased Detail**: Compared to RANS, URANS shows minor transient effects that provide more detail in the pressure distribution, particularly in regions where flow interactions are more complex.

- **Intermediate Complexity**: While not as detailed as LES, URANS provides a balance between capturing transient phenomena and maintaining computational efficiency.

LES Model:

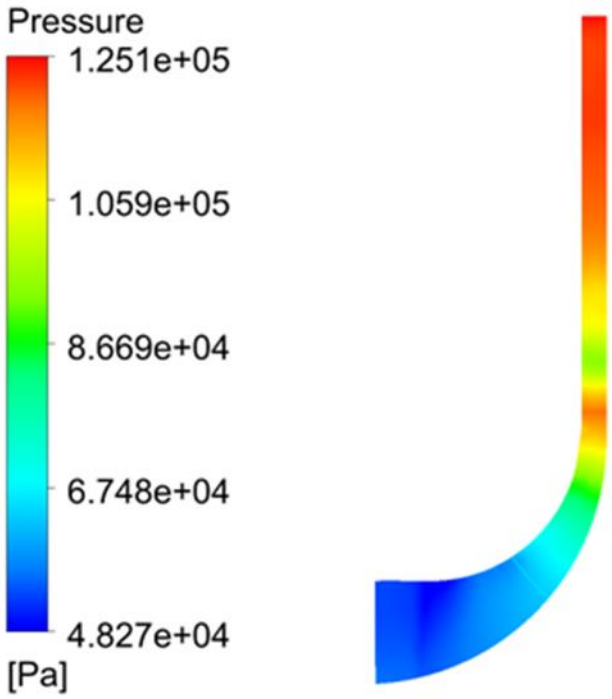

Figure 4-23 Relative Static pressure distribution in the meridional plane (LES).

➢ **Description**:

- The static pressure distribution shows more fine-scale variations and fluctuations compared to RANS and URANS.
- Detailed pressure changes are visible throughout the flow path, indicating a more complex interaction of flow structures.

- **Key Characteristics**:
    - **High Resolution**: LES captures small-scale variations and pressure fluctuations, especially in regions where flow separation or secondary flows are significant.
    - **Detailed Flow Features**: This model reflects a higher fidelity in capturing turbulence and flow instabilities, leading to a more detailed and accurate pressure field.

Comparative Analysis:

- **Uniformity**:
    - **RANS** provides the smoothest pressure gradient with minimal fine details, which is expected due to its averaging nature.
    - **URANS** captures some transient effects, adding slight variations compared to RANS, but still smooth in general.
    - **LES** shows the highest level of detail and variations in the static pressure distribution, indicating the capture of complex flow phenomena.
- **Flow Details**:
    - **RANS** may not accurately capture complex flow structures, such as vortices or separation zones, leading to a more averaged pressure distribution.
    - **URANS** offers an intermediate view, capturing some unsteady effects while maintaining a relatively smooth pressure field.
    - **LES** excels in capturing fine-scale turbulence and flow interactions, resulting in a more detailed and fluctuating pressure field.
- **Computational Implications**:
    - **RANS** is computationally efficient but may lack accuracy in capturing detailed flow dynamics.
    - **URANS** provides a balance between computational cost and capturing transient effects.

- **LES** is computationally intensive but offers the most detailed and accurate representation of static pressure variations.

4.4.2.2 Relative Static Temperature Analysis

RANS Model:

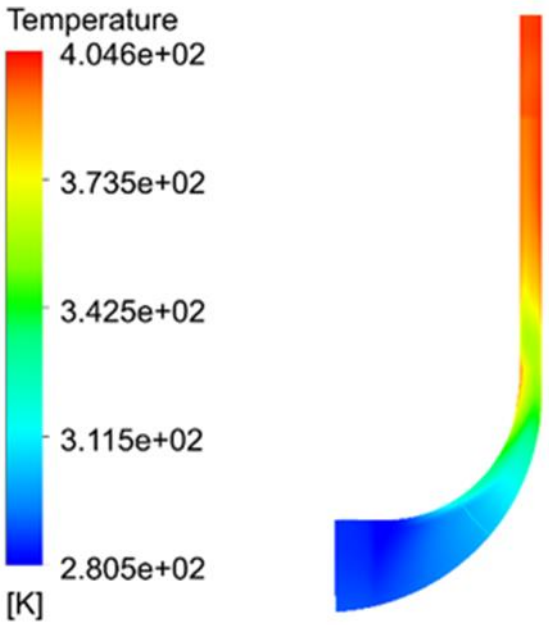

Figure 4-24 Relative Static temperature distribution in the meridional plane (RANS).

- **Temperature Range:**

  The static temperature ranges from approximately 280.5 K to 404.6 K.

- **Distribution:**

  - The RANS model shows a gradual increase in temperature from the inlet to the outlet. The highest temperatures are observed near the outlet, which is consistent with expected behavior due to compressive heating as the air passes through the compressor.

- **Observation:**

  - The temperature distribution appears relatively smooth with minimal variation, indicating that RANS captures the general trend but may lack finer details due to the averaging of turbulent fluctuations.

URANS Model:

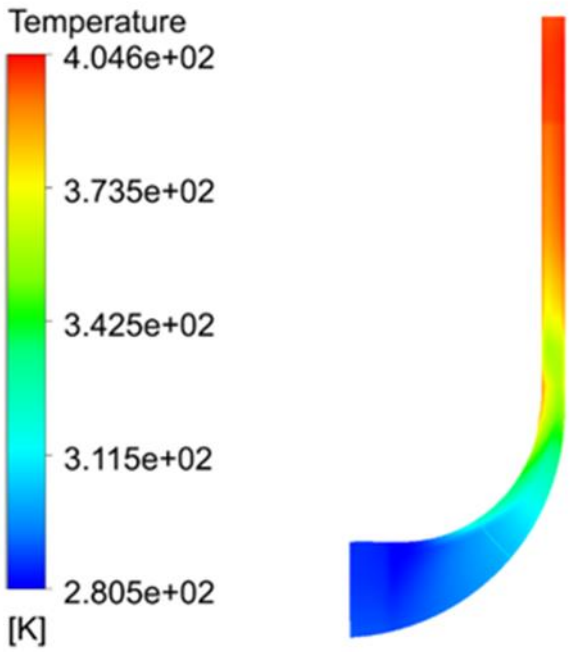

Figure 4-25 Relative Static temperature distribution in the meridional plane (URANS).

- **Temperature Range:**

  Similar to RANS, the temperature ranges from approximately 280.5 K to 404.6 K.

- **Distribution:**

  - The URANS model also shows a gradual temperature increase from inlet to outlet. The temperature gradient is comparable to that of the RANS model.

- **Observation:**

  - URANS captures slightly more unsteady effects compared to RANS, but the overall temperature distribution remains similar. This suggests that URANS

provides a slight improvement in capturing transient effects but may not significantly enhance temperature detail over RANS.

LES Model:

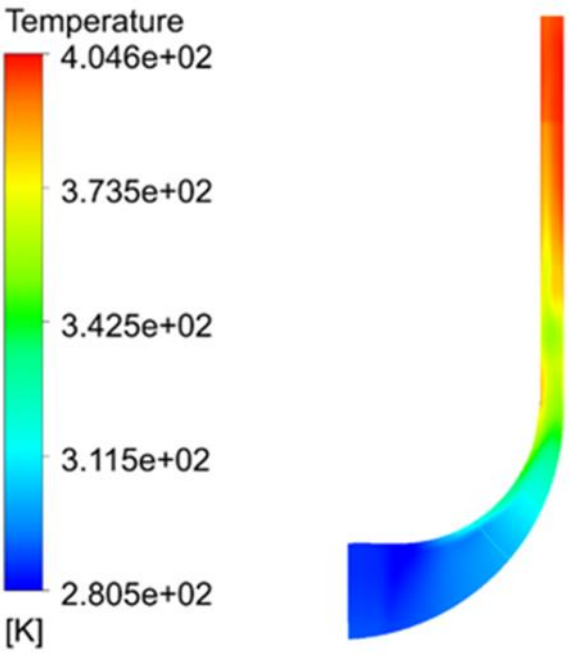

Figure 4-26 Relative Static temperature distribution in the meridional plane (LES).

- **Temperature Range:**

  The temperature range is again approximately 280.5 K to 404.6 K.

- **Distribution:**

  - The LES model displays a similar overall trend of increasing temperature from inlet to outlet. However, there are more pronounced variations and finer details in the temperature field.

- **Observation:**

  - LES captures more detailed temperature fluctuations, especially in regions with higher turbulence. This model provides a more accurate representation of the

temperature distribution, reflecting the impact of smaller eddies and transient effects more effectively than RANS and URANS.

Comparative Analysis:

- **Temperature Range:**

  All three models predict a similar range of static temperature, indicating consistency in the overall thermal behavior.

- **Smoothness vs. Detail:**

  RANS provides a smooth temperature distribution, suitable for capturing the general trend. URANS offers a slight improvement by accounting for some unsteady effects, but the overall pattern remains similar to RANS. LES, on the other hand, captures finer details and more accurate transient effects, offering a more detailed and realistic temperature distribution.

- **Computational Cost vs. Accuracy:**

  While RANS is computationally less expensive and captures the general trends well, LES, though more computationally demanding, provides a significantly more detailed and accurate depiction of the temperature field. URANS serves as a middle ground but does not offer substantial improvements over RANS in terms of temperature distribution.

4.4.2.3 Relative Mach Number Analysis

RANS Model:

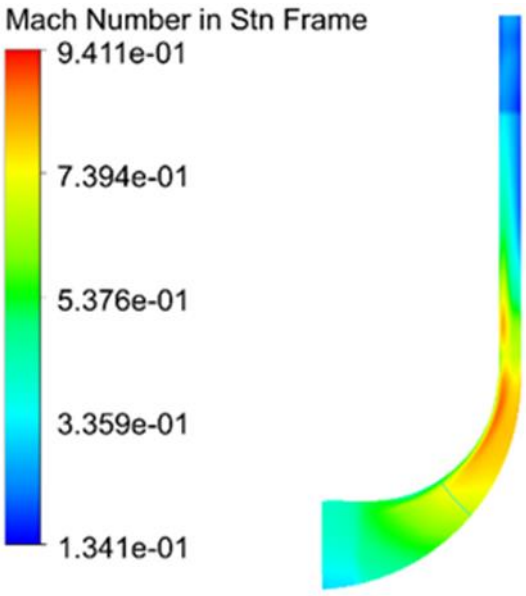

Figure 4-27 Relative Mach number distribution in the meridional plane (RANS).

- **Flow Characteristics**:
  - The Mach number distribution is relatively smooth and shows a gradual increase from the inlet to the outlet.
  - The highest Mach number, approximately 0.94, occurs near the compressor outlet.
  - Flow acceleration is visible, especially near the curved regions of the compressor, where the Mach number increases due to the curvature and reduction in cross-sectional area.
- **Turbulence Effects**:
  - RANS provides an averaged representation of turbulence, leading to a smoother Mach number distribution.
  - This model might not capture finer turbulence-induced variations but gives a clear overview of the average flow characteristics.

URANS Model:

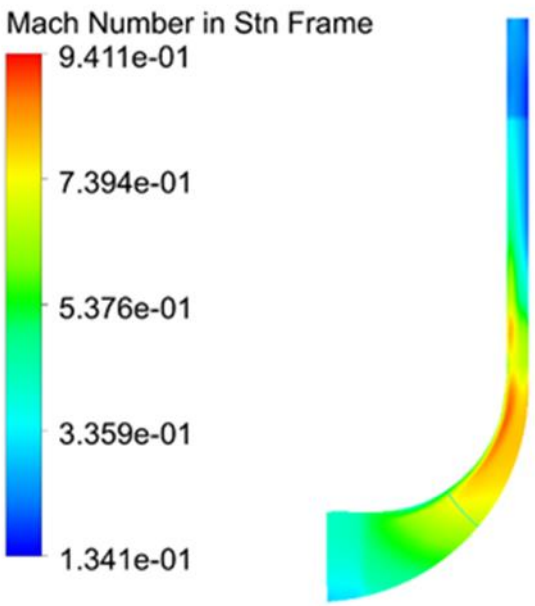

Figure 4-28 Relative Mach number distribution in the meridional plane (URANS).

- **Flow Characteristics**:
  - The Mach number distribution shows slight variations compared to RANS, indicating unsteady effects in the flow.
  - There is a noticeable unsteady pattern, especially near the outlet, where the highest Mach number (approximately 0.94) is observed.
  - The distribution is less smooth than RANS, showing areas of acceleration and deceleration due to transient effects.
- **Turbulence Effects**:
  - URANS captures unsteady turbulent effects, leading to minor fluctuations in the Mach number distribution.
  - These unsteady effects can highlight regions prone to flow separation and reattachment, which are not as visible in the RANS results.

LES Model:

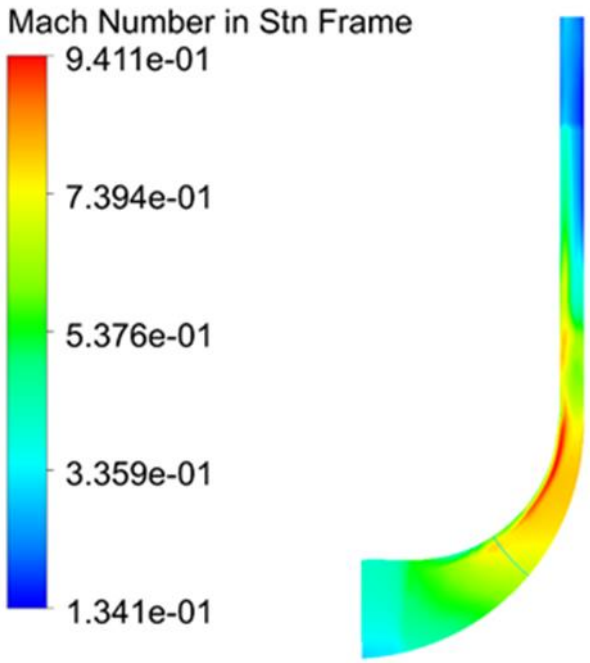

Figure 4-29 Relative Mach number distribution in the meridional plane (LES).

- **Flow Characteristics**:
  - The Mach number distribution is highly detailed, showing significant fluctuations throughout the flow path.
  - The highest Mach number, approximately 0.94, is observed near the outlet, similar to the other models.
  - LES captures small-scale variations and transient phenomena in the flow, providing a detailed picture of the flow acceleration and deceleration.
- **Turbulence Effects**:
  - LES provides a high-fidelity representation of turbulence, capturing detailed and transient variations in the Mach number.
  - The fluctuations indicate the presence of complex flow structures and turbulent eddies, which are not captured by RANS and URANS.

- This model is effective in highlighting areas with potential flow instabilities and high turbulence intensity.

4.4.2.4 Relative Static Entropy Analysis

RANS Model

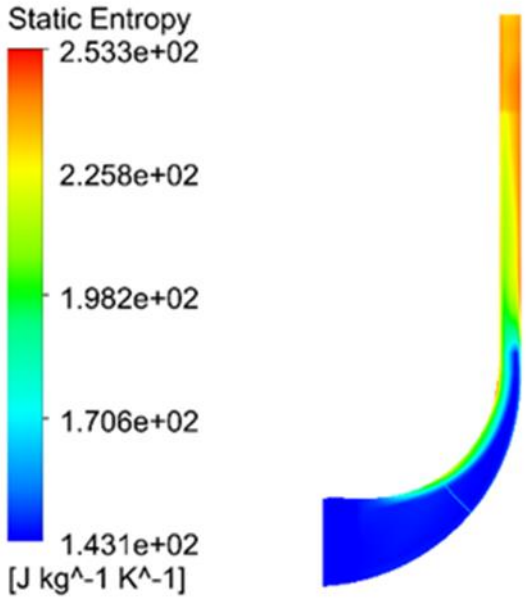

Figure 4-30 Relative Static entropy distribution in the meridional plane (RANS).

- **Description**:

In the Meridional Projection plane, the RANS model depicts a smooth and consistent increase in static entropy from the inlet to the outlet of the compressor. This gradual rise in entropy is a hallmark of the time-averaged nature of the RANS approach.

- **Observations**:
  - **Gradual Increase**: Entropy gradually climbs as the flow progresses through the compressor, reflecting a steady accumulation of losses.
  - **Peak Concentration**: The highest entropy values gather near the outer periphery at the outlet, indicative of maximal energy dissipation in this region.
  - **Uniform Core**: The core region maintains a steady increase without notable spatial variations, suggesting limited mixing and turbulence.

URANS Model

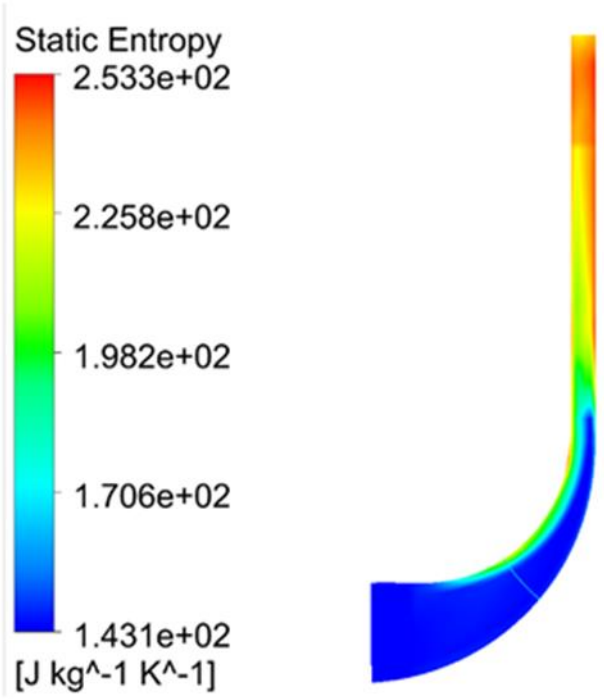

Figure 4-31 Relative Static entropy distribution in the meridional plane (URANS).

- **Description**:

  The URANS model adds a layer of complexity with its depiction of static entropy, introducing transient fluctuations that disrupt the otherwise smooth gradient seen in the RANS results.

- **Observations**:
  - **Transient Fluctuations**: Small but noticeable entropy variations appear, hinting at the underlying unsteady phenomena.
  - **Localized Peaks**: The entropy distribution shows localized peaks, highlighting areas where transient turbulent mixing is more pronounced.
  - **Slightly Higher Values**: Entropy values are slightly elevated compared to RANS, especially near regions of flow instability and interaction.

LES Model

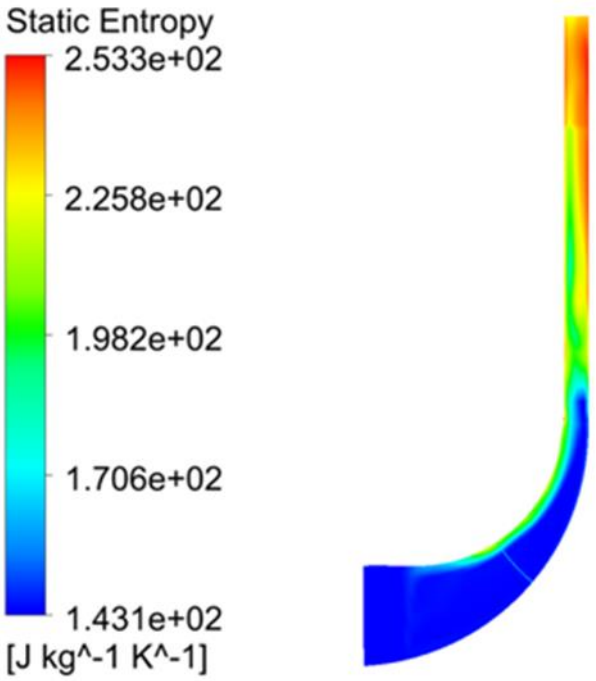

Figure 4-32 Relative Static entropy distribution in the meridional plane (LES).

- **Description**:

  The LES model offers a vivid and intricate picture of static entropy, capturing the fine-scale turbulent structures and their effects on the entropy distribution with remarkable detail.

- **Observations**:
  - **High-Resolution Details**: The entropy field is richly detailed, showing significant spatial variations and intricate patterns.
  - **Complex Interactions**: The highest entropy values, observed near the outlet, form intricate patterns that reveal complex flow interactions and energy dissipation mechanisms.
  - **Fine-Scale Turbulence**: The LES model captures the fine-scale turbulent mixing, providing a realistic and detailed representation of the flow's thermodynamic behavior.

Comparative Analysis:

- **Overall Trends**:
  - **Increasing Entropy**: Across all models, entropy consistently increases from the inlet to the outlet, highlighting the cumulative nature of energy losses in the compressor.
  - **Detail and Accuracy**: LES stands out for its detailed and realistic entropy distribution, while RANS provides a smooth and averaged view. URANS offers a compromise, capturing some transient effects but not the full detail of LES.
- **RANS vs. URANS**:
  - **Smooth vs. Transient**: RANS offers a smooth, time-averaged entropy field, whereas URANS introduces transient effects, leading to more entropy variations and localized peaks.
  - **Energy Dissipation**: URANS captures the unsteady behavior of turbulent flows better than RANS, showing slightly higher and more varied entropy values.
- **URANS vs. LES**:
  - **Intermediate vs. Detailed**: While URANS captures some transient phenomena, LES provides a much more detailed and accurate depiction of the entropy distribution.
  - **Fine-Scale Structures**: LES reveals intricate fine-scale turbulent structures and their impact on entropy, something only partially resolved by URANS.

4.4.3 Orthogonal Cut Projection Plane

4.4.3.1 Relative Static Entropy Analysis

RANS Model

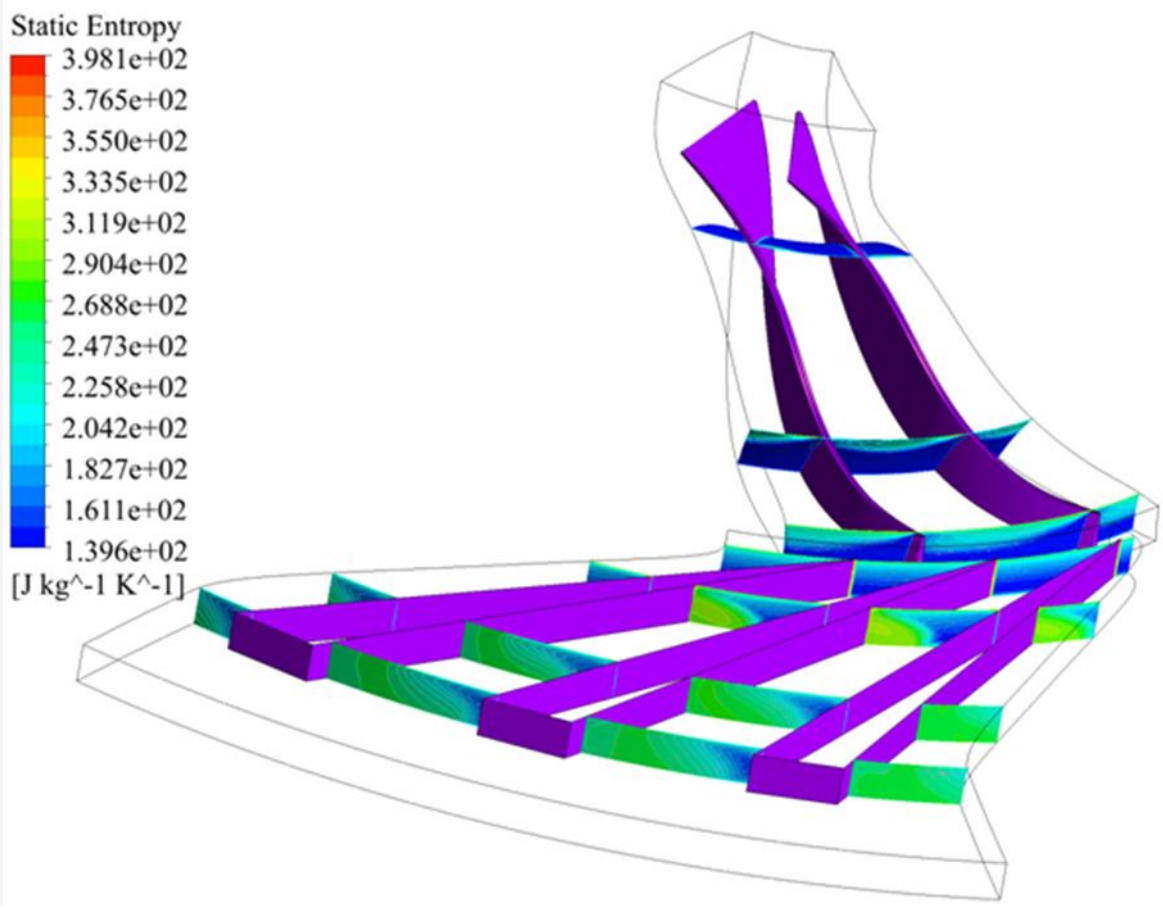

Figure 4-33 Relative Static entropy distribution in the orthogonal plane (RANS).

- **Observations:**
  - The static entropy values range from 139.6 J/kg·K to 398.1 J/kg·K.
  - Higher entropy regions are observed along the blade surfaces, especially towards the trailing edge, indicating higher losses.
  - The entropy distribution shows a gradient from the hub to the shroud, with higher entropy near the shroud.
  - The presence of high entropy in certain areas suggests energy losses and possible inefficiencies in the flow due to turbulence and flow separation.

URANS Model

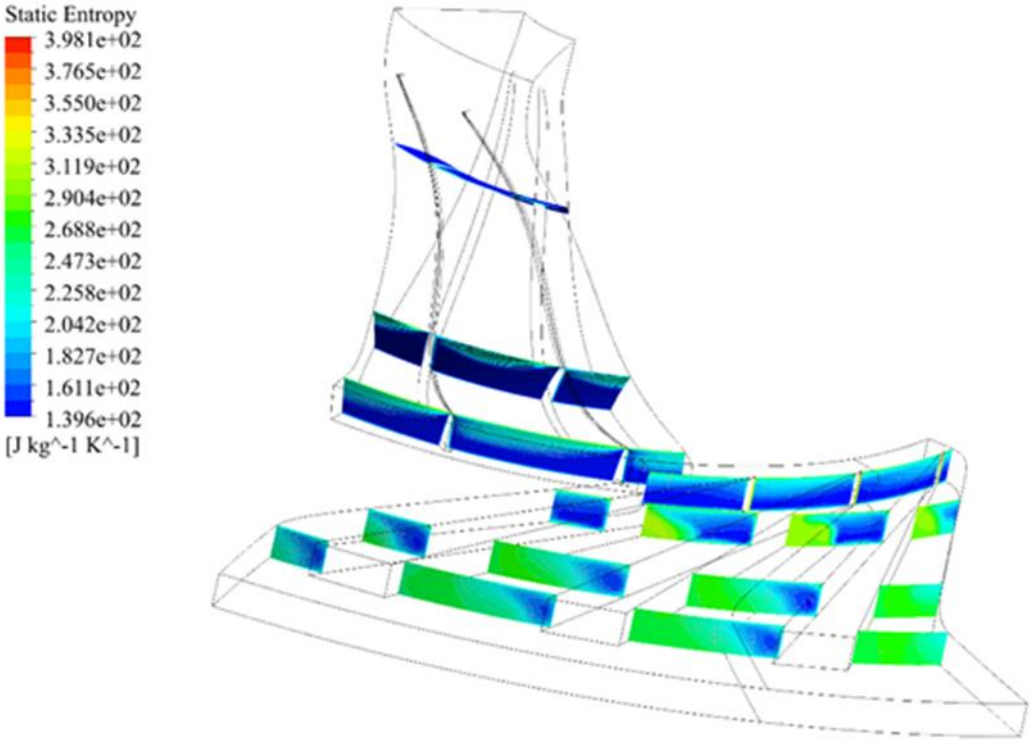

Figure 4-34 Relative Static entropy distribution in the orthogonal plane (URANS).

- **Observations:**
  - The static entropy values range from 139.6 J/kg·K to 398.1 J/kg·K, similar to the RANS model.
  - The URANS model shows a more evenly distributed entropy field compared to RANS.
  - Higher entropy regions are still present near the blade surfaces but appear less intense than in the RANS model.
  - The entropy gradient is smoother, indicating that URANS captures some of the unsteady effects, reducing the peak entropy values and distributing them more evenly.

LES Model

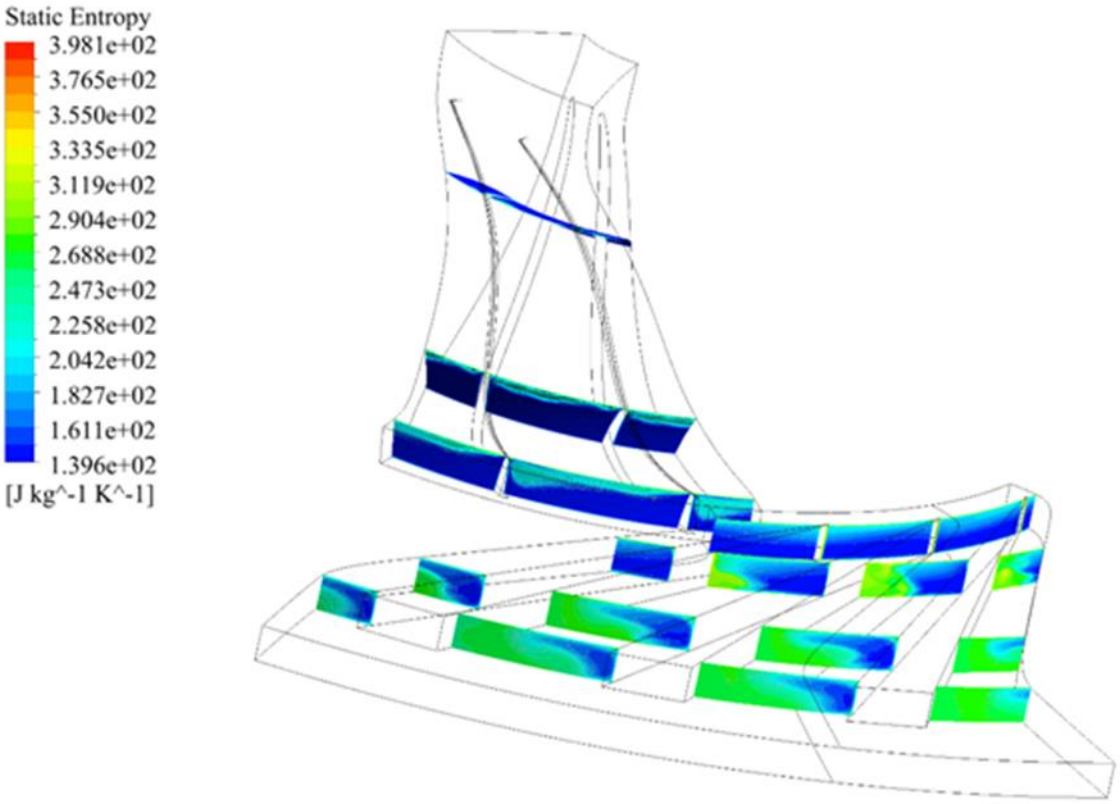

Figure 4-35 Relative Static entropy distribution in the orthogonal plane (LES).

- **Observations:**
  - The static entropy values again range from 139.6 J/kg·K to 398.1 J/kg·K.
  - The LES model provides a much more detailed and varied entropy distribution, capturing fine-scale turbulence and unsteady flow features.
  - High entropy regions are less pronounced compared to RANS and URANS, with more localized spots of high entropy.
  - LES captures the small-scale eddies and turbulence effects, resulting in a more accurate representation of entropy variations across the plane.

Comparative Analysis:

- **RANS**: Shows higher and more concentrated entropy regions indicating higher losses. It is less capable of capturing unsteady and fine-scale turbulent effects, leading to a more averaged and possibly less accurate entropy field.

- **URANS**: Provides a smoother entropy distribution, capturing some unsteady effects and reducing peak entropy values. It strikes a balance between computational cost and accuracy, offering better results than RANS but still missing finer details.
- **LES**: Offers the most detailed and accurate entropy distribution, capturing small-scale turbulence and providing a nuanced view of entropy variations. This model highlights localized losses more effectively, suggesting better performance in predicting real-world compressor behavior but at a higher computational cost.

Implications for Compressor Performance :

- **Efficiency and Losses**: The RANS model shows higher and more concentrated entropy, indicating higher predicted losses and lower efficiency. URANS improves on this by smoothing out the entropy field and reducing peaks, suggesting better performance. LES, with its detailed and accurate entropy distribution, indicates lower overall losses and higher efficiency.
- **Flow Characteristics**: LES captures the complex flow structures and unsteady phenomena better than RANS and URANS. This results in a more accurate prediction of flow behavior and associated losses.
- **Model Selection**: While LES provides the most accurate results, its high computational cost may not be justified for all applications. URANS offers a good compromise, improving accuracy over RANS without the extensive computational requirements of LES.

In summary, for the static entropy comparison in the orthogonal cut projection plane, LES emerges as the most accurate model in capturing detailed flow features and entropy variations, followed by URANS and then RANS. The choice of model should consider the balance between required accuracy and available computational resources.

4.4.4 Comments on Relative Static Pressure Plot

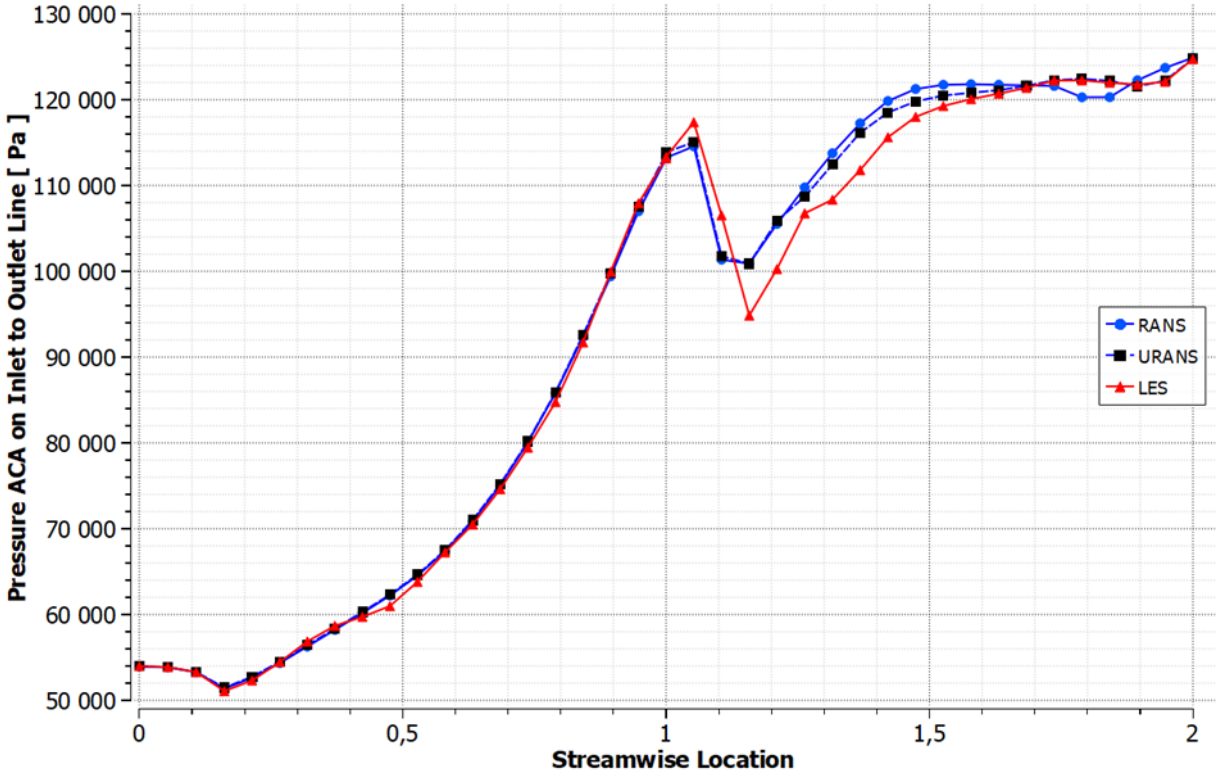

Figure 4-36 Relative Static pressure variation for the three turbulence models.

The relative static pressure plot illustrates the changes in pressure along the compressor, from the inlet at position 0 through the impeller (0 to 1) and into the diffuser (1 to 2). All three turbulence models—RANS (blue), URANS (black), and LES (red)—show a general increase in static pressure, reflecting the compression of air through these components. Initially, there is a gradual rise in pressure within the impeller, followed by a sharper increase nearing the impeller exit. Notably, LES displays more pronounced fluctuations, particularly around the transition from the impeller to the diffuser, highlighting finer details of the flow that are not as evident in RANS and URANS. The RANS model provides a smoother and more averaged pressure rise, while URANS captures some transient features but not to the extent of LES. This suggests that LES is more sensitive to capturing complex flow dynamics, such as separation and reattachment phenomena, that are pivotal in accurately modeling the behavior of air within the compressor stages.

4.4.5 Comments on Relative Mach Number Plot

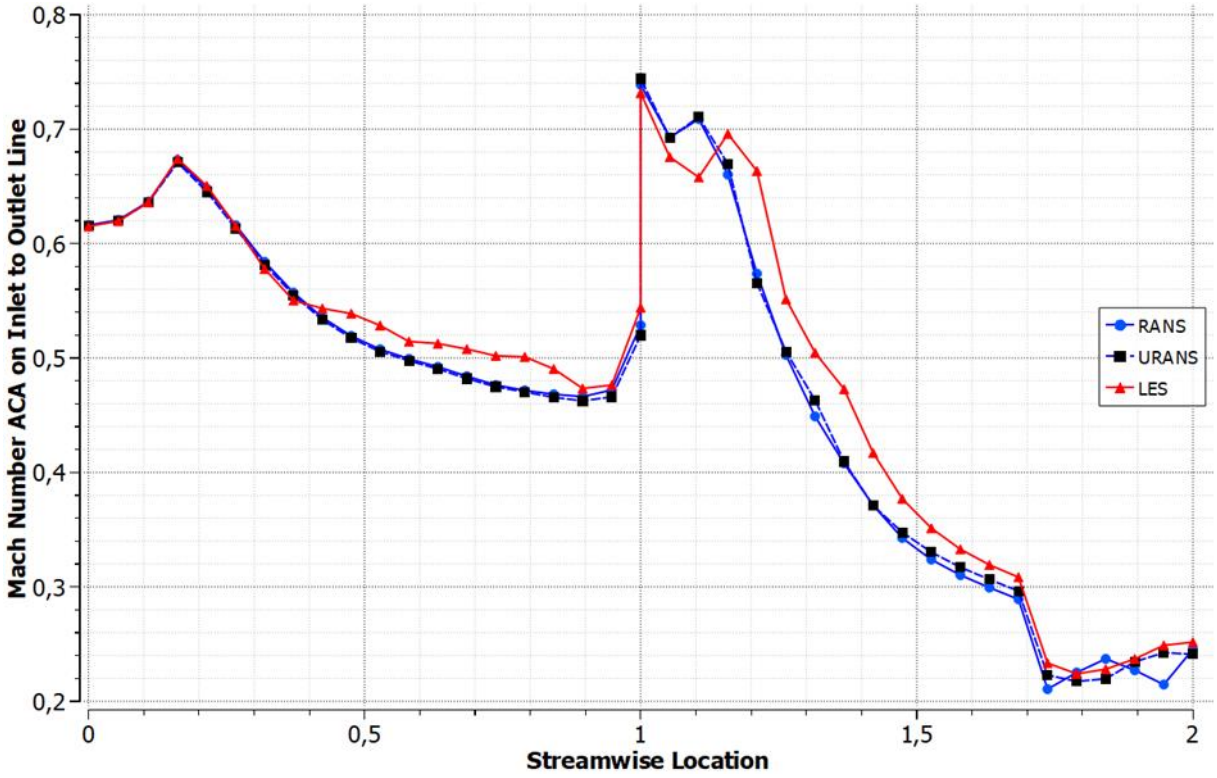

Figure 4-37 Relative Mach number variation for the three turbulence models.

The relative Mach number plot reveals the variation in flow speed relative to the speed of sound along the compressor, from the inlet (0) through the impeller (0 to 1) and into the diffuser (1 to 2). The Mach number initially increases within the impeller, peaking just before the impeller exit, which indicates the acceleration of the air due to the impeller's action. After this peak, there is a significant decrease in the Mach number as the flow decelerates in the diffuser, converting dynamic pressure into static pressure. The LES model (red) shows more detailed fluctuations and sharper changes in Mach number, especially near the impeller exit, indicating a more precise capture of turbulent and unsteady effects. The RANS model (blue) smoothens these changes, providing a more averaged representation, while URANS (black) captures more detailed behavior than RANS but still less than LES. The differences between the models are most notable around the impeller exit and diffuser regions, where LES's ability to resolve finer flow structures becomes evident.

4.4.6 Comments on Relative Static Entropy Plot

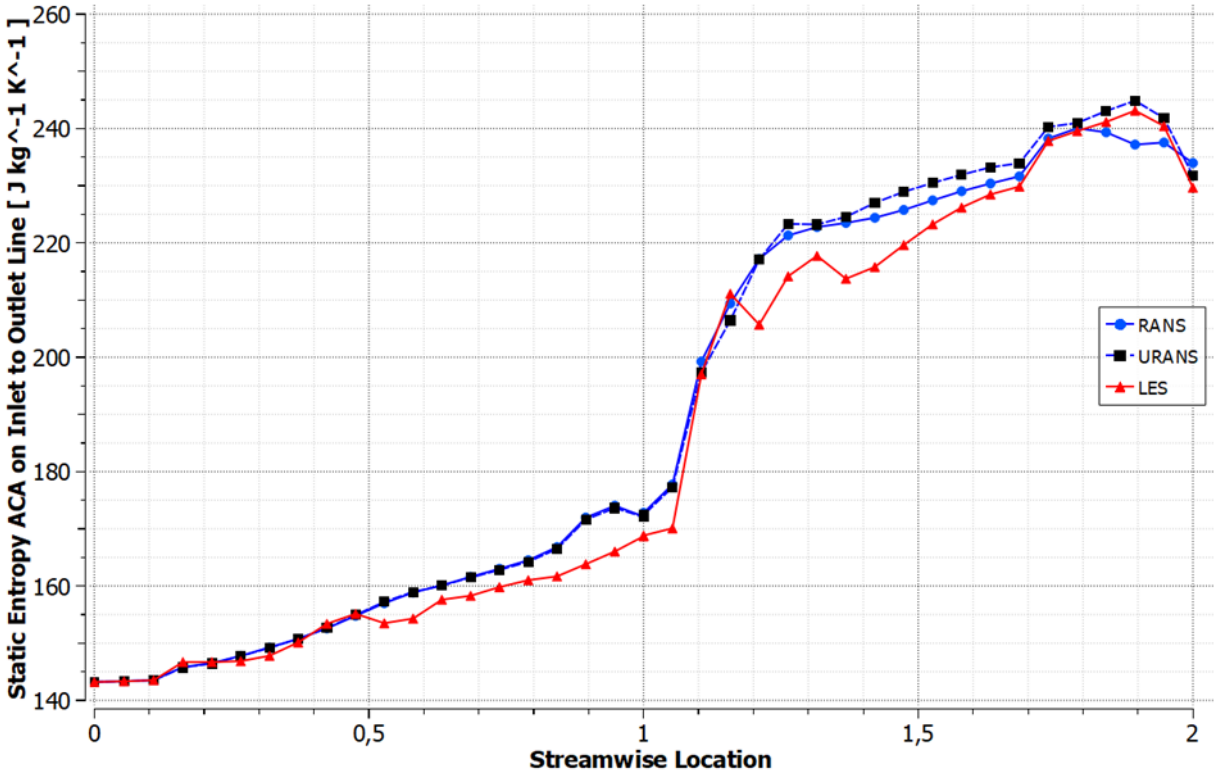

Figure 4-38 Relative Static entropy variation for the three turbulence models.

The relative static entropy plot depicts the entropy changes along the compressor, from the inlet (0) through the impeller (0 to 1) and into the diffuser (1 to 2). Entropy increases as the flow moves through the compressor due to irreversible processes such as viscous dissipation and turbulence. This increase is continuous, with the most significant rise occurring in the impeller and continuing through the diffuser. The LES model (red) shows a more detailed and fluctuating entropy profile, particularly around the impeller exit and within the diffuser, indicating a higher resolution of the turbulent dissipation effects. The RANS model (blue) presents a smoother and more averaged increase in entropy, while URANS (black) captures more of the transient and detailed features than RANS but less than LES. The LES model's detailed fluctuations suggest that it captures more complex interactions and energy dissipation processes, providing a more comprehensive understanding of the flow dynamics within the compressor stages.

Conclusions

The comparative evaluation of RANS, URANS, and LES models in simulating a centrifugal compressor underscores the critical differences and unique benefits each model offers, with a particular emphasis on the capabilities and significance of the LES model.

RANS, known for its robustness and computational efficiency, provides a smooth and steady depiction of flow parameters such as pressure and temperature. This makes it an excellent choice for preliminary analyses and scenarios where computational resources are limited, offering a quick overview of general flow behaviors and trends. However, its limitations in capturing detailed turbulent structures and transient phenomena restrict its use in high-fidelity applications.

URANS serves as a middle ground between RANS and LES, incorporating unsteady effects to enhance accuracy while maintaining a manageable computational cost. This model is valuable for applications requiring a better representation of transient behaviors and flow unsteadiness than RANS can provide, but without the substantial computational demands of LES.

The LES model stands out as the most advanced and detailed simulation approach, crucial for capturing the intricate and complex nature of turbulent flow structures. LES excels in resolving fine-scale turbulence and transient phenomena with high accuracy, offering unparalleled insights into the flow dynamics within the centrifugal compressor. This model's ability to capture detailed flow features is indispensable for in-depth analysis, optimization, and design improvements. The detailed pressure, temperature, and flow structure information provided by LES can significantly enhance the understanding and performance optimization of the compressor.

Despite its high computational cost, the detailed insights gained from LES make it an essential tool for high-fidelity simulations. It is particularly important in scenarios where capturing the full complexity of turbulence is critical for achieving accurate and reliable results. The level of detail and accuracy provided by LES is unmatched, making it the preferred choice for researchers and engineers aiming for the most precise and comprehensive analysis.

In summary, while RANS and URANS offer valuable benefits for less demanding simulations, the LES model's capability to deliver highly detailed and accurate results is crucial for advanced analysis of centrifugal compressors. The choice of model should balance the need for accuracy and detail against available computational resources, with LES being the optimal choice for high-fidelity simulations where understanding the intricate details of turbulent flow is paramount.

Bibliography

1. Rui Zhu 2021, “EFFECTS OF GEOMETRIC AND OPERATIONAL UNCERTAINTIES ON THE AERODYNAMIC PERFORMANCE OF A CENTRIFUGAL COMPRESSOR STAGE”.
2. Wang Yi 2020, “Numerical Investigation of a Centrifugal Compressor with a Pre-Compression Wedge Diffuser under High Subsonic Conditions”.
3. Seongbin Hong 2022, “Numerical Study on Vortical Flow Structure and Performance Enhancement of Centrifugal Compressor Impeller”.
4. Ali Zamiri 2020, “Scale-Adaptive Simulation of the Unsteady Turbulent Flow in a High-Speed Centrifugal Compressor with a Wedge-Type Vaned Diffuser”.
5. Simon J 2009, “Developing Large Eddy Simulation for Turbomachinery Applications”.
6. S. Vagnoli 2015, “URANS analysis of the effect of realistic inlet distortions on the stall inception of a centrifugal compressor”.
7. Ibrahim Shahin 2016, “Large eddy simulation of surge inception and active surge control in a high speed centrifugal compressor with a vaned diffuser”.
8. Ali Zamiri 2017, “Numerical evaluation of transient flow characteristics in a transonic centrifugal compressor with vaned diffuser”.
9. Kai U.Ziegler, “Astudy on impeller-diffuser interaction—part 1: influence on the performance”.
10. S. L. Dixon,” Fluid Mechanics and Thermodynamics of Turbomachinery Sixth Edition".
11. Meherwan P.Boyce,P.E. “Centrifugal compressors a basic guide”.
12. MICHAEL Casey, “Radial Flow Turbocompressors design, analysis, and applications”.
13. Hawthorne 1974, “Secondary vorticity in stratified compressible fluids in rotatingsystems”.
14. . Ziegler 2002, “A Study on Impeller-Diffuser Interaction: Part I—Influence on the Performance”.
15. Jones 1972, “The Prediction of laminarization with a two-equation model of turbulence
16. Wilcox1998, “Turbulence Modeling for CFD, 2nd ed.”.
17. Rumesy, “Assessment of two-equation turbulence models for transonic Flows”.
18. Tutorial ansys 2023.
19. Johannes Schiff 2013, “A Preliminary Design Tool For Radial Compressors June”.